POLITECNICO DI MILANO

Scuola di Ingegneria Industriale e dell'Informazione

Corso di Laurea Magistrale in Ingegneria Nucleare

RADIATION-INDUCED VAPORISATION OF SUPERHEATED NANODROPLETS AS AN IN VIVO PROTON RANGE VERIFICATION TECHNIQUE: A MONTE CARLO APPROACH

Tesi di Laurea Magistrale di:
Andrea GIAMMANCO
Matricola n. 878127

Relatore: Prof. Stefano AGOSTEO
Correlatori: Prof. Uwe HIMMELREICH
Prof. Edmond STERPIN
Prof. Gianni COPPA

Anno Accademico 2017 - 2018

Acknowledgements

I'm so grateful for the constant support given to me by my Supervisor Prof. Agosteo and by my Co-Supervisor Prof. Coppa during this long period. Despite the distance, they helped me with all the difficulties that I encountered, giving helpful advice whenever there were the need.

Then, I want to refer my acknowledgements to Prof. Himmelreich and Prof. Sterpin for having supported me on a daily basis in the realization of this work and for the great opportunity that they have given to me; this international experience at KU Leuven has made me grew both personally and professionally.

Furthermore, I want to express my best appreciation to the PhD students Bram Carlier and Sophie Heymans for all their teachings and for having helped me in the realization of this work on a daily basis always with kindness.

A special "thanks" goes also to the MoSAIC people for making me part of their family during my stay in Belgium.

At last, but not least, my truly and lovely greetings go to my family and to my girlfriend, that no matter what happens give me the best support to build my own life.

Milan, April 2019 A. G.

Sommario

Al giorno d'oggi le radiazioni ionizzanti hanno molte applicazioni in medicina; una di questa è la protonterapia, utilizzata per i trattamenti tumorali. Quest'ultima ha un efficacia limitata nel trattamento dei tumori maligni a causa delle incertezze sul range dei protoni, le quali spesso costringono all'utilizzo di trattamenti non ottimali per salvaguardare i tessuti sani. Il presente lavoro, sviluppato come parte di un più ampio progetto Europeo denominato "AMPHORA", ha lo scopo di indagare il potenziale utilizzo di nano-gocce surriscaldate per verificare il range dei protoni in-vivo. Nello specifico, utilizzando il toolkit Geant4 è stato sviluppato un modello Monte Carlo che è stato utilizzato per simulare la vaporizzazione di quest'ultime indotta dall'interazione con le radiazioni ionizzanti. Le simulazioni sono state condotte utilizzando nano-gocce contenenti C_3F_8 o C_4F_{10} in diverse condizioni sperimentali. Inoltre, per ridurre il tempo necessario alla simulazione, è stata sviluppata e validata una tecnica di accelerazione approssimata. Utilizzando questa tecnica abbiamo dimostrato che, almeno nel caso in cui vengono utilizzate nano-gocce contenenti C_3F_8, già a partire da una temperature di 36°C sembra possibile identificare il Bragg peak analizzando gli eventi di vaporizzazione. Dunque, i risultati sono incoraggianti e sono già in programma esperimenti aventi lo scopo di validare i risultati presentati in questo lavoro. Una volta validato, questo modello consentirà di ottimizzare i futuri esperimenti e restituirà informazioni utili circa la risposta delle nano-gocce surriscaldate alle radiazioni ionizzanti.

Parole chiave: dosimetria in-vivo, emulsioni surriscaldate, mezzo di contrasto a cambiamento di fase, PCCA, mezzo di contrasto per ultrasuoni, UCA, verifica del range dei protoni, protonterapia, radioterapia, Monte Carlo, Geant4

Abstract

Nowadays, the use of ionising radiation has many applications in medicine; one of which is the Proton Therapy for cancer treatment. However, uncertainties in the proton beam range lead to non-optimal treatments, hence limiting the effectiveness of proton therapy in treating malignant tumours, while sparing healthy tissue. This work, developed as part of the larger European project "AMPHORA", investigates the potential use of superheated nanodroplets as an in-vivo proton range verification tool. In particular, nanodroplets convert into highly echogenic microbubles detectable via ultrasound interrogation upon radiation induced vaporisation. Here, a Monte Carlo model was build using the Geant4 toolkit and it was used to simulate the radiation induced vaporisation of superheated nanodroplets containing C_3F_8 or C_4F_{10} under different experimental conditions. To reduce the simulation time, an approximate acceleration technique was developed and validated. Using this technique we showed that, at least using C_3F_8, already starting from a temperature of 36°C it seems possible to detect the Bragg peak region looking at the vaporisation events. So, results are encouraging and future experiments are planned in order to validate the results presented in this work. Once validated, this model will allow to readily optimise future experiments and provide useful insights into the nanodroplets' radiation response.

Keywords: in-vivo dosimetry, superheated emulsions, phase change contrast agent, PCCA, ultrasound contrast agent, UCA, proton range verification, proton therapy, radiation therapy, Monte Carlo, Geant4

Estratto in lingua Italiana

Al giorno d'oggi, con circa 2.9 milioni di nuovi casi ogni anno, il cancro rappresenta una delle principali cause di morte in tutto il mondo. Nella lotta contro questa malattia, l'utilizzo terapeutico delle radiazioni ionizzanti, in associazione ad altri trattementi, quali la chemioterapia e la chirurgia, ricopre un importante ruolo. Infatti, le radiazioni ionizzanti, interagendo con la materia biologica, possono provocare danni permanenti al DNA, interrompendo la proliferazione incontrollata tipica delle cellule neoplastiche. Purtroppo, allo stesso modo possono venire danneggiate anche le cellule dei tessuti sani; per questo motivo è importante ottenere una distribuzione di dose il più possible conforme al tessuto tumorale. In aggiunta, i danni causati dalle radiazioni hanno una natura stocastica; per descrivere la probabilità di successo di un trattamento sono state introdotte due quantità, la Tumour Control Probability (TCP) e la Normal Tissues Complication Probability (NTCP). L'obiettivo è ottenere un elevata TCP mantenendo la NTCP a valori definiti "accettabili".

Negli anni questo settore ha avuto un enorme sviluppo; ad oggi vi sono nuove tecniche, come la protonterapia e la adroterapia, che consentono di ottenere distribuzioni di dose sempre più conformi alla massa tumorale da trattare. Purtroppo le loro potenzalità non possono essere sempre sfruttate al meglio; questo a causa delle numerose incertezze presenti in tutti gli step di cui sono costitutiti i processi di pianificazione e somministrazione del trattamento. Tali incertezze, se non vengono prese opportune precauzioni, possono portare a distribuzioni di dose completamente diverse da quelle previste, provocando effetti opposti rispetto a quelli auspicati.

In questo lavoro particolare attenzione è stata posta alla protonterapia. La distribuzione di dose ottenuta utilizzando un fascio di protoni, a differenza di quella prodotta da un fascio di fotoni (utilizzato nella radioterapia convenzionale), presenta un picco molto pronunciato (picco di Bragg) dovuto ad un aumento significativo della sezione d'urto delle interazioni Coulombiane nel mezzo a seguito del rallentamento del fascio. Dunque, tale picco si presenta nella zona corrispondente al range dei protoni nel mezzo attraversato e, dato che il Bremsstrahlung è trascurabile, il tessuto che si trova oltre tale zona riceve una dose pressoché nulla. L'energia del fascio può essere quindi modulata per far coincidere il picco con la zona del tessuto tumorale, massimizzando in questo modo la TCP e riducendo la NTCP.

Nel caso della protonterapia, le incertezze nel processo di pianificazione e somministrazione del trattamento hanno diverse fonti; alcune sono presenti indipendentemente dal metodo utilizzato per pianificare il trattamento (riproducibilità del fascio, errori nel posizionamento del paziente, etc.) mentre altre derivano da quest'ultimo (calibrazione delle immagini ottenute con tomografia computerizzata, parametri fisici utilizzati nella pianificazione del trattamento, etc.). Tali incertezze sono state stimate; anche se il trattamento viene pianificato con un software Monte Carlo, l'incertezza complessiva sul range ammonta a circa il 2.4% più 1.2 mm.

Un'incertezza sul range si riflette immediatamente sul posizionamento del picco di Bragg; in alcune situazioni potrebbero bastare pochi millimetri per causare una deposizione di dose massima nei tessuti sani ed una deposizione ridotta o nulla nei tessuti tumorali. Dunque, le tecniche più utilizzate per far fronte a queste incertezze prevedono l'adozione di margini di sicurezza nel processo di pianificazione e l'utilizzo di geometrie del fascio non ottimali. Queste comportano una riduzione dell'efficacia del trattamento; una maggior accuratezza sul range consentirebbe di sfruttare a pieno tutti i vantaggi della protonterapia, salvaguardando al tempo stesso i tessuti sani.

Alcune tecniche per la verifica del range dei protoni, pur con delle limitazioni, sono già state sviluppate ed altre sono in fase di studio. Ognuna di esse cerca di sfruttare un fenomeno fisico diverso (ex. emissione di γ pronti, annichilazione di positroni, etc.) per estrapolare informazioni riguardo la distribuzione di dose all'interno del paziente.

All'interno del progetto Europeo *AMPHORA* (Acoustic Markers for Enhanced Remote Sensing of Radiation Doses), di cui questo lavoro fa parte, si sta studiando un sistema affidabile e non invasivo in grado di dare informazioni precise riguardo il range dei protoni direttamente in vivo. Nello specifico, si vuole indagare il potenziale utilizzo di nano-gocce surriscaldate radio-sensitive per rilevare la posizione del picco di Bragg dall'esterno utilizzando una sonda ad ultrasuoni. Tali nano-gocce sono costituite da perfluorocarburi in condizioni di liquido surriscaldato (ovvero liquido in condizioni di temperatura e pressione corrispondenti alla zona dei vapori) e sono rivestite da un monostrato di PCDA (Pentacosadiynaic acid). La shell esterna, oltre a fornire stabilità alle nano-gocce, può essere funzionalizzata per far sì che, una volta iniettate nel paziente, esse si vadano ad accumulare nella regione di interesse.

L'interazione delle radiazioni ionizzanti con le nano-gocce surriscaldate può, in determinate condizioni, provocarne la vaporizzazione. Durante il processo di vaporizzazione viene emesso un segnale acustico caratteristico; esso è il risultato di una complessa dinamica oscillatoria che rimane in essere fino a quando lo stato di equilibrio finale non viene raggiunto. La frequenza di tale segnale dipende dalle caratteristiche della nano-goccia di partenza e può essere stimata analiticamente. Inoltre, esso può essere utilizzato per ottenere informazioni circa la distribuzione di dose in tempo reale.

Le microbolle risultanti sono fortemente ecogeniche; per questo motivo possono essere utlizzate come mezzo di contrasto per ultrasuoni (Ultrasound Contrast Agent, UCA). In particolare, dato che la caratteristica di ecogenicità si presenta solo dopo la vaporizzazione, tali nano-gocce sono definite "mezzi di contrasto a cambiamento di fase" (Phase Change Contrast Agents, PCCA).

Lo studio della vaporizzaziona indotta da radiazioni ionizzanti può essere effettuato utilizzando una teoria semi-empirica sviluppata da Seitz nel 1958 per le camere a bolle e verificata sperimentalmente in studi successivi anche per i liquidi surriscaldati. Secondo tale teoria, per attivare il processo di vaporizzazione è necessario che si formi una bolla di vapore all'interno dell'emulsione surriscaldata di dimensioni tali (dimensioni "critiche") da possedere un'energia sufficiente a superare la barriera energetica che si oppone alla sua espansione. Il raggio critico R_c ed il valore della barriera energetica W_{tot} possono essere determinati analiticamente.

L'interazione delle radiazioni ionizzanti con un liquido surriscaldato, secondo la teoria del Thermal Spike di Seitz, provoca un immediato trasferimento di calore localizzato. Questo induce la formazione di nano-cavità di vapore; è stato dimostrato sperimentalmente che, se viene depositata un'energia pari a quella della barriera energetica definita in precedenza in una distanza pari a k volte il raggio della bolla di dimensioni "critiche", viene indotta la vaporizzazione di tutta la nano-goccia. Il parametro k è detto *parametro di nucleazione* e, in diversi studi sperimentali, ne è stato riportato un valore compreso tra 2 e 12. Il rapporto tra W_{tot} e la distanza $L_{eff} = k * R_c$ può essere interpretato come un requisito minimo sul LET (Linear Energy Transfer) della radiazione ionizzante incidente affinché questa provochi una vaporizzazione. Tale requisito minimo è fortemente dipendente dalla temperatura; tanto più la temperatura è vicina al limite superiore di surriscaldamento (temperatura oltre la quale si ha vaporizzazione spontanea; essa dipende dalla pressione e dalla tipologia di perfluorocarburo), tanto minore è tale requisito. Questa peculiare caratteristica delle nano-gocce surriscaldate consente di tararne la “sensibilità” variando la temperatura operativa o la composizione del perfluorocarburo; in questo modo è possibile renderle sensibili solo a radiazioni aventi un LET medio superiore ad una soglia pre-determinata.

All’interno di questo lavoro, utilizzando il toolkit Geant4, è stato sviluppato un modello Monte Carlo in grado di simulare la risposta di nano-gocce surriscaldate contenenti C_4F_{10} o C_3F_8 indotta dall’interazione con le radiazioni ionizzanti. Tale modello consentirà di pianificare ed ottimizzare gli esperimenti nei quali verranno provate le nano-gocce surriscaldate oggetto dello studio. In particolare, una volta validato consentirà di indagare diverse possibili condizioni sperimentali al fine di individuare la combinazione che con maggiore probabilità porterà a risultati positivi. Questo consentirà di ridurre al minimo il numero di esperimenti, con un risparmio di tempo e denaro non indifferente.

Tali simulazioni, senza utilizzare alcun accorgimento, richiederebbero tempi lunghissimi. Infatti, a causa delle dimensioni delle nano-gocce ($\approx 560nm$ diametro), per ottenere informazioni accurate circa le interazioni che avvengono al loro interno, è necessario utilizzare un algoritmo di simulazione step-by-step. Un algoritmo di questo tipo, se applicato per simulare il trasporto di particelle cariche, richiederebbe la simulazione di un numero elevatissimo di interazioni per singola particella. Per questo motivo, utilizzando una comune workstation (HP Z440), non sarebbe possibile simulare in tempi ragionevoli le interazioni di un fascio di protoni o fotoni con tali nano-gocce in una geometria macroscopica.

Per risolvere questo problema è stata sviluppata e validata una tecnica di accelerazione approssimata in grado di ridurre drasticamente i tempi di simulazione. L’applicazione di tale tecnica provoca però l’introduzione di un errore sistematico; in ogni caso, in opportune condizioni (es. basse frazioni totali di nano-gocce vaporizzate, requisiti di LET sufficientemente bassi) l’entità di quest’ultimo è facilmente quantificabile. In aggiunta, abbiamo verificato che esso non incide in maniera sostanziale sull’andamento qualitativo delle curve di vaporizzazione.

L’applicazione di tale tecnica prevede, come primo step, l’identificazione delle radiazioni ionizzanti “rilevanti” in termini di fluenza e LET medio per il setup sperimentale in esame. Una volta identificate, per ognuna di esse deve essere effettuato un set di simulazioni in cui la sorgente è costituita da un fascio monoenergetico di particelle della stessa tipologia incidenti su un singolo strato (di spessore t_l, area A e materiale opportunamente scelto) contenente la concentrazione di nano-gocce desiderata. Grazie alle dimensioni estremamente ridotte del dominio di simulazione, in questo caso è possibile utilizzare algoritmi step-by-step; confrontando il LET relativo alle interazioni all'interno delle nano-gocce con il LET minimo determinato nelle condizioni sperimentali in analisi è possibile identificare tutti gli eventi di vaporizzazione. Dunque, l'intero set di simulazioni ha lo scopo di determinare la probabilità di vaporizzazione p_i^k relativa ad una particella ionizzante di tipologia k ed energia i incidente perpendicolarmente su uno strato di spessore t_l contenente nano-gocce in concentrazione nota.

Una volta determinate tutte le p_i^k, deve essere effettuata una simulazione utilizzando la geometria del setup sperimentale in analisi. In essa però non devono essere inserite le nano-gocce; piuttosto, il volume sensibile che le avrebbe dovute contenere deve essere suddiviso in strati di spessore t_l ed il flusso Φ_{ij}^k di particelle di tipologia k ed energia i incidenti perpendicolarmente sullo strato j viene determinato.

Questa tecnica consente quindi di suddividere il problema in due sotto-problemi di più semplice risoluzione; infatti, il primo prevede una simulazione in scala microscopica ed il secondo non necessita più di algoritmi step-by-step.

A questo punto la stima del numero di eventi di vaporizzazione viene effettuata ipotizzando che ogni singola particella ionizzante incidente rappresenti un Bernouilli trial avente probabilità di successo pari a p_i^k. Dunque, dato che il numero totali di particelle di tipologia k incidenti sullo strato j è pari a $\Phi_{ij}^k A$, il valore atteso del numero di eventi di vaporizzazione in ciascuno strato sarà pari a $p_i^k(\Phi_{ij}^k A)$. Sommando su tutti gli strati, tutte le energie e tutte le radiazioni ionizzanti rilevanti si ottiene una stima del numero totale di vaporizzazioni.

La validazione di questa tecnica è stata effettuata confrontando il profilo di vaporizzazione ottenuto con e senza la sua implementazione. Per fare questo, sono state condotte delle simulazioni in geometrie microscopiche utilizzando nano-gocce contenenti C_3F_8 o C_4F_{10} ed un fascio primario di protoni o fotoni.

Per quantificare lo scostamento tra coppie di profili corrispondenti, è stato calcolato il Mean Absolute Percentage Error (MAPE):

$$\begin{aligned} MAPE^i &= \frac{\left|Vap^i_{fraction,real} - Vap^i_{fraction,approx}\right|}{Vap^i_{fraction,real}} \\ MAPE &= \frac{\sum_{i=1}^{N} MAPE^i}{N} \end{aligned} \tag{1}$$

Dove i rappresenta l'indice dello strato, N è il numero totale di strati, $Vap^i_{fraction,real}$ è il numero di vaporizzazioni nello stato i e $Vap^i_{fraction,approx}$ è il numero di vaporizzazioni nello strato i calcolato utilizzando il metodo approssimato.

Di seguito, a titolo di esempio, viene riportato il confronto tra i profili di vaporizzazione relativi a nano-gocce contenenti C_3F_8 ottenuti simulando un fascio di protoni primario a 35°C e variando il parametro di nucleazione in modo parametrico.

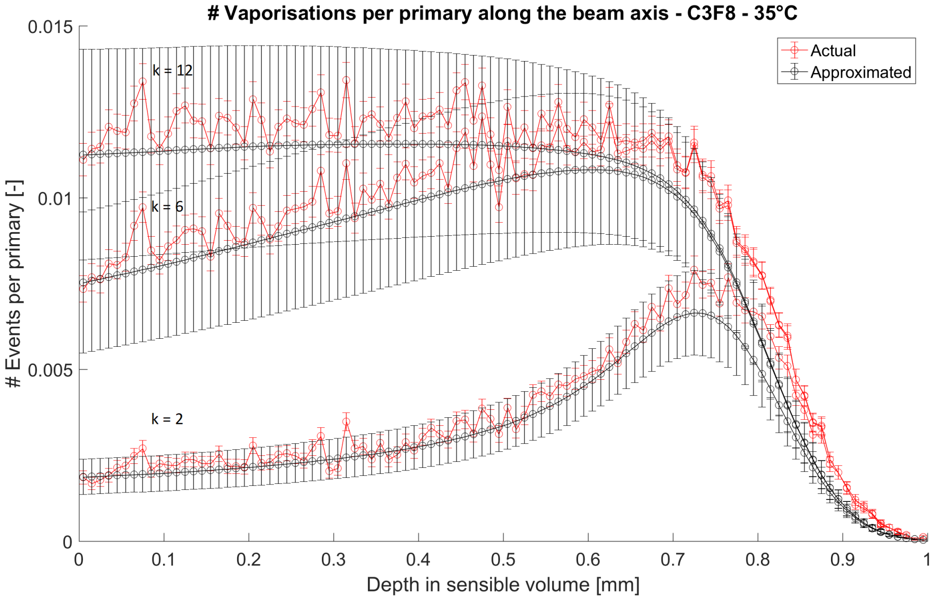

Figure 1: Validazione della tecnica di accelerazione approssimata utilizzando un fascio di protoni e nano-gocce surriscaldate contenenti C_3F_8. Confronto tra i dati grezzi ottenuti utilizzando diversi valori del parametro di nucleazione.

I profili di vaporizzazione, da un punto di vista qualitativo, sono sempre risultati sovrapponibili. In aggiunta, in tutte le validazioni effettuate il MAPE si è sempre mantenuto sotto il 20%, raggiungendo anche valori inferiori al 3% in alcuni casi.

Dopo aver concluso la validazione, tale tecnica è stata utilizzata per realizzare diverse simulazioni in geometria macroscopica aventi lo scopo di analizzare il comportamento delle nano-gocce in diverse condizioni sperimentali. In particolare, simulando il reale set-up sperimentale che verrà utilizzato in futuro, è stata analizzata la risposta di nano-gocce contenenti C_3F_8 o C_4F_{10} utilizzando un tipico fascio di protoni da 60 MeV.

Per ogni tipologia di nano-gocce, sono stati condotti due set di simulazioni: nel primo è stata fissata la temperature a 36°C ed è stato variato il parametro di nucleazione in modo parametrico, mentre nel secondo è stato fissato il parametro di nucleazione a 4 ed è stata variata la temperatura in modo parametrico.

Il primo set di simulazioni ha lo scopo di valutare se sarà possibile distinguere il picco di Bragg analizzando gli eventi di vaporizzazione in un ipotetico esperimento futuro condotto a 36°C. Infatti, le simulazione condotte assumendo il valore più basso possibile del parametro di nucleazione (k = 2) consentono di esaminare la risposta delle nano-gocce surriscaldate nel peggiore scenario; se in esso viene evidenziata in modo netto la zona del picco di Bragg, vi sono ottime probabilità di riuscita dell'esperimento.

Il secondo set di simulazioni ha lo scopo di stimare la temperatura minima necessaria all'identificazione del picco di Bragg per i due diversi perfluorocarburi.

Per rendere i risultati confrontabili con gli esperimenti futuri, il numero di vaporizzazioni è stato calcolato "per Monitor Unit (MU)"; seguendo le indicazioni fornite dalla Université catholique de Louvain (UCL), presso la quale verranno effettuati gli esperimenti, è stato posto 1 MU $\approx 10^8$ protoni primari.

Sovrapponendo le curve di vaporizzazione con la curva di deposizone di dose sono stati ottenuti risultati promettenti: utilizzando nano-gocce contenenti C_3F_8, già a partire da una temperatura di 36°C, sembra possibile identificare chiaramente il Bragg peak analizzando gli eventi di vaporizzazione. D'altro canto, a causa delle incertezze sul parametro di nucleazione, non è chiaro se sarà possibile identificarlo utilizzando nano-gocce contenenti C_4F_{10}; in quest'ultimo caso probabilmente la temperatura dovrà essere più elevata. Di seguito sono riportati i grafici più significativi:

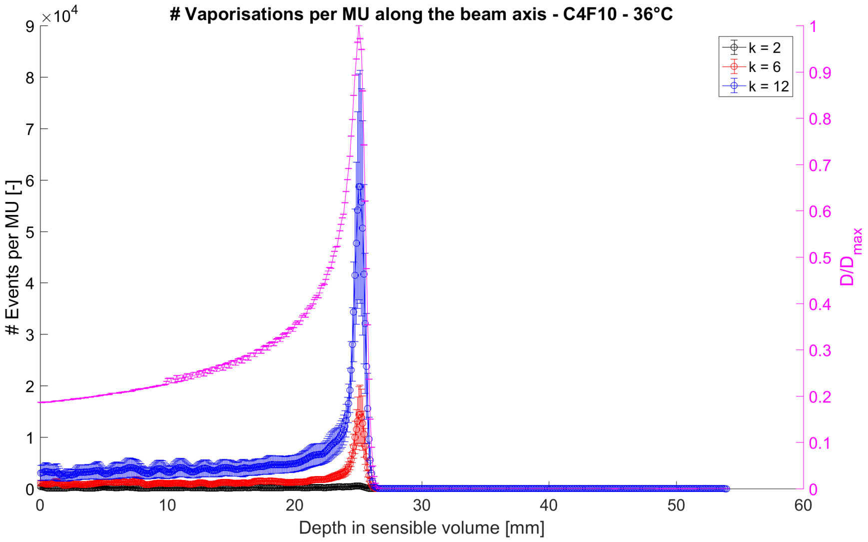

Figure 2: Vaporizzazioni per MU lungo l'asse del fascio utilizzando un fascio di protoni a 60 MeV. Nano-gocce contenenti C_4F_{10} a 36°C, diversi valori del parametro di nucleazione. La curva di deposizione di dose normalizzata è riportata in magenta.

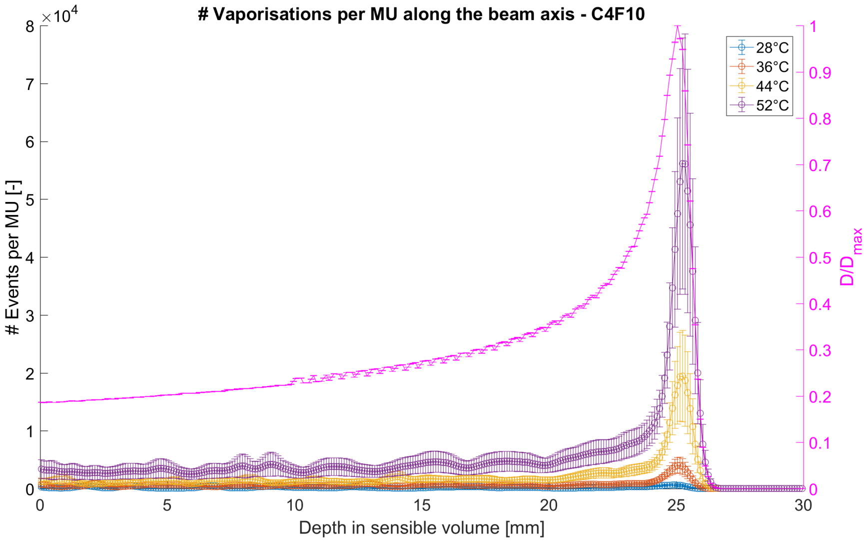

Figure 3: Vaporizzazioni per MU lungo l'asse del fascio utilizzando un fascio di protoni a 60 MeV. Nano-gocce contenenti C_4F_{10} a diversi valori di temperatura . Parametro di nucleazione fissato a 4. La curva di deposizione di dose normalizzata è riportata in magenta.

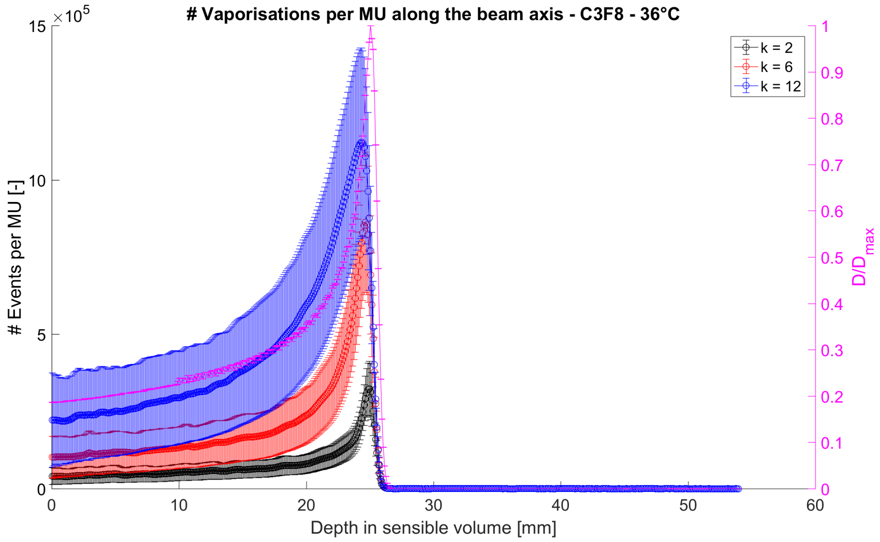

Figure 4: Vaporizzazioni per MU lungo l'asse del fascio utilizzando un fascio di protoni a 60 MeV. Nano-gocce contenenti C_3F_8 a 36°C, different values of the nucleation parameter. La curva di deposizione di dose normalizzata è riportata in magenta.

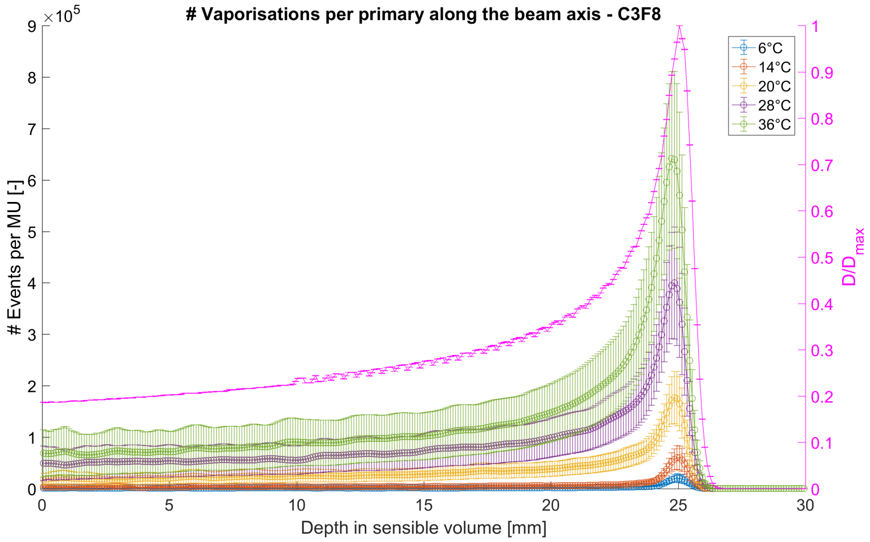

Figure 5: Vaporizzazioni per MU lungo l'asse del fascio utilizzando un fascio di protoni a 60 MeV. Nano-gocce contenenti C_3F_8 a diversi valori di temperatura . Parametro di nucleazione fissato a 4. La curva di deposizione di dose normalizzata è riportata in magenta.

In ogni caso, la fisica che governa il processo di vaporizzazione è complessa e la teoria utilizzata per descriverlo è basata su modelli semi-empirici. Questo rende le previsioni difficili e richiede che ogni modello venga validato sperimentalmente. Inoltre, nel modello da me sviluppato sono state fatte diverse ipotesi: è stato trascurato l'effetto della pressione di Laplace, la distribuzione dimensionale delle nano-gocce è stata supposta monodispersa e gli eventi di vaporizzazione spontanea dovuti all'agitazione termica sono stati completamente trascurati. Per questo motivo, il prossimo passo sarà quello di validare i risultati presentati in questo lavoro; a tale scopo, sono già in programma esperimenti nel prossimo futuro.

Contents

Chapter 1

Introduction

Nowadays cancer is one of the leading health problems worldwide, representing about 2.9 million new cases and 1.7 million deaths each year [1]. These numbers are huge, and great efforts in research are currently made to develop new treatments and to optimize the existing ones. Standard treatment consists in surgery, chemotherapy, radiotherapy or a combination of them.

In the therapeutic strategies, high energy photons or particles are often exploited to irradiate the tumour and kill the malignant cells by inducing DNA damages. In fact, the irradiation can be used both as a curative treatment (to destroy the tumour or to reduce the risk of malignant recurrences) or as a palliative one (to alleviate patient's pain). This technique is called *radiotherapy*. The success of a radiotherapy relies on the ability to achieve *high tumour conformity* in terms of delivered dose distribution, in order to optimize the trade-off between tumour damage and healthy tissue toxicity.

Since its first clinical usages, extensive developments in that field have brought new techniques (e.g. hadrontherapy) that enable a more precise delivery of high doses to the tumour site reducing the side effects for the surrounding healthy tissues. At the same time, there is an increasing need of an accurate quality assurance during the treatment delivery. In fact, to fully exploit the advantages of the high tumour conformity present in the new techniques, it is necessary to assess the delivered dose distribution with high accuracy [1].

For many years, dose verification methods have remained rudimentary, consisting in offline measurements or point verification at the patient's skin surface. In fact, the effects of uncertainties in patient positioning, patient anatomy (that generally changes during the course of the treatment) and machine output have already led to several reported cases of accidents in conventional radiotherapy treatments (dose inhomogeneities, secondary malignancies, lack of tumour control, organ failure) [2]. Luckily, nowadays to cope with with the increasing complexity of the treatment plans, new, more reliable methods are used (e.g. Image Guided Radiotherapy) and a set of *quality assurance* procedures on radiotherapy treatments are adopted. However, in the field of particle therapy, where beams of protons or heavy charged particles are used, there are still significant uncertainties about the actual range in the human body of such particles that strongly limit the huge potential of these innovative techniques.

Some in-vivo dosimetry systems that measure the dose at the skin level already exist, but they are not part of the clinical routine nowadays due to their inaccuracy in predicting the actual dose distribution at the tumour site. In addition, some implanted or intra-cavity dosimeters have been developed, but they imply a high degree of invasiviness for the patients [4]. Consequently, there is a need for an improved non-invasive device and method that allows an efficient measurement of dose distribution in and around a tumour during radiotherapy. To fill this gap, the *AMPHORA* (Acoustic Markers for Enhanced Remote Sensing of Radiation Doses)[1] project proposes the use of innovative in-vivo dosimeters made by superheated nanodroplets to improve patient's safety and to optimize the treatment efficiency.

Consequently, the aim of the *AMPHORA* project is to develop an *in situ* radiation dosimeter based on functionalized, radiosensitive, non-invasive ultra sound contrast agents (UCAs). The idea is to exploit the capability of UCAs to translate an imparted radiation dosage into a modulation of their acoustic response upon ultrasound interrogation. A rough work-flow for the use of UCAs would be the following:

1. Prior to the beam delivery, UCAs would be injected into the patient;
2. UCAs are functionalized with targeting moieties like antibodies or small peptides which would accumulate at the region of interest;
3. Upon irradiation, UCAs would change their properties (for example size) dose-dependent to result in a modified ultrasound readout;
4. Contrast ultrasound imaging could be used to produce a 3D distribution map of the dose delivered during the different stages of the treatment.

---

[1] EC H2020 project # 766456

Phase change contrast agents are currently under development. For example, they could be nanodroplets made by a liquid fluorocarbon nucleus surrounded by a lipid shell. These nanodroplets are able to accumulate in the tumour region thanks to their extravasating capability related to their small size ($\approx$ 500nm diameter). Moreover, the nanodroplets are used while in a metastable superheated state (they are called *superheated emulsions*); this will allow to exploit an induced phase change to alter their acoustic properties (e.g. ultrasound attenuation in a given frequency band) in a radiation dose dependent way. The phase change will be induced by the ionizing radiation; an effect that has been extensively used in the field of neutron detection in the last decades and has also proven to be feasible using photons and protons [5]. In addition, the induced vaporisation will cause the emission of characteristic ultrasound pulses that can also be detected with an ultrasound transducer.

In the lead up to this study, initial radiation induced vaporisation experiments using nanodroplets made of liquified decafluorobutane (C_4F10) encapsulated in a fatty acid monolayer of PCDA (Pentacosadiynaic acid) have been carried out. They have been conducted using the facilities of the UZ Leuven Hospital (in particular, using a VARIAN TrueBeam LINAC). Those nanodroplets have also been characterised acoustically triggering the vaporisation by ultrasound in a controlled way.

For the present work, the Geant4 software has been used to simulate the response of different superheated emulsions that are of interest in this project when irradiated using either a photon beam or a proton beam. This allows to predict the behaviour of the superheated emulsions before performing the experiments, and helps the design of the actual experiments in a conscious way, saving time and money required for performing many experiments, with many of them probably not leading to positive results. In order to build up these simulations, an approximate method to reduce the computational effort has been developed and validated.

Before getting to the core of this work, an overview on the discovery of radiation and the historic evolution of their usages is made. A deep insight into the radiation therapy technique is also provided, followed by an overview of the radiation transport problem together with its mathematical formulation. Then, since it has been widely used to build-up the simulations using the Geant4 code, an entire chapter is devoted to the Monte Carlo stochastic method. Afterwards, the theory behind the induced vaporisation of the superheated emulsions and the Geant4 model are fully described. Finally, the results of the performed simulations are presented.

1.1 Radiation: a brief history

The first pioneer in this field was a German physicist, W. C. Roentgen, who in the late 1895 discovered X-rays during experiments with a cathode ray tube in his laboratory. He called this “invisible light capable of passing through the matter” in that way because in mathematics “X” is often used to indicate an unknown quantity. In addition, he discovered that X-rays would pass through the human tissue, making it possible to image the bones and metals. This was exemplified by the most famous X-ray image of Roentgen’s wife’s hand with two rings on her finger (see Fig. 1.1) [6].

Figure 1.1: A, Roentgen’s wife, Anna Bertha Roentgen (1839-1919). B, Wilhelm C. Roentgen. C, Roentgen’s first radiograph, showing his wife’s hand and two rings on her finger. [7]

At that time there were just few options to diagnose and treat several diseases (malignant or benign in nature). For this reason, the news of Roentegen’s discovery spread quickly throughout the world and, without knowing the physical properties of X-rays and their biological effects, X-rays were being utilized clinically for radiology within just one year. The advent of X-ray beams has dramatically improved the available tools to diagnose and, later on to treat such diseases, but due to this lack of knowledge, the actual benefits of such technique were accompanied by important side effects which often worsened the situation [9].

In the following years new radioactive isotopes and radiation techniques were discovered. Scientists began to understand how such radiation interacts with the biological matter and the relations between time and dose on cell survival. In the 1920s this led to the adoption of fractionated dose treatments instead of a singular treatment session, with a remarkable improvement in the cancer control and fewer side effects. Moreover, in 1928 the International Commission on Radiological Protection (ICRP) was created to specifically address the question of radioprotection.

Then, research went on and continuous scientific progress in this field was made, allowing to treat also patients affected by deep cancers and reducing the toxicity of radiation to healthy tissues. However, for many decades, improvements in radiotherapy were inhibited due to issues in characterising the tumour volume and due to the inability to target the radiation beam with sufficient accuracy. The ballistics of treatment were rudimentary due to insufficient imaging and lack of flexibility in treatment delivery.

The period 1930-1950 is known as *Orthovoltage era*. During this period brachytherapy, X-ray kilovoltage (50 kV to 200 kV) tubes and electron beam therapy were introduced. All these revolutionary findings gave birth to a new branch of physics: the *medical physics* [9] .

Then, the period between 1950 and nowadays is known as *Megavoltage era*. In the first part of this period, Cobalt teletherapy (able to deliver high energy γ rays) and electron linear accelerators (LINAC, able to deliver megavoltage X-rays) were introduced. Despite the fact that these high energy radiations allowed to treat more deeper tumours, they were more difficult to manage and there was a need to plan the irradiation in a more detailed way to avoid side effects of the treatment [9]. In the 1970s the first medical CT-scanners were developed. They allowed to go from the so called *conventional radiotherapy*, in which roughly shaped fields were used, to the *conformal radiotherapy*, in which the beam aperture closely follows the edges of the tumour [10]. In addition, also the first multi-field plans were introduced in this period.

It was between the 1970 and 1980 that innovative devices delivering proton beams were employed to treat tumours. Such beams have huge advantages for some cancers because they allow to concentrate the dose in the tumour region affecting in a low extent the surrounding healthy tissues and organs. However, as we will see in the next chapters, this introduced a series of complications in the treatment planning because any uncertainty in its simulation could lead to huge differences in terms of delivered dose distribution [9].

Finally, in the last decades progress was made in this field and several new techniques were implemented. Among them we have [9, 10]:

- **Intensity modulated radiotherapy (IMRT)**; Is defined as a *"a radiation treatment technique with multiple beams incident from different directions in which at least some of the beams are intensity-modulated so that each beam intentionally delivers a non-uniform dose to the target."*. Differently from uniform beams, it allows to create homogeneous concave dose distributions thanks to a fluence that is a function of its geometrical location inside the cross section of the beam. Without such a technology, if the tumour bends around organs at risk (OARs), the clinical target volume (CTV) will have a concave surface that will lead to a concave planning target volume (PTV). The dose in this case may be limited to unacceptable dose values in the OARs, making the treatment useless. In general, the IMRT is implemented through inverse planning computer algorithms that are able to convert a desired dose distribution into beam intensity maps to be then delivered by a properly equipped radiotherapy machine. An additional refinement of this technique foresees the replanning and/or the optimization of the treatment plan during the course of radiotherapy when clinically relevant by means of several imaging techniques. In this case we talk about *Adaptive Radiotherapy* (ART).

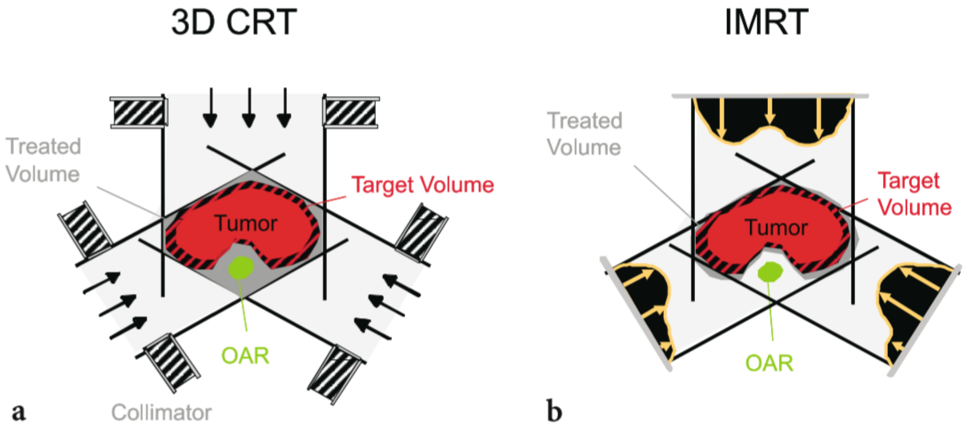

Figure 1.2: Comparison of 3D Conformal Radiotherapy and IMRT when dealing with a concave PTV. A, 3D Conformal Radiotherapy. B, Intensity Modulated Radiotherapy. [10]

- **Hadron therapy**; aims at exploiting the beneficial shape of heavy ions dose-deposition curves.

Today, radiation has found also many industrial applications. Among them [11]:

- **Sterilization**; as opposed to chemical processes and physical hot processes, that could cause damages and leave residues, sterilisation can be considered a physical cold process that preserves the materials. Moreover, if the dose is properly controlled, activation phenomena can be avoided. It involves panoramic irradiator containing γ emitting radioisotopes as sources. The dose that needs to be used in order to achieve a desired bacteria survival probability depends on the material properties, the amount and kind of bacteria and the temperature.

- **Mine detection**; the use of radiations allow to identify small Anti Personal Mines (APM) with a good accuracy, discriminating the numerous false positive signals that arise from a metal detector in these situations. For instance, a physical phenomenon that can be exploited is the *Neutron Induced γ Emission.* After a neutron capture reaction, the nucleus can de-excite through a γ emission that can be correlated with the soil composition. In this way the ratio (H:O:C:N) can be evaluated and the presence of explosives can finally be forecasted.

Chapter 2

Radiation therapy

Radiation therapy (from now on will be just “RT”) can be defined as a *“treatment modality based on the use of high energy rays or radioactive substances to damage tumoral cells and to halt their growth and division”* [9]. Depending on the localisation, size and type of cancer, the treatment can be executed using a radioactive source that is external or internal to the body.

The RT, used alone or in combination with other treatments, is an extremely important therapeutic tool that is adopted to treat cancer. In fact, considering RT as a unique treatment or as a part of a complex therapeutic protocol, it is estimated that about two-third of all patients affected by cancer will receive it.

The ultimate goal of the radiotherapy is to treat the tumour and spare the healthy tissues and organs that surrounds it. This can only be fulfilled if the therapeutic absorbed dose is delivered to the tumour reliably from day to day during the entire course of treatment.

There are two main types of radiation actually involved in RT: the electromagnetic (X-rays and γ rays) and the particulate ones (electrons, neutrons and ions). Among them, ion beams have unique biophysical and radiobiological properties. For instance, compared to photon beams they have an inverted depth dose profile and a different “efficiency” in killing biological cells (that is well described by the so called Relative Biological Effectiveness). These unique characteristics on one hand are favourable because they allow to treat tumours efficiently, but on the other hand they impose greater efforts to reduce uncertainties in the whole treatment delivery process.

Irrespective of the kind of radiation, after its interaction with the biological tissues numerous effects could arise:

- Physics effects → transfer/absorption of energy

- Biophysics effects → ionisation and excitation phenomena
- Physical/Chemical effects → direct alterations of atoms and molecules / indirect damage due to free radicals production
- Chemical → breaking of bonds, polymerisation or depolymerisation phenomena
- Biochemical → alteration at the molecular level
- Biochemical/Biological → damage to DNA, RNA, cytoplasm, enzymes
- Biological → damage to the genetic material, metabolic lesions...

Among these effects, there are two main mechanisms that could be exploited to kill tumour cells and to halt their reproducing ability:

- Direct effects: most commonly present in case of particulate radiations. DNA or other important molecules are directly damaged by the radiation itself. The molecular structure is disrupted, and this structural change leads to cell damage or even cell death. Direct effects are predominant with high-LET radiations such as α particles and neutrons at high radiation doses.
- Indirect effects: caused by the free radicals that are produced during the interaction of radiation with biological tissues. Since the major biological constituent is water, when radiations hit the water molecules, free radicals such as perhydroxyl and alkoxy are produced. They are characterised by an unpaired electron that makes them very reactive; interactions with the biological environment can cause damages. Since the water accounts for about the 70% of the cell composition, it has been found that the indirect effects is responsible for the majority of the radiation induced damages. [15]

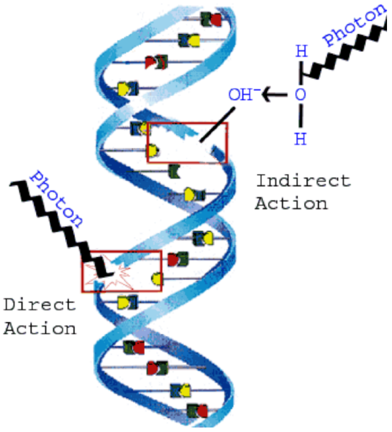

Figure 2.1: Indirect and direct effects on the DNA [28]

.

However, not only the tumour will be affected by the radiation beam; all the surrounding tissues will be affected by it. So, since the first usages of RT for clinical purposes, great efforts have been made to reduce these risks as much as possible [9].

The treatment planning aims at determining the most appropriate way to irradiate the patient given a prescribed dose to the tumour and dose limits to the surrounding healthy organs. So, the definition of the tumour, adjacent organs at risk (OAR), and other anatomical structure is an essential part of the entire planning process. As a result, according to the *ICRU Report 50 (1993)* different volumes need to be identified in each treatment planning process [12]. Among them, there are:

- Gross Target Volume (GTV): it contains all the macroscopically detectable portions of tumour tissues. In general it is defined by the oncologist using clinical imaging. However, in certain cases even the modalities with the best tissue contrast may not resolve the tumour shape with enough precision.

- Clinical Target Volume (CTV): since the GTV may not comprise all the tumour tissues, a margin is applied to it to account for any microscopic extension of the primary tumour. It can be defined in different ways, but in all cases it must receive the prescribed radiation dose.

- Planning Target Volume (PTV): it contains the CTV and all the structures and healthy tissues in proximity that can be interested by the radiation field due to all the uncertainties in the planning. Usually it is the final volume defined by the clinician during the planning process and it should ideally be determined from an uncertainty analysis. The final aim of this additional volume is to ensure that the whole CTV will receive the prescribed dose.

- Organ at Risk Volume (OAR): to avoid secondary syndromes all the potentially exposed organs that are adjacent the PTV needs to be highlighted in order to check if the dose that they will receive is lower than the prescribed maximum. In fact, since they are outside the PTV, they do not contain malignant cell and they need to be preserved. The OARs that need to be considered vary from case to case depending on the location and size of the PTV.

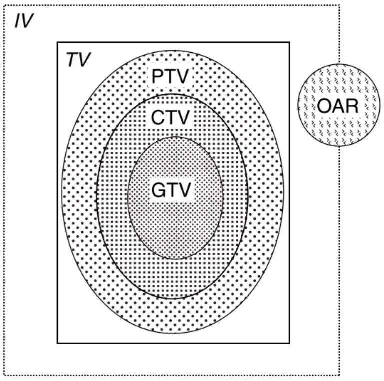

Figure 2.2: Treatment Planning System volumes definition [12]

.

It is important to bear in mind that a typical treatment workflow is composed of several steps and each one is associated with some uncertainty:

1. Conversion of CT images to physical quantities: uncertainties due to possible wrong conversion coefficients or resolution limits.
2. Delineation of the target volume together with margins: uncertainties due to contouring accuracy, setup accuracy, motion management, internal organ movements.
3. Dose prescription.
4. Treatment planning: uncertainties in beam modelling, dose calculation.

5. Treatment delivery: uncertainties due to patient's anatomy changes, machine output and patient motion.

In the next sections the physics of the main phenomena involved in the radiation therapy are analyzed. Then, a particular focus on the proton therapy and on the in-vivo dose delivery assessment problem is made.

2.1 Physics of radiation therapy

In general, the word "radiations" refers to electromagnetic radiations of any wavelength. However, among them the ones of interest in radiation therapy are the so-called *ionising radiations*. The word "ionising" refers to their capability of ionise the matter through interactions; to do so, they must be sufficiently energetic. Such radiations include both electromagnetic (X-rays and γ rays) and particulate radiations ($neutrons, e^-, p^+, heavyions\ldots$).

Since their modalities of interaction with the matter are completely different, a major distinction between charged and neutral particles need to be made.

Photons and neutrons through their interactions mainly produce secondary charged radiation. The *biological effects* induced by the ionising radiations are often caused by the charged particles. Consequently, the latter are often called *directly ionising radiations* while photons and neutrons are called *indirectly ionising radiations* [12]. For charged particles, different interaction mechanisms can be identified:

- Inelastic collisions with bound atomic electrons: this mechanism is important for both light and heavy charged particles. It both causes transfer of energy to matter and a change on the momentum of the projectile (that is more pronounced for light particles). If the energy transfer to the bound atomic electrons is high enough, they can be emitted with sufficient energy to create their own track. In that case they are called δ-rays [12].

- Elastic collisions with heavy nuclei; this mechanism is relevant for both light and heavy charged particles and for heavy particles it is known as *multiple coulomb scattering (MCS)*. It causes only a modification on the direction of travel of the projectile.

- Radiative losses (Bremsstrahlung); when a charged particle is accelerated in a strong electric field, it emits photons. This effect is relevant only for light charged particles in mediums with a high atomic number.

- Nuclear reactions; relevant only for heavy charged particles with enough energy to interact directly with the target nucleus through an inelastic collision. These interactions are important in radiotherapy because the passage of heavy ions through an absorber could produce a significant amount of lighter reaction products even if the cross sections for this kind of interactions are low. Moreover, nuclear interactions could cause tissues activation though the production of radioactive nuclei that are positron emitters. Research is ongoing to exploit the radioactive nature of these nuclei for in-vivo dosimetry using imaging techniques such as the positron emission tomography (PET) [15].

Their contribution varies depending on the energy and on the material in which the radiation is being transported. However, it can be argued that the main interaction mechanism that finally causes energy deposition in the materials at the energies of interest in radiotherapy (from few hundred eV to hundreds of MeV) is the coulomb interaction with the bound atomic electrons.

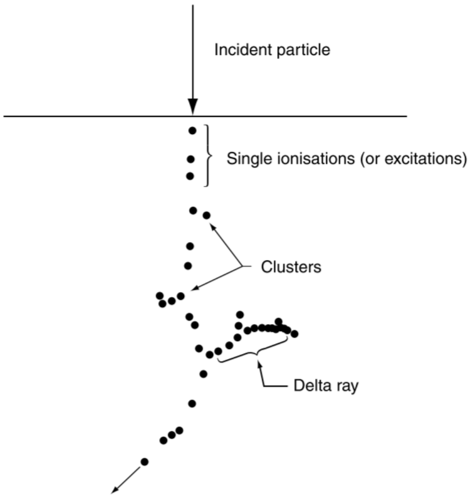

Figure 2.3: Representation of the track of a charged particle in matter [12]

.

While charged particles lose their energy “gradually” due to a huge number of interactions per unit path length, photons interact only a few times. For this reason, when dealing with charged particles the concept of *stopping power* is often used to approximate in a continuous manner their energy loss behaviour. So, we say that charged particles “slow down” when passing through materials. Each interaction mechanism will contribute to the stopping power to a certain extent.

For photons, we use the term "attenuation" to describe the behaviour of the beam. Also in this case, each interaction mechanism will contribute to the beam attenuation in a different extent. The main contributions arise from:

- Photoelectric absorption: in this process the photon is entirely absorbed following the interaction with an atom. As a result, an electron is ejected from one of the atomic shells with a kinetic energy given by:

  $$T = h\nu - E_B \tag{2.1}$$

  Where h is the Planck's constant, ν is the frequency of the incident photon (so, $h\nu$ is the energy of the photon) and E_B is the binding energy of the atomic electron. Actually, due to momentum conservation, part of the energy is transferred also to the atom. However, since the atom is heavy compared to the electrons, it can be neglected. In addition, the photoelectric absorption could be followed by the emission of characteristic X-rays whom afterwards could trigger the emission of another electron from an inner shell that will be called *Auger electron.*

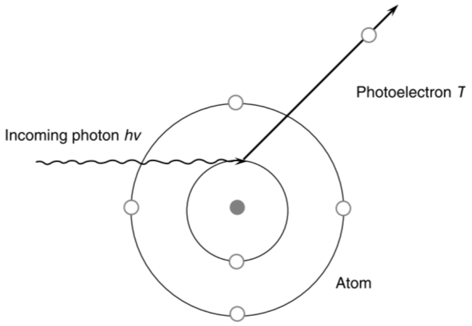

Figure 2.4: Representation of the photoelectric absorption [12].

In general, the cross section (that can be interpreted as the probability of interaction) for the photoelectric absorption increases with decreasing photon energy. Moreover, at energies corresponding to the binding energies of the electrons *absorption edges* are present. In fact, as soon as the energy of the incident photon gets bigger than the binding energy of a given electronic shell, more electrons become available for the absorption process, leading to a sudden increase in the probability of this kind of interaction.

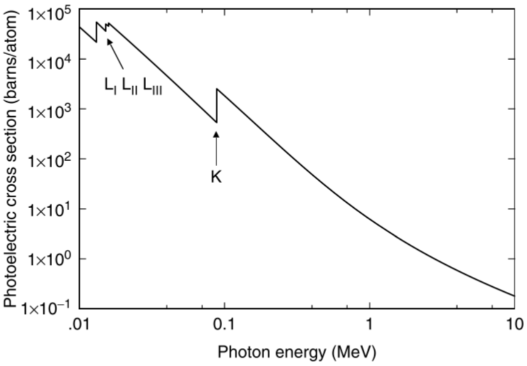

Figure 2.5: Representation of the photoelectric absorption cross section in lead. The position of the L_I, L_{II}, L_{III} and K absorption edges are indicated [12] .

Finally, it is worth to underline the strong dependence of the photoelectric absorption cross section on the atomic number of the target material Z. Above the K absorption edge, the photoelectric absorption cross section is approximately proportional to $\frac{Z^4}{(h\nu)^3}$. This explains why bones offer high beam attenuation in X-ray imaging [12].

- Rayleigh scattering: in this case the energy of the photon remains constant. Only the direction of the motion changes and the process is also called “elastic scattering” or “coherent scattering”. This kind of interaction is dominant when the energy of the photon is sufficiently low so that the binding energies of the atomic electrons cannot be neglected. In that case, the photon can scatter also from all the bound electrons together.

- Compton scattering : this process is also called “incoherent scattering” because, in addition to the change of the photon direction following the interaction, its energy also decreases due to the emission of a recoil electron (Fig. 2.6). This process dominates on the “coherent scattering” when the energy of the photon is higher than the binding energies of the atomic electrons.

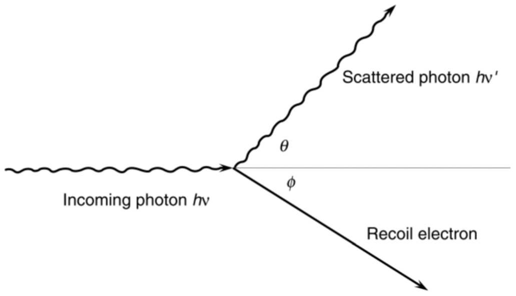

Figure 2.6: An incoming photon of energy $h\nu$ scatters to produce a scattered photon of energy ($h\nu' \leq h\nu$) and a recoil electron [12] .

- Pair production: if the energy of the photon is higher than $1.02MeV$ it can be absorbed in the electric field of the nucleus. Its energy will contribute to the creation of an e^- -e^+ pair. The kinetic energy of the created pair can be determined by applying a simple energy balance:

  $$T^- + T^+ = h\nu - 2m_0c^2 \tag{2.2}$$

  Where $m_0c^2 \approx 1.02MeV$ is the energy equivalent of the electron rest mass m_0. Obviously, the cross section of this process is 0 below the threshold energy, it then increases rapidly becoming dominant at high energies [12].

The relative contribution of each interaction mechanism to the attenuation of the beam depends on the photon energy and on the atomic composition of the medium in which it is being transported. Two useful plots of this dependence are reported in Fig. 2.7 and Fig. 2.8. In MV radiotherapy the dominants effects are pair production and Compton scattering.

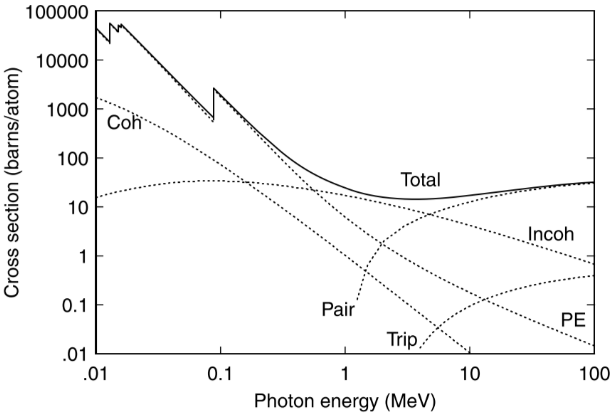

Figure 2.7: Photon attenuation cross sections in lead [12]

.

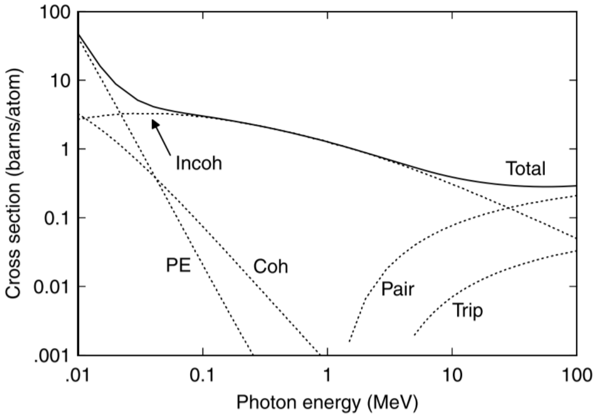

Figure 2.8: Photon attenuation cross sections in carbon [12]

.

After having characterised the way radiations interact with the matter, from a dosimetric point of view it is important to introduce the *LET (Linear Energy Transfer)* and the absorbed dose. The LET gives us the amount of energy that is actually deposited in the medium by the radiation per unit path length. It reflects the rate at which ionisation is produced along the track of charged particles. It is related to the stopping power, but it is not exactly the same. In fact, even if the stopping power includes all the interactions that lead to an energy loss, such energy loss may not be entirely deposited in the medium in the point in which the interaction has occurred. For instance, interactions with a high energy loss may produce secondary particles with their own track (e.g. δ rays) that will deposit the energy far away from the initial point of interaction.

So, the LET is in general defined by setting an energy threshold Δ that excludes from the computation all the interactions that could lead to a too high energy exchange. For charged particles it can be defined as:

$$LET_{\Delta} = (\frac{dE}{dx})_{\Delta,col} \tag{2.3}$$

Where $(\frac{dE}{dx})_{\Delta,col}$ represents the "collision" contribution to the stopping power and Δ is the energy threshold for the production of δ rays. The "radiative" contribution to the stopping power (e.g. bremstrahlung) is obviously omitted since the energy will be for sure deposited far away.

Moreover, this definition of LET supposes that the energy deposition is well described by the continuous slowing down approximation (CSDA). However this is an approximation; the stopping power is an averaged measure of the energy loss along the track and, due to the intrinsic stochastic nature of the radiation transport, the energy straggling phenomenon is always present.

After having defined the LET, the definition of the absorbed dose (D) is straightforward. We will consider the non-stochastic absorbed dose; it means that we are considering a mass element sufficiently large to neglect fluctuations of the energy deposition due to its intrinsic stochastic nature. In fact, when the mass element is in the microscale it is necessary to consider an absorbed energy probability distribution and the stochastic nature of such energy deposit becomes extremely important. Consequently, considering identical irradiations, the dose deposited in a microscopic volume is not always the same, while if the volume is sufficiently large it can be considered relatively constant between irradiations. This fact becomes important in medical physics because the working domain of a tumour tissue is of the order of $10^{-6}m^3$ or less [33]. As a result, two stochastic quantities have been defined and their characteristic behaviour is depicted in the Fig. 2.9:

- The tumour control probability (TCP)
- The normal tissue complication probability (NTCP)

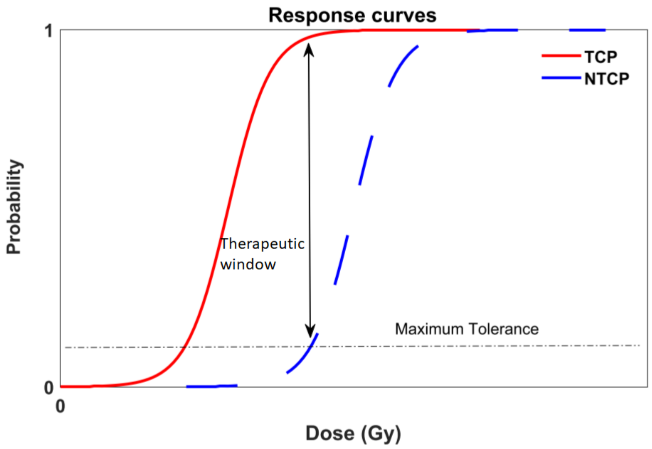

Figure 2.9: Example of response curves for TCP and NTCP [33] .

The aim of radiotherapy is to achieve a high probability of local tumour control (TCP) with a low risk of normal tissue complications (NTCP).

Coming back to the non-stochastic absorbed dose, it has been defined by the ICRU in 1951 as "the quotient $\frac{d\bar{\epsilon}}{dm}$, where $d\bar{\epsilon}$ is the *mean* imparted energy deposited by a ionizing radiation in a material of mass dm ".

$$D = \frac{d\bar{\epsilon}}{dm} \tag{2.4}$$

It has the dimensions of an energy (J) divided by a mass (kg). Such unit of measure has been called *Gray [Gy]*.

Since the mean LET value strongly affects the biological effects), it is useful to categorise the ionising radiations according to it (Fig. 2.10):

- Low LET radiations: sparse ionisation is present along their track.
- High LET radiations: dense ionisation is present along their track.

Low LET	**LET** [keV/µm]	**High LET**	**LET** [keV/µm]
X-rays 250kVp	2	Electrons 1MeV	12.3
γ-rays ^{60}Co	0.3	Neutrons 14MeV	10
X-rays 3MeV	0.3	Carbon Ions 100MeV	160
Electrons 10keV	2.3	Heavy ions	100-2000

Figure 2.10: Radiations classification based on mean LET values [11] .

High-LET radiations are more destructive to biological material than low-LET radiations because they transfer energy in a limited area of the cell creating well localised DNA damage, while the latter transfer energy in a wider zone (leading to a sparse formation of free radicals, Fig. 2.11). So, high LET radiations generally are responsible for the so called *direct effects* whilst the low LET radiations are responsible for the *indirect effects* [13].

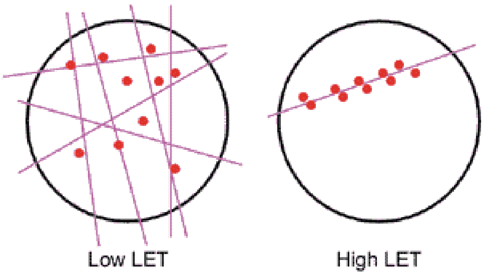

Figure 2.11: In both cases the same total number of ionisations is present. The dose deposited in the volume is the same, but the biological effects will be different [13] .

It is worth to underline the main mechanisms that lead to the formation of free radicals in aqueous mediums:

$$\begin{aligned}
&H_2O + Radiation \rightarrow H_2O^{+} + e^{-}\\
&H_2O + e^{-} \rightarrow H_2O^{-}\\
&H_2O^{+} \rightarrow H^{+} + OH^{\circ}\\
&H_2O^{-} \rightarrow H^{\circ} + OH^{-}\\
&RH + OH^{\circ} \rightarrow R^{\circ} + H_2O\\
&RH + H^{\circ} \rightarrow R^{\circ} + H_2
\end{aligned} \tag{2.5}$$

The presence of oxygen can enhance such mechanisms leading to a chain effect and making the damages permanent:

$$\begin{aligned}
&R^{\circ} + O_2 \rightarrow RO_2^{\circ}\\
&RO_2^{\circ} + RH \rightarrow RO_2H + R^{\circ}
\end{aligned} \tag{2.6}$$

As a consequence, two parameters have been defined to take into account the different biological effects of the radiations and the role of the oxygen in the therapy effectiveness:

- The Relative Biological Effectiveness (RBE): it accounts for the cell killing efficiency of radiations. It compares the efficiency of different types of radiation to produce a given biological effect compared to a reference radiation. So, it is defined as the ratio between the dose that led to a given cell survival fraction (S) for a reference radiation (in general X-rays) and the dose that led to the same cell survival fraction for a given radiation of interest (e.g protons).

$$RBE_{rad} = [\frac{D_{X-ray}}{D_{rad}}]_{S_{X-ray}=S_{rad}} \tag{2.7}$$

The Fig. 2.12 is related to a cell line irradiated by photons and protons. It is clear that protons have a greater cell killing efficiency compared to photons. Typical mean RBE values are 1.1 for protons and between 2.5 and 3 for carbon ions. It is important to bear in mind that the RBE value depends also on the tissue characteristics, on the dose and on the particular biological effect under investigation [14, 15].

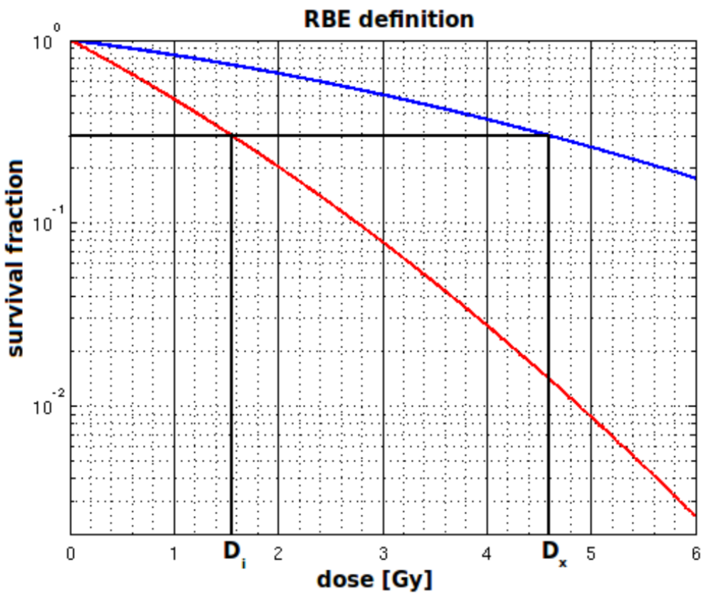

Figure 2.12: Cell survival fraction as a function of the Dose for X-rays (blue curve) and protons (red curve) [14]

.

- The Oxygen Enhancement Ratio (OER): it quantifies the role of the oxygen in the effectiveness of the therapy. Since it enhances the effects of free radicals, low LET radiations are more effective in its presence. Unfortunately hypoxic regions are present in many tumours and so their resistance to low LET radiations is high (Fig. 2.13). The OER is defined as the ratio between the dose that is required without oxygen and the dose that is required with a fully oxygenated biological medium to produce the same biological effect. It decreases as the LET increases and approaches 1 at approximately $150\frac{keV}{\mu m}$ [15].

$$OER = \frac{D_{hypoxic}}{D_{areated}} \tag{2.8}$$

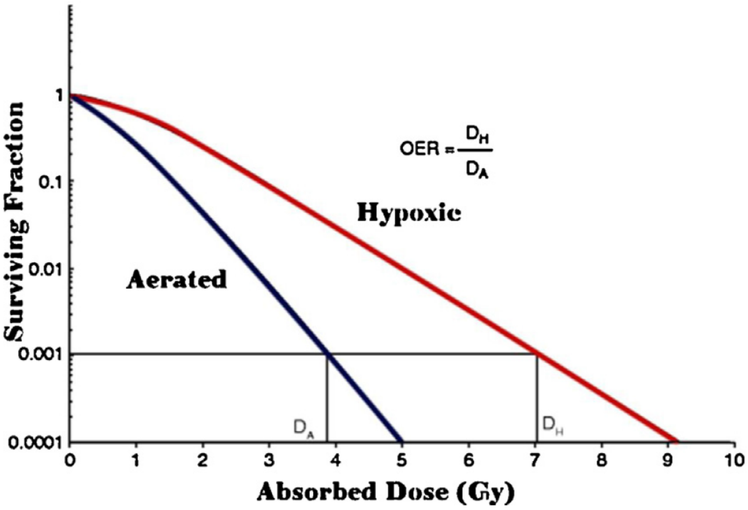

Figure 2.13: Effect of hypoxia upon cell survival fraction. Definition of the OER [15].

.

To summarize, the effects of ionising radiation are influenced by the dose, the dose rate, the mean LET of the radiation and the biological tissue type.

After having introduced all the main concepts that are involved in radiation therapy, to underline the reasons that are pushing researchers to find reliable in-vivo dosimetry solutions, in the following section proton therapy is deeply analysed.

2.2 Proton therapy

The use of proton (and heavy ion) irradiation in cancer therapy was proposed due to their unique radiobiological properties such as a higher

RBE, a lower OER and an inverted depth dose profile compared to photon beams. These properties are much more favourable than those of photon radiotherapy, hence proton therapy can be used to treat tumours more efficiently. Consequently, there is a significant interest in the medical use of such beams with energies generally ranging between 65 and 250 MeV [12].

In Fig.2.14 a comparison between the dose deposition profiles of photons (in particular, X-rays emitted by a linac operated at 6MV) and 250 MeV protons is shown. It is immediately noticeable that the latter allows the irradiation of deep-seated target volumes with an optimal precision and greater sparing of the surrounding healthy tissues and organs, while the former does not allow for an optimal dose distribution control [15]. Moreover, a typical photon beam produced in clinical linacs exhibits an increase of the dose distribution within the first few centimeters (phenomenon called *dose build-up*) followed by an exponential drop. The build-up is due to the fact that at the beginning the photon beam has a higher energy; this leads to the production of secondary electrons that are strongly forwardly scattered. Consequently, increasing the depth more and more secondary electrons will be present (the ones produced locally in addition to the ones coming from interactions at lower depths). This holds for the first few centimeters of penetration and rapidly leads to the so called “charged particles equilibrium”. Then, the attenuation of the photon beam becomes no more negligible and the dose starts decreasing in a condition that is often called “transient charged particles equilibrium”. So, for deep seated tumours. the dose delivered to the tumour using a single photon beam is in general lower than the dose given to the healthy tissues at lower depths [15]. This behaviour is absolutely not beneficial from the TCP and NTCP point of view.

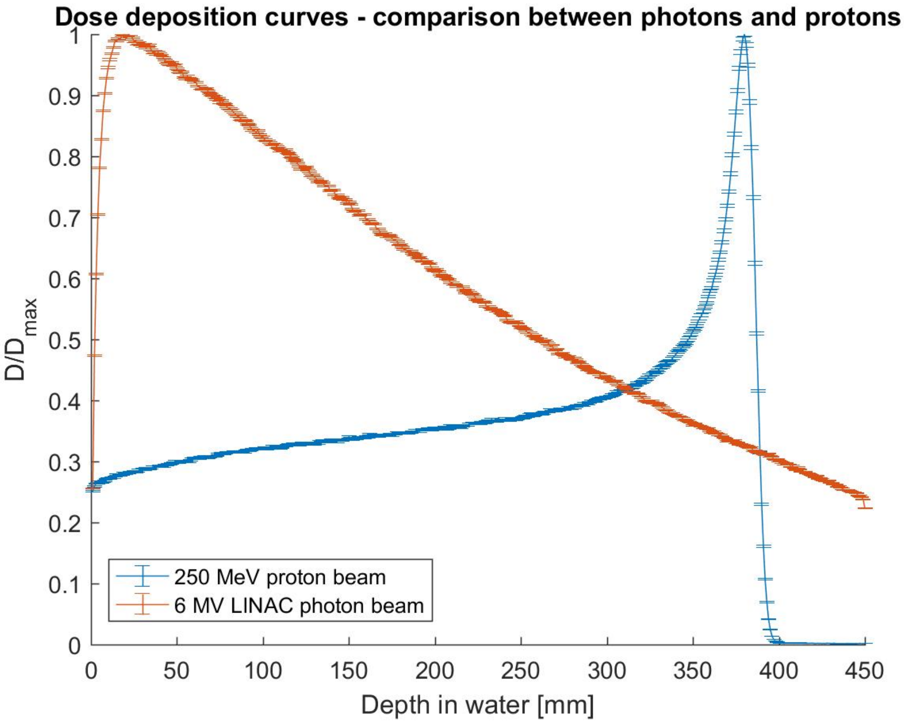

Figure 2.14: Photons and protons dose deposition profiles in water. Computed using Geant4.

The proton dose deposition curve has a peak called *Bragg Peak (BP)* that is located at a mean depth that depends on the initial energy of the beam and on the medium (Fig. 2.15). Such peak is characteristic of protons and of every heavy charged particle and is due to a significant increase of the collision cross section due to the reduction of the particle speed caused by the slowing down process. All these collisions cause a rapid energy deposit in a small volume, leading to a fast decrease of the primary particle energy. Moreover, since the Bremsstrahlung effect is negligible, the tissue beyond the BP receives little or no radiation dose. However, in case of heavier particles, secondary products of nuclear interactions could produce a significant tail beyond the peak. This could cause large undesired radiobiological effects that could limit their clinical application [12].

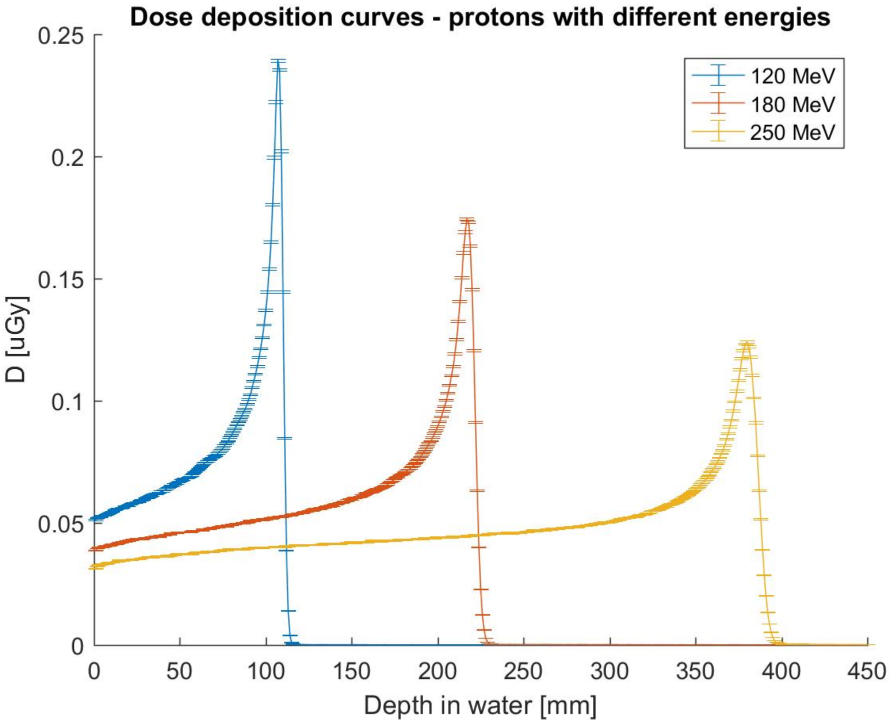

Figure 2.15: Dose deposition profile in water computed using Geant4 for proton beams with different energies.

This inverted dose deposition profile is the argument for the use of heavy charged particles instead of photons in tumour therapy [15]. Thanks to this feature protons allow, in principle, to deliver high doses to the tumour region whilst at the same time sparing surrounding healthy tissues. In general, in a typical treatment plan a single Bragg peak is not wide enough to cover the whole tumour; a summation of multiple peaks at staggered depths (Spread out Bragg peak - SOBP) is needed to broaden the coverage of the whole tumour (Fig. 2.16). At the end, a typical X-ray radiotherapy plan would always deliver a higher integral dose thus creating more damages to normal tissues compared to a proton therapy plan. The latter is able to deliver highly conformal radiation fields to target volumes; so, it is absolutely preferred for tumours with irregular shapes and/or placed around critical structures and for paediatric patients, where the NTCP is of main concern [21]. For instance, proton therapy has an ideal application in craniospinal irradiation (used to treat some brain tumours); the sharp dose fall-off dramatically decreases the dose to the bowel, lungs and heart compared with photon therapy [26].

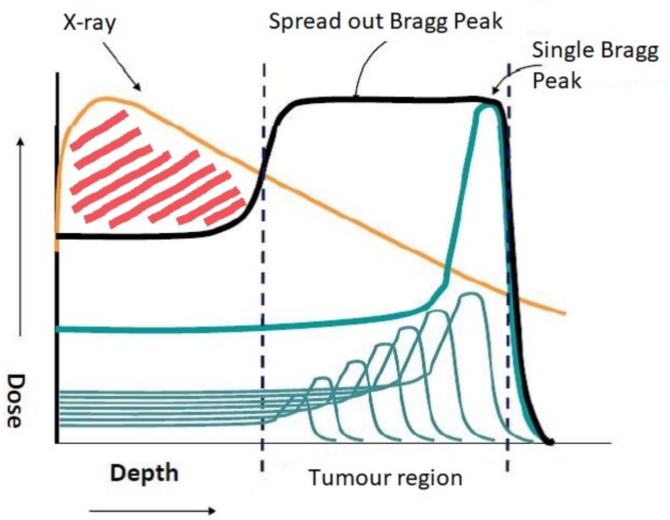

Figure 2.16: Spread out Bragg Peak illustration. The red area highlights the additional dose given to healthy tissues in case X-rays are adopted. Adapted from [18].

Two beam delivery modes are currently available for protons (Fig. 2.17) [24]:

- **Passive scattering** : In order to make the beam suitable for therapy, a broadening of the narrow proton beam that is extracted from the accelerator is needed. In this delivery mode, scatter foils are used for this purpose. Next, there is a range modulation wheel and finally, on the beam nozzle, the field is shaped using an aperture (for lateral dose conformation) and a range compensator (for distal conformation) and a range modulation device that allows the formation of the SOBP.
- **Active scanning**: In this case a narrow quasi mono-energetic proton "pencil" beam is adopted. The beam is is magnetically scanned across the target using a pre-defined beam energy. Then, after a first layer is "painted", the beam is turned off and its energy is changed step-wise. Successively, another layer is painted and this goes on until the Bragg peak is modulated in depth. This technique allows to achieve a greater target dose conformity , reduces the neutron contamination and requires no patient-specific hardware compared to the passive scattering technique. Moreover, it allows to deliver intensity modulated proton therapy (IMPT) that further enhances the dose conformity in the tumour region adopting multiple non-uniform treatment fields (in analogy with IMRT). However, this delivery mode is extremely sensitive to organ motion.

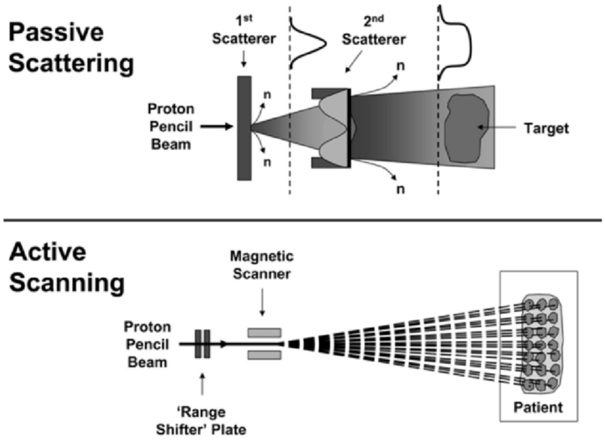

Figure 2.17: Comparison between passive scattering and active scanning methods [19].

However, as we learned in the previous section, there are lot of uncertainties that affect all the phases of the treatment planning workflow. In proton therapy such uncertainties arise mainly from [21, 23]:

- Treatment planning: CT noise, CT artefacts (huge in presence of metal implants), CT resolution (especially in heterogeneous geometries with high density and low density materials together), Hounsfield Unit (HU) conversion method [1], physics parameters (mean excitation energies, cross sections...).
- Treatment delivery: setup and positioning errors, organ motions, change of anatomical structures during the treatment period, drift in machine output and performance, RBE at low proton energies (due to LET uncertainties)

All these uncertainties will have an important impact on the dose distribution if a proton beam dose profile is involved. An estimate of their relative contribution using both analytical or stochastic methods to the overall range uncertainty for non-moving targets has been reported in the following table:

---

[1] If the treatment planning system is based on analytical pencil-beam dose calculation algorithms, empirical HU conversion schemes are used to translate CT scans into relative stopping powers that are used to project the range based on the water-equivalent depth method. That method neglects the position of the inhomogeneities relative to the Bragg Peak depth and, compared to the Monte Carlo method, has greater uncertainties in complex geometries. However, also Monte Carlo codes are affected by such conversions since they are used to get information about densities and materials composition. For more details, the reader is referred to [21, 33, 23].

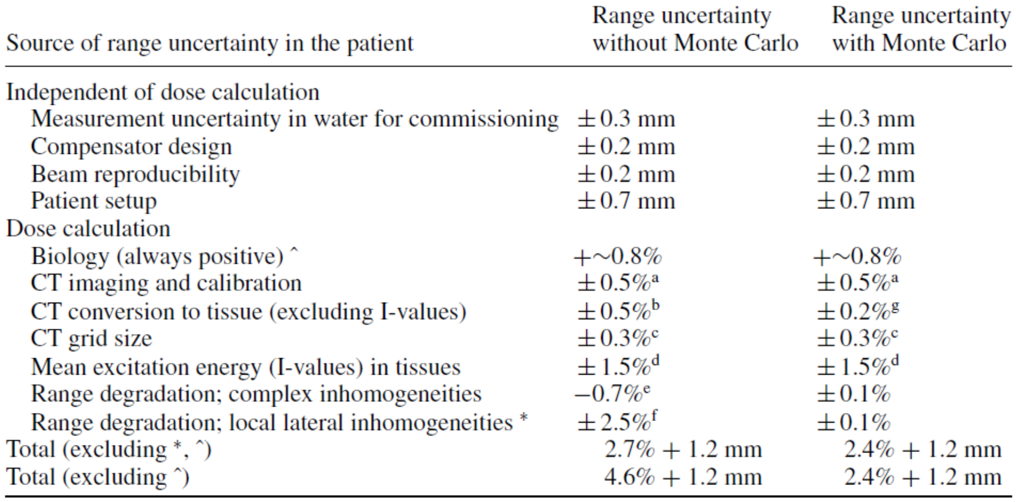

Source of range uncertainty in the patient	Range uncertainty without Monte Carlo	Range uncertainty with Monte Carlo
Independent of dose calculation		
Measurement uncertainty in water for commissioning	±0.3 mm	±0.3 mm
Compensator design	±0.2 mm	±0.2 mm
Beam reproducibility	±0.2 mm	±0.2 mm
Patient setup	±0.7 mm	±0.7 mm
Dose calculation		
Biology (always positive) ˆ	+∼0.8%	+∼0.8%
CT imaging and calibration	±0.5%^{a}	±0.5%^{a}
CT conversion to tissue (excluding I-values)	±0.5%^{b}	±0.2%^{g}
CT grid size	±0.3%^{c}	±0.3%^{c}
Mean excitation energy (I-values) in tissues	±1.5%^{d}	±1.5%^{d}
Range degradation; complex inhomogeneities	−0.7%^{e}	±0.1%
Range degradation; local lateral inhomogeneities *	±2.5%^{f}	±0.1%
Total (excluding *, ˆ)	2.7% + 1.2 mm	2.4% + 1.2 mm
Total (excluding ˆ)	4.6% + 1.2 mm	2.4% + 1.2 mm

Figure 2.18: Estimated proton range uncertainties and their sources and the potential of Monte Carlo for reducing the uncertainty. The estimations are average number based on 1.5 standard deviations. Adapted from [23].

To emphasize their impact, suppose to put a 2 cm air gap between the beam and the tumour target and see how the dose profile changes in both proton and photon beam cases (Fig. 2.19 and Fig. 2.20):

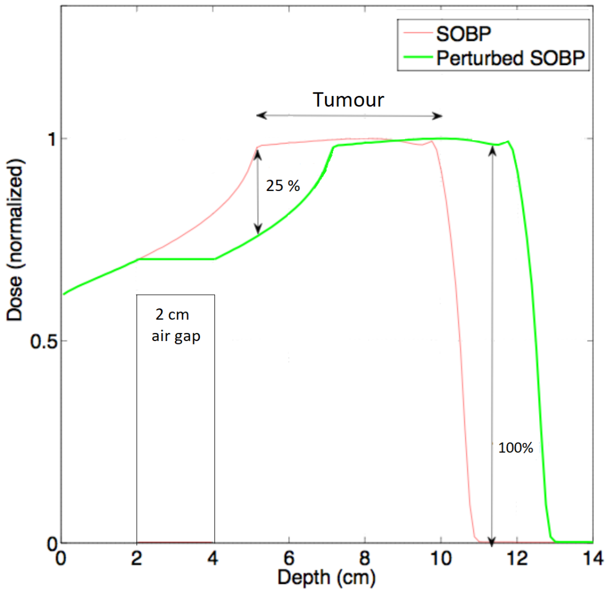

Figure 2.19: Dose deposition profile with and without a 2 cm air gap between the beam and the tumour region [28].

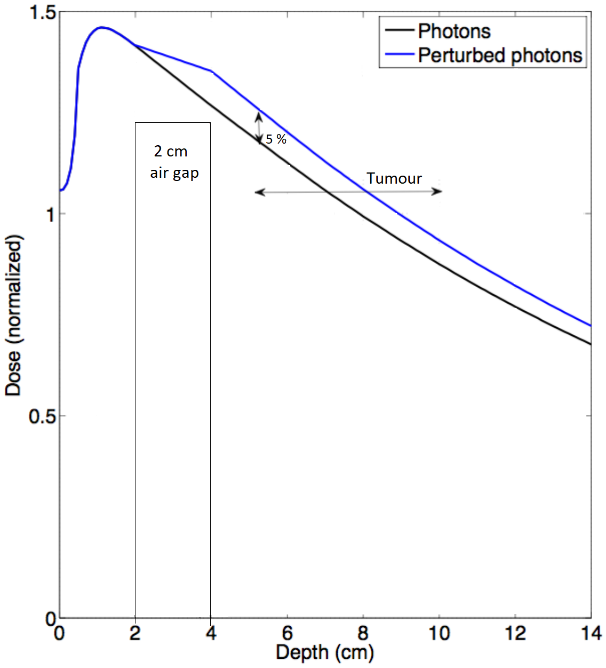

Figure 2.20: Dose deposition profile with and without a 2 cm air gap between the beam and the tumour region [28].

While in the case of a photon beam such air gap makes small differences (but still, they should be assessed in a treatment quality assurance protocol even if the gain might be small compared with the additional workload and costs involved[20]), the impact is much more significant for proton beam delivery. The proximal tissues will receive up to 25% overdose and, due to a range increase, some distal volumes will receive 100% of the maximum dose instead of being spared. So, despite the advantageous dose deposition profile of protons, the direct aim of a proton beam against critical structures is rarely done in practice since it could cause serious damages, both decreasing the TCP and increasing the NTCP [24].

Consequently, proton therapy is very sensitive to uncertainties introduced during the entire treatment planning and delivery procedure. A range error could lead to under-shooting of a portion of tumour and over-shooting of healthy tissues. To partly avoid these consequences, when it is possible alternative non-optimal beam arrangements are adopted as it is shown in Fig. 2.21.

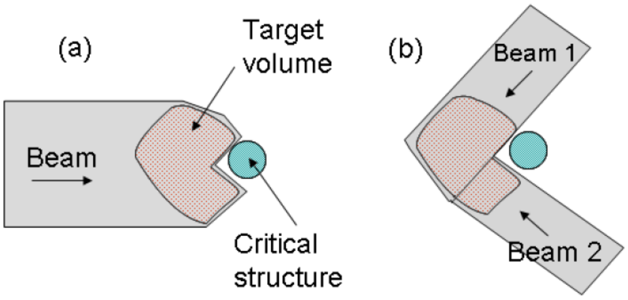

Figure 2.21: a. The optimal beam arrangement of one proton beam stopped in a target volume right in front of a critical structure. b. A conservative beam arrangement to avoid possible damages to the critical structure [21].

Moreover, to account for such uncertainties a distal margin recipe that depends on the proton therapy facility is always included in treatment protocols (e.g. 3.5% of range + 1 mm at the Massachusetts General Hospital [23]), but this increases the dose imparted to healthy tissue (e.g. 8 mm overshoot for a 20 cm range beam) thus reducing the benefits of such treatments [22]. Such increase in the prescribed range is based on an overall estimation of the range uncertainty in typical treatments and, as we can notice from the table 2.18 in general it is still conservative with respect to such estimations. Reducing the uncertainties would allow to fully exploit the advantages of proton therapy.

To conclude, the range uncertainties limit to a great extent the potential of such techniques, and are their major drawback. Reducing such uncertainty would allow to fully exploit the advantages of the proton therapy, achieving an optimal treatment volume, hence decreasing the NTCP. So, it would be extremely desirable to measure proton ranges directly in-vivo and this is the reason why researchers have started looking for reliable methods to reach that goal in the last years.

2.3 In-vivo dose delivery assessment: state of art

The verification of delivered dose distribution during treatments is of paramount importance. In particular, as we have seen, it is almost mandatory to completely exploit the benefits of the proton beams and of the innovative heavy ion beams. For the following discussion, proton beams will be taken as reference.

Since, unlike photons, protons stop completely in the body, direct in-vivo treatment monitoring is definitely challenging. To accomplish this aim, several techniques have already been proposed and the AMPHORA project is investigating a new, innovative concept. Such techniques can be broadly classified in invasive and non-invasive techniques. An example of invasive technique is the so called *point dose method*. It has been widely used for verifications in photon/electron treatments. However, when measurements at the skin level are not sufficient, it foresees to implant detectors inside the human body. Moreover, it is not trivial to adopt when proton beams are involved since it requires splitting an SOBP field into two opposite subfields "sloped" in a prescribed way. This will allow to retrieve the water equivalent path length at the dosimeter location by means of the ratio between the two distributions with just one point measurement. However, this can be easily done only for machines that adopt *active scanning systems* while for the majority of machines that adopt *passive scanning systems* completely new hardware must be made [21, 24, 25]. In addition, this method presents several limitations:

- It can only verify the range at a limited number of points. In case of tissue inhomogeneities along the beam path a higher resolution is needed and this would no longer be sufficient.
- Tissue inhomogeneities may distort the depth-dose "slope" obtained from water tank measurements.
- The implantation of dosimeters may not be possible for all the tumours.

From now on, we will focus only on non-invasive in-vivo proton range verification methods. The following is a brief review of the state of art methods currently being proposed, developed or that are already clinically implemented:

- **Range probe**: This method can be viewed as an alternative to the 1D point dose method which does not involve the implantation of a dosimeter. It is based on the measure of the residual range of a single proton pencil beam with sufficient energy to pass completely through the patient. So, using a commercial multiple layer ionization chamber (MLIC) the complete Bragg peak can be measured. Through Monte Carlo simulations it has been shown that such technique can lead to in vivo range estimates at the 0.5% precision level [24]. Moreover, the dose delivered to the patient is very low since it comes from the plateau region; this allows to use multiple range probes from different directions hence obtaining a low-resolution *proton radiograph.* Main drawbacks of this technique are:

  - It requires high energy protons (higher than 250 MeV), therefore increasing the overall cost of the proton therapy facility.
  - The spatial resolution is poor (due to the multiple coulomb scattering which produces uncertainties in the reconstructed proton trajectory)
  - Only the total range change through the patient can be measured (computed range uncertainties can be considered as “worst case”).

- **Proton radiography and tomography**: It is the 2D extension of the range probe concept. Here a 2D proton fluence is adopted and the main goal is to obtain an higher spatial resolution through a simultaneous detection of the entrance and exit coordinates of each proton together with its range measurement. This technique has been investigated since the late 1960s, but it has not progressed rapidly mainly due to source availability and cost; in fact the beam needs specific characteristics in order to achieve a sufficient range measurement accuracy (e.g. intensity, energy spread, energy...). This technique gives also low dose to the patient allowing imaging before each fraction of the treatment. Moreover, the most interesting fact is that it has a two-fold benefit; it allows not only to estimate the proton range, but it can be used also in the treatment planning process to provide directly measured stopping power values of the tissues involved, thus avoiding the uncertainties due to the HU conversion from CT scans. For this reason, currently the main interest for this technique arises from its 3D applications (proton tomography) for treatment planning purposes [24].

- **Prompt gamma imaging**: It exploits prompt gamma emission produced by the target nuclei de-excitation that follows interactions with protons and was first proposed in 2006. Such interactions occur along the whole proton penetration path, until the energy of the proton becomes too low (generally 2-3 mm before the Bragg peak). Thus, the measurements of prompt gammas can be used to assess the range of protons. Moreover, it gives high count rates hence reducing the statistical uncertainty on measurements; even with a therapeutic dose rate of $\approx 2\ Gymin^{-1}$ it is possible to perform real time dose verification during the treatment, avoiding additional dose to the patient. Most of the emissions are in the 2-15MeV range and this has thwarted the development of this technique for years since there were no practical detectors available in that range; in fact, conventional detectors used for single photon emission tomography (SPECT) are not feasible since they would need to be too thick to detect high energy gamma rays. However, using a custom-built prototype detector, an accuracy of 1-2 mm was predicted through Monte Carlo simulations by several research groups, confirming the first estimate that has been given in 2006 [24].

Luckily several promising results on the development of suitable detectors have been obtained in the last years; numerous groups are working on a clinically suitable detector system. Indeed, first clinical results have been achieved in 2017 within a brain proton therapy treatment in pencil beam scanning mode using a prototype prompt gamma camera [22]. The recorded depth-dose profiles of individual pencil beam spots have been compared with the ones obtained by simulations during the treatment planning. Since the prompt gamma emission happens in a time scale of about 1 ns after excitation, it is possible to associate each gamma in the signal to a particular proton pencil beam spot. So, at the end, this technique allows to measure the shift in Bragg peak position with respect to the one predicted by the treatment planning system. However, the prompt gamma detection system is also subject to both random errors (Poisson noise, camera positioning errors) and systematic errors. So, the distinction between errors and actual peak shifts is difficult due to the lack of an absolute reference baseline. However, an overall precision of around 2 mm seems to be achievable and it is already better than the range uncertainty margin currently applied in the treatment plan process [22].

- **PET imaging**: Imaging techniques based on the positron emission tomography have been used at several institutions as a proton range verification tool and currently it is the most widespread method [23]. At least in principle, it is similar to the prompt gamma imaging method, but the physical phenomena that are exploited are different. In particular, it makes use of coincident gammas resulting from annihilation of the positrons emitted by the positron emitters which are created following proton nuclear reactions (positron emitters like C^{11} , N^{13} and O^{15} are created). This technique is appealing since it allows to retrieve information on the proton ranges without additional dose to the patient and because the emitted gammas can be easily detected in coincidence using a standard PET camera.

However, the target activation strongly depends on its elemental composition; so, the relation between the induced activity distribution and the imparted dose can't be easily retrieved. In addition, the activity distribution is strongly affected by the threshold energies for the production of the β^+ emitters. Hence, the fall-off of the activity distribution is shifted with respect to the dose fall-off. Then, it is also necessary to consider the time dependence of the biological wash-out related to the β^+ emitters that are produced. Consequently, it is not possible to verify the range directly comparing the dose and activity profiles; however, it is possible to do that through a comparison between the measured activity distribution and a modelled one, in which MC simulations are typically involved. In general, in order to take into account the biological wash-out of the induced β^+ emitters functional information must be used in CT-based Monte Carlo simulations. The main issue is related to the uncertainties of such simulations, that at the end will rely on cross section data, on information about materials taken from a CT scan and on the adopted biological wash-out model (the biological wash-out could change from day to day and it has not been well understood); it is estimated that in order to get an accuracy of about 1 mm such simulations should be properly fine tuned [24]. So, in the end this approach is mainly limited by the restricted knowledge about the elemental composition and the wash-out processes of different human tissues.

Nevertheless, even if the clinical benefits of such approach are still debatable since it is often difficult to extract quantitative information about the dose distribution, this approach has already been clinically implemented in some institutes. It has been demonstrated that it works best for intracranial and cervical spine target sites. For instance, for head-and-neck patients it has been claimed that it is possible to assess the beam range with an accuracy of 1-2 mm by proper co-registration with bony structures [24, 21]. However, this approach cannot provide the same accuracy in all the positions.

A comparison between this method and the prompt gamma imaging reveals that the latter has an enhanced count statistic and it avoids all the problems related to the biological wash out whilst the PET imaging is favoured by the commercial availability of suitable detectors but it is still not sufficiently reliable.

- **MRI imaging**: It has been shown that also a magnetic resonance imaging done after the treatment can reveal dose distribution information analysing physiological changes in tissues [23]. In fact, radiation can cause changes in the constitution of tissues that are sufficiently marked to be detected by MRI. Such detectable changes have been reported in the bone marrow after spine treatments and in the liver [24].

  However, since the location of the greatest signal intensity gradient does not correspond to the delivered dose gradient, a visual inspection of the MRI images alone is not enough to deduct useful information about the range of the protons. Consequently for each physiological change that is exploited there is a need of a dose-response curve that has to be determined experimentally; this is the main drawback of this technique since there is no guarantee that it's actual shape will be always the same for each patient. Moreover, the time that is needed for the induced tissue changes to be completed can be up to months and it is also patient-specific; so, this technique is suitable only as a posteriori verification method, hence it can't be used to adapt the therapy plan in case of observed range errors. However, there are researches ongoing that aim at exploiting different physiological changes that arise earlier using other MRI techniques [26].

  Nevertheless, the main advantages of this technique are its theoretical high spatial resolution, the lack of additional dose to the patient and the already widespread use of MRI scanners.

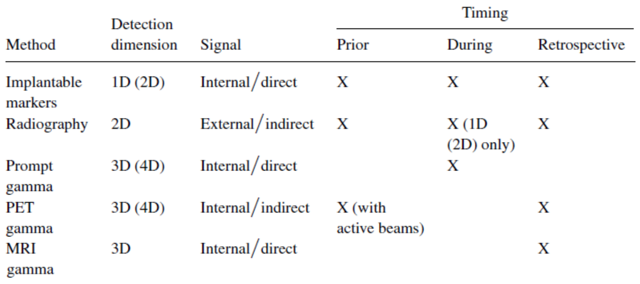

Method	Detection dimension	Signal	Timing		
			Prior	During	Retrospective
Implantable markers	1D (2D)	Internal/direct	X	X	X
Radiography	2D	External/indirect	X	X (1D (2D) only)	X
Prompt gamma	3D (4D)	Internal/direct		X	
PET gamma	3D (4D)	Internal/indirect	X (with active beams)		X
MRI gamma	3D	Internal/direct			X

Figure 2.22: Overview of the discussed techniques for the in vivo range verification [24] (1/2).

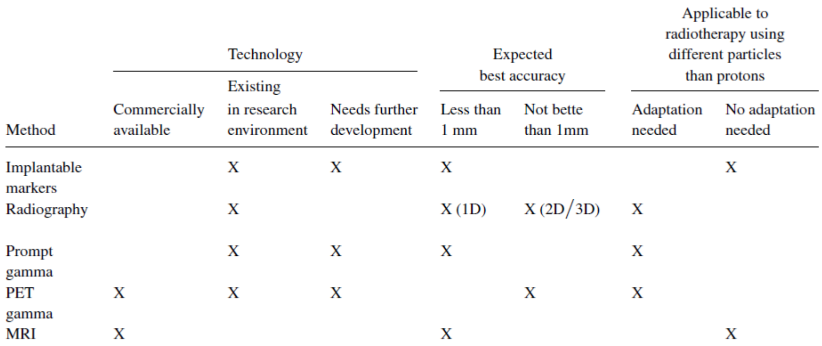

	Technology			Expected best accuracy		Applicable to radiotherapy using different particles than protons	
Method	Commercially available	Existing in research environment	Needs further development	Less than 1 mm	Not bette than 1mm	Adaptation needed	No adaptation needed
Implantable markers		X	X	X			X
Radiography		X		X (1D)	X (2D/3D)	X	
Prompt gamma		X	X	X		X	
PET gamma	X	X	X		X	X	
MRI	X			X			X

Figure 2.23: Overview of the discussed techniques for the in vivo range verification [24] (2/2).

To sum up, several researches are ongoing; all the proposed methods are complex and each one tries to exploit a different physical phenomenon to retrieve information about the dose distribution inside the patient's body. Range uncertainties are inevitable in particle therapy and, since its potential can be fully exploited only with a reliable in-vivo control of the dose distribution, it can be claimed that research related to this topic will go on until the goal is reached.

The AMPHORA project is investigating other techniques based on nano-sized superheated emulsions which, after having accumulated at the tumour site through functionalisation of the external shell, can be "activated" by the interaction with ionising radiations. The concepts studied by AMPHORA and their application to in vivo dosimetry will be further developed in Chapter 5.

Chapter 3

Radiation transport: mathematical formulation

This chapter aims at introducing the basic concepts, terminology and formalism of radiation transport theory. Indeed, that theory is the basis to understand how a radiation beam (and, in particular, a clinical beam) propagates into the matter. The understanding of all the physical phenomena involved, allows us to formulate the transport problem in mathematical terms. Once it is fully understood and translated, the next step will be to find a suitable method to solve it in all practical cases. Specifically, two main methods can be identified: analytical methods and stochastic methods. We will focus our attention on both, underlying pros and cons of each.

3.1 Definitions

In order to understand the following discussion, it is necessary to introduce some key concepts that will be recurrent.

- **Phase Coordinates**

  The phase coordinate of a particle is its position and momentum: $(\mathbf{r}, \mathbf{p})$. So, to fully describe it, we need a six-dimensional variable to represent a point in the phase-space. However, from now on, we will use two variables instead of the momentum; the particle energy E and a unit vector $\mathbf{\Omega}$, that defines the direction of the particle travel. Of course, since $\mathbf{\Omega}$ is a unit vector, the dimensionality of the problem remains six.

The phase coordinate will be: $(\mathbf{r}, \mathbf{\Omega}, E)$ and it will be often indicated by just $\mathbf{x}$.

- **Source Function**

  It is a function that fully describes the radiation source; each emitted particle will have a certain phase space coordinate depending on $S(\mathbf{x})$. If it is normalised per particle, $S(\mathbf{x})$ represent the probability distribution function (pdf) of $\mathbf{x}$.

- **Total Cross Section**

  A classical model of interaction can be used to understand this concept. Let's think about an atom as a sphere. We can assume that a particle interacts with the atom if it "enters the sphere". Under this view, it is straightforward that the probability of such an interaction will be proportional to the cross-sectional area of the sphere. In this way, we can easily define the *microscopic cross section*, with units of cm^2. However, for our purpose, it is better to work with the so called *macroscopic cross section*, which will be indicated with Σ, that is obtained by multiplying the microscopic one by the atomic density of the media $N(atoms/cm^3)$.

  $$\Sigma = \sigma N \tag{3.1}$$

  Σ represents the probability of an interaction per unit path length. Its unit is cm^{-1}. We talk about *total cross section* when we are condensing in Σ contributions from any possible interaction (and, in this case, the most appropriate symbol is Σ_{tot}). Instead, when we are focusing on a particular interaction we refer to it as the *partial cross section.* The total cross section is the sum of all partial cross sections.

  Thanks to that quantity, it is possible to derive the probability that a particle travels a distance l in a homogeneous material ($\Sigma = cost$ along the track) without interactions:

  $$P(l) = exp(-\Sigma l) \tag{3.2}$$

  Finally, exploiting the idea of the macroscopic cross section, it is possible to derive an expression for the mean free path for tracks in homogeneous materials:

  $$\langle l \rangle = \int_0^\infty l f(l) dl = 1/\Sigma \tag{3.3}$$

Where $f(l)$ is the probability density function of the free path:

$$f(l) = \frac{d}{dl}F(l) = \frac{d}{dl}[1 - P(l)] = \Sigma exp(-\Sigma l) \tag{3.4}$$

In the last equation, $F(l)$ is the cumulative distribution function (CDF) of $f(l)$ and represents the probability to have an interaction in a distance l.

- **Differential Cross Sections**

  The differential cross sections define the probability of an interaction with a given outcome. We can take as an example the probability that a particle with momentum described by $(\mathbf{\Omega}, E)$ undergoes an interaction as it travels a distance dl. If we want to know what the probability is of a specific outcome (for instance, the final state is described by a pair $(\mathbf{\Omega}', E')$) we should refer to the doubly differential cross section $\Sigma_s(\mathbf{r}, \mathbf{\Omega} \to \mathbf{\Omega}', E \to E')$.

  The total cross section is the integral of the differential cross section:

  $$\Sigma_s(\mathbf{r}, \mathbf{\Omega}, E) = \int d\mathbf{\Omega}' \int dE' \Sigma_s(\mathbf{r}, \mathbf{\Omega} \to \mathbf{\Omega}', E \to E'). \tag{3.5}$$

  Finally, if the material properties are isotropic, the interaction probability does not depend on the direction of particle travel before the interaction:

  $$\Sigma_s(\mathbf{r}, \mathbf{\Omega}, E) = \Sigma_s(\mathbf{r}, E) \tag{3.6}$$

- **Fluence**

  In Nuclear Reactor Physics the vectorial fluence $(\Phi(\mathbf{r}, \mathbf{\Omega}, E)$ is defined as *the average number of particles with energy E crossing a unit area of a surface located at point* $\mathbf{r}$ *and oriented normally to* $\mathbf{\Omega}$ [27]. So, it is important to emphasize that fluence reflects the *average* properties of a given radiation field. Integrating over all the possible directions Ω we easily obtain the *fluence spectrum* $\Phi(\mathbf{r}, E)$. Finally, integrating over all the possible energies we obtain the *total fluence* $\Phi(\mathbf{r})$.

  To get the average number of particles with a given energy E crossing a surface A orientated along a direction $\mathbf{n}$, an integral over the surface A of the product between $\Phi(\mathbf{r}, \mathbf{\Omega}, E)$ and the cosine of the angle between $\mathbf{\Omega}$ and $\mathbf{n}$ must be computed.

- **Collision Density**

  It is denoted by F and it represents the average number of collisions in the phase space volume $d\mathbf{x}$:

  $$F(\mathbf{x})d\mathbf{x} = \Sigma(\mathbf{r}, E)\Phi(\mathbf{x})d\mathbf{x}. \tag{3.7}$$

  The term $\Sigma(\mathbf{r}, E)\Phi(\mathbf{x})$ represents the average number of collisions.

- **Detector Response Function**

  In our case the word ”Detector” does not always refer to an actual physical device. It is just an useful mathematical concept used to relate a certain quantity of interest J to the fluence $\Phi(\mathbf{x})$. In fact, generally speaking, such quantities will be linear functionals of $\Phi(\mathbf{x})$ [27].

  $$J = \int \Phi(\mathbf{x})R(\mathbf{x})dx \tag{3.8}$$

  In this equation, $R(\mathbf{x})$ is the contribution to the quantity J from a unit path length of a particle with phase coordinate $\mathbf{x}$. The quantity J is often called the *detector reading in field* $\Phi(\mathbf{x})$.

  In the Geant4 Monte Carlo code that has been developed in this work, a relationship like this has been established to estimate the number of vaporised nanodroplets inside the phantom scoring the fluence in parallel layers. In our case J represents the estimated number of vaporization events, $R(\mathbf{x})$ represents the probability that a radiation with a given energy will vaporise a droplet and $\Phi(\mathbf{x})$ represents the amount of radiations that are normally hitting a given layer with a given energy.

3.2 The Boltzmann equation

In order to derive the full radiation transport equation, we can proceed step by step always including some additional physical phenomena that are involved. The first step is to retrieve a three-dimensional balance equation that expresses the conservation of the number of particles in a given control volume. The main assumption is that we consider a steady flow of particles that can leave or enter our control volume only through its surface; all the possible interactions between particles and matter are initially neglected. The balance will have the form:

$$\begin{gathered}\text{[number of particles entering }\Delta\text{V]}\\ +\text{ [particles produced by a source within }\Delta\text{V]}\\ =\text{ [number of particles leaving }\Delta\text{V].}\end{gathered}$$

To account for the particles entering or leaving the volume, we need to integrate over its surface $\Gamma(\Delta V)$, paying attention to the sign of the scalar product between $\mathbf{n}$, which is an outward-pointing unit vector normal to the surface Γ, and Ω.

$$\begin{aligned} &-\oint_{\Gamma:(\boldsymbol{\Omega}\cdot\mathbf{n})<0} \Phi(\mathbf{r},\boldsymbol{\Omega},E)(\boldsymbol{\Omega}\cdot\mathbf{n})dA + \int_{\Delta V} S(\mathbf{r},\boldsymbol{\Omega},E)dV \\ &= \oint_{\Gamma:(\boldsymbol{\Omega}\cdot\mathbf{n})>0} \Phi(\mathbf{r},\boldsymbol{\Omega},E)(\boldsymbol{\Omega}\cdot\mathbf{n})dA \end{aligned} \tag{3.9}$$

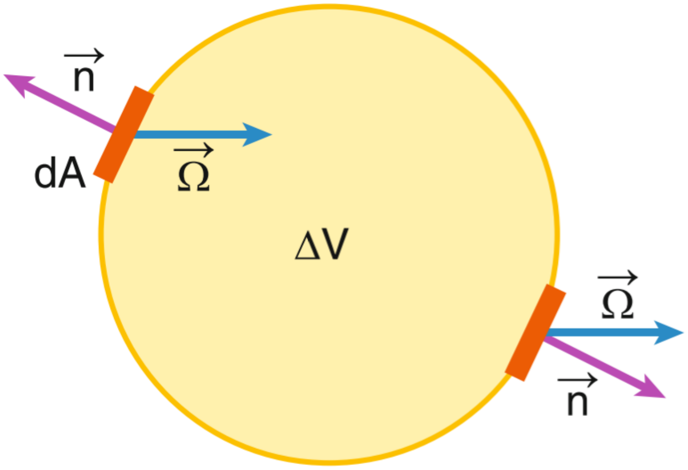

Figure 3.1: Three-dimensional balance equation for a free flow of particles [27]

Combining the two surface integrals and using the divergence theorem, we get:

$$\begin{aligned} &-\oint_{\Gamma} \Phi(\mathbf{r},\boldsymbol{\Omega},E)(\boldsymbol{\Omega}\cdot\mathbf{n})dA = \int_{\Delta V} div[\boldsymbol{\Omega}\Phi(\mathbf{r},\boldsymbol{\Omega},E)]dV \\ &= \int_{\Delta V} (\boldsymbol{\Omega}\cdot\nabla)\Phi(\mathbf{r},\boldsymbol{\Omega},E)dV \end{aligned} \tag{3.10}$$

Finally, substituting this expression in the 3.9, dividing both sides by ΔV and taking the limit $\Delta V \to 0$:

$$(\mathbf{\Omega} \cdot \nabla)\Phi(\mathbf{r}, \mathbf{\Omega}, E) = S(\mathbf{r}, \mathbf{\Omega}, E) \tag{3.11}$$

The first term of the equation accounts for particle travel; for this reason it is named *streaming operator.* This equation is called the *balance equation for a free flow of particles.* The equation is very similar to the continuity equation in fluid mechanics. The only difference is that the latter expresses mass conservation in terms of the fluid velocity and mass density while the transport equation for radiation expresses conservation of number of particles in terms of fluence.

In the next step we will also consider the potential change of energy and direction due to interactions with matter inside our control volume; this will lead to a more general form of the balance equation.

3.2.1 The Boltzmann equation for non-multiplying systems

In order to get a first simple form of the Boltzmann equation, we need to apply the same balance as before. However, now we will count only particles with a given momentum **p**. This implies that we need to consider two more processes in our model: loss and gain of particles with momentum **p** due to scattering within the control volume ΔV. However, we will still neglect all the interactions that can lead to particles production (non-multiplying system):

[number of particles with momentum **p** entering ΔV through its boundaries]
+ [particles with momentum **p** produced by a source within ΔV]
+ [particles with momentum **p** produced within ΔV by scattering]
= [number of particles with momentum **p** leaving ΔV through its boundaries]
+ [number of particles with momentum **p** lost due to scattering within ΔV].

Actually, in case of interaction, it is possible to have also absorption; this will also lead to a particle loss from the balance point of view. For this reason, to compute the collision density for the newly introduced production term we will use the *scattering cross section* while for the removal term we will use the *total cross section*, which includes also the absorption processes:

- Removal term → $\int_{\Delta V} \Sigma(\mathbf{r}, E)\Phi(\mathbf{r}, \mathbf{\Omega}, E)dV$
- Production term → $\int_{\Delta V} \int dE' \int d\Omega' \Sigma_s(\mathbf{r}, \mathbf{\Omega}', E' \to \mathbf{\Omega}, E)\Phi(\mathbf{r}, \mathbf{\Omega}', E')dV$.

Finally, as before we divide both sides of the equation by ΔV and we take the limit $\Delta V \to 0$.

$$\begin{aligned}&(\mathbf{\Omega} \cdot \nabla)\Phi(\mathbf{r}, \mathbf{\Omega}, E) + \Sigma(\mathbf{r}, E)\Phi(\mathbf{r}, \mathbf{\Omega}, E)\\ &= S(\mathbf{r}, \mathbf{\Omega}, E) + \int dE' \int d\Omega' \Sigma_s(\mathbf{r}, \mathbf{\Omega}', E' \to \mathbf{\Omega}, E)\Phi(\mathbf{r}, \mathbf{\Omega}', E').\end{aligned} \tag{3.12}$$

Now we have also a *removal operator*, that is represented by the second term and a *collision integral*, that is represented by the last term (often called *the scattering source*).

This is a simple form of the Boltzmann equation; the main feature is that it is **linear**. This property is valid if the two major assumptions that we implicitly made can be considered true:

1. Particles do not interact with each other
2. Material properties, such as cross sections, do not change when fluence changes

The main goal, in general, will be to compute a specified detector reading J for a given source $S(\mathbf{x})$ and detector $D(\mathbf{x})$. In order to get the solution, we should identify a finite volume V that encompasses both the source and the detector. That will be the *computational domain* and it should be minimized for faster calculations. However, since that volume is finite,we need to put boundary conditions on its surface, bearing in mind that each particle that is outside that volume can't be tracked. Consequently, the most common boundary condition when dealing with convex surfaces imposes that the fluence incident on the boundary from the outside is zero. This means that there are no sources outside and that particles that have left V can't scatter back (they are lost from a computational point of view). As a consequence, this boundary condition requires that the computational domain is not too close to detectors and sources, otherwise there will be an underestimation of the detector reading due to particles that are considered lost but that could actually have re-entered the volume through scattering [27].

3.2.2 The Boltzmann equation for multiplying systems

To get a more comprehensive description of the radiation transport phenomena, it is possible to include other physical interactions in the model. This will lead to enhanced forms of the Boltzmann equation.

If we consider a multiplying system, we should include also all the interactions that will lead to particle multiplication; they are characterised by both a momentum change and a secondary particle production. For instance, in case of electron transport an example of scattering interaction is the excitation, while an example of multiplying interaction is the ionization. For the latter, the cross section could be defined as $\Sigma_2(\mathbf{p'} \rightarrow \mathbf{p_1}, \mathbf{p_2})$ where $\mathbf{p_1}$ and $\mathbf{p_2}$ are the momenta of the two particles emerging from the collision.

To include these interactions in the Boltzmann equation we need an additional collision integral that accounts for them:

$$\begin{aligned}
&(\mathbf{\Omega} \cdot \nabla)\Phi(\mathbf{r}, \mathbf{\Omega}, E) + \Sigma(\mathbf{r}, E)\Phi(\mathbf{r}, \mathbf{\Omega}, E) \\
&= S(\mathbf{r}, \mathbf{\Omega}, E) + \int dE' \int d\Omega' \Sigma_1(\mathbf{r}, \mathbf{\Omega}', E' \rightarrow \mathbf{\Omega}, E)\Phi(\mathbf{r}, \mathbf{\Omega}', E') \\
&+ \int dE' \int d\Omega' \Phi(\mathbf{r}, \mathbf{\Omega}', E') \int dE'' \int d\Omega'' [\Sigma_2(\mathbf{r}, \mathbf{\Omega}', E' \rightarrow \mathbf{r}, \mathbf{\Omega}, E; \mathbf{r}, \mathbf{\Omega}'', E'') \\
&+ \Sigma_2(\mathbf{r}, \mathbf{\Omega}', E' \rightarrow \mathbf{r}, \mathbf{\Omega}'', E''; \mathbf{r}, \mathbf{\Omega}, E)]
\end{aligned} \tag{3.13}$$

In the new collision integral the first term in the square brackets accounts for multiplying collisions that result in the first of the two particles emerging with momentum $\mathbf{p}$, while the second term account for the reverse situation. The first integral accounts for all the particles with momentum $\mathbf{p}'$ that could undergo such kind of interaction.

3.2.3 Simplified forms of the Boltzmann equation

Even if the complete form of the Boltzmann equation is complex, in certain conditions simplifications are possible. We will discuss some useful examples.

- **Energy Degradation Equation**

  There are several problems in which this simplification can be applied. The main assumptions are:

  1. Infinite homogeneous medium;

2. Infinite spatially uniform source.

These assumptions allow a huge simplification: all cross sections, the source function and the fluence can be considered independent of (x,y,z). Consequently, the streaming operator is zero and the Boltzmann equation 3.12 becomes:

$$\Sigma(E)\Phi(\mathbf{\Omega},E) = S(\mathbf{\Omega},E) + \int dE' \int d\Omega' \Sigma_s(\mathbf{\Omega}',E' \to \mathbf{\Omega},E)\Phi(\mathbf{\Omega}',E') \tag{3.14}$$

Integrating both sides over Ω we get the *energy degradation equation*:

$$\Sigma(E)\Phi(E) = S(E) + \int dE' \Sigma_s(E' \to E)\Phi(E') \tag{3.15}$$

If electron equilibrium is achieved in a given volume, the assumptions are valid and it is possible to model the electron transport using the energy degradation equation.

In general, such equilibrium is achieved when electrons are produced by photon interactions in a volume larger that the electron range. Consequently, from the electron transport point of view, that volume can be considered infinite. In addition, it is possible to consider the photon fluence constant throughout it if the volume is small compared to the attenuation scale length of the photon beam. This would make it possible to consider the source of electrons constant.

If such a volume can be identified, inside it electron equilibrium is achieved and the energy degradation equation can be applied to get the fluence $\Phi(E)$ that, in this case, is called *electron energy degradation spectrum* or simply *equilibrium spectrum.* [27]

- **Continuous Slowing Down Approximation (CSDA)** When we have to deal with *charged particle transport*, we know in advance that there will be a very large number of inelastic collisions per unit path length. However, for each event the energy loss will be on the order of $10eV$ [27]. Comparing that value with the typical initial kinetic energy of an electron in a radiation field (for instance, external beam radiotherapy), we found that it is many orders of magnitude lower. So, for such an electron, it would be possible to approximate the discrete energy loss process in a continuous manner. Every time this condition is fulfilled, we talk about the *continuous slowing down approximation* (CSDA).

Even if it is not related to equilibrium conditions, since it concerns only energy loss it is possible to derive such approximation starting from the energy degradation equation. In fact, it is sufficient to rewrite the scattering cross section inside the collision integral using different variables:

$$\Sigma_s(E' \to E) = \Sigma_s(E + \Delta E, \Delta E) \tag{3.16}$$

Now, $\Delta E = E' - E$ represents the energy lost in one collision and, since the likelihood of collisions with an high energy loss is low, the function $\Sigma(E', \Delta E)$ decreases rapidly as the ΔE increases. In addition, since in the CSDA $\Delta E << E$, variations of ΔE have a negligible effect on E' and do not cause Σ_s to change significantly [27]. This applies also to $\Phi(E')$ and so we can apply a Taylor series expansion:

$$\Sigma(E', \Delta E)\Phi(E') \approx \Sigma(E, \Delta E)\Phi(E) + \frac{\partial}{\partial E}[\Sigma(E, \Delta E)\Phi(E)]\Delta E \tag{3.17}$$

Substituting the right-hand side in the collision integral we find:

$$\int_E^\infty dE'\Sigma_s(E' \to E)\Phi(E') \approx \Sigma_s(E)\Phi(E) + \frac{\partial}{\partial E}[\beta(E)\Phi(E)] \tag{3.18}$$

In this last equation we should highlight a new factor, $\beta(E)$ that is the so called *stopping power*.

$$\beta(E) = \int_0^\infty \Sigma_s(E, \Delta E)(\Delta E)d(\Delta E) = -\frac{dE}{dx} \tag{3.19}$$

It is worth to underline that the concept of stopping power can be applied only to charged particles and it represents the *average* energy lost per unit path length.

However, should be considered that, with some probability, a large energy loss in a collision is possible even if the kinetic energy of the charged particle is sufficiently high. For this reason, a more rigorous method for applying the CSDA foresees the subdivision of collisions in *soft collisions* and *hard collisions* (or *catastrophic collisions*). In order to do that, an energy loss threshold ΔE_t has to be defined in advance to obtain:

  - Soft collisions → $\Delta E < \Delta E_t$: CSDA is applicable
  - Hard collisions → $\Delta E >= \Delta E_t$: CSDA not applicable

At the end, the collision integral will be subdivided into two integrals and the CSDA approximation will be applied just to the one related to soft collisions. Thanks to this method it is possible to define a *restricted stopping power* $\beta_<(E)$ that considers only interactions with a maximum energy loss of ΔE_t.

$$\beta_<(E) = \int_0^{\Delta E_t} \Sigma_s(E, \Delta E)(\Delta E)d(\Delta E) \tag{3.20}$$

This approximation is often implemented in Monte Carlo algorithms for charged particle transport that are called *condensed history algorithms*. In particular, they simulate only hard collisions explicitly, while when a charged particle travels between two consecutive hard collisions it is assumed that it continuously loses energy at a well defined rate given by $\beta_<(E)$. As we will see in more detail, thanks to this approach it is possible to simulate the transport of charged particles considerably reducing the computational effort that is required.

- **Fokker-Planck Approximation** The Fokker-Planck approximation is based on the assumption that scattering angles are small. It is often used in both Monte Carlo and deterministic Boltzmann solvers. It is worth to mention because it is very useful in proton therapy applications. In such applications proton energy ranges from 70 to 250 MeV; so, it is sufficiently high to assume that the majority of the interactions will have a small scattering angle, leading to a forward-peaked distribution.

  The derivation of this approximation, even if it is not straightforward, is conceptually similar to the CSDA; it is also based on a Taylor series expansion of the collision integral, but in this case it is made in terms of angular variables. For the sake of completeness, the resulting collision integral in the Fokker-Planck approximation is just reported. For a deeper insight on its derivation, the reader is referred to the bibliography [27].

$$\int d\Omega' \Sigma_s(\mathbf{r}, \mathbf{\Omega}' \cdot \mathbf{\Omega}) \Phi(\mathbf{r}, \mathbf{\Omega}')$$
$$\approx \Sigma_s(\mathbf{r}) \Phi(\mathbf{r}, \mu, \phi) + \frac{1}{4} \Sigma_s(\mathbf{r}) \langle \theta_0^2 \rangle [\frac{\partial}{\partial \mu}(1-\mu^2) \frac{\partial}{\partial \mu} + \frac{1}{1-\mu^2} \frac{\partial^2}{\partial \phi^2}] \Phi(\mathbf{r}, \mu, \phi) \tag{3.21}$$

In this expression, $(\theta\ , \phi)$ are respectively the poloidal and azimuthal angles in spherical coordinates, $\mu = \cos\theta$ and $\langle \theta_0^2 \rangle$ is the mean square scattering angle.

After this brief digression on the main physical models for the radiation transport problem, we need some methods to actually solve them in geometries that are complex and heterogeneous. As an example, typical computational domains in the medical physics field are human bodies; they are well known for being heterogeneous and not static with respect to the external radiation source. Moreover, in medical physics accuracy is of main concern. For that reason, we will see that Monte Carlo simulations, although computationally expensive, often are a compulsory choice for these applications, especially for those that involve the use of heavy ions. Instead, the use of analytical approximated models is better in static large scale problems with well known geometry and materials where a high accuracy is not required [27].

3.3 Stopping Power: a more detailed insight

Even if at first the stopping power was defined only for α and β particles, now it has been extended to every kind of charged particles and it is of main concern in radiation transport. It depends on the material properties and on the type and energy of radiation.

It is possible to identify two different quantities that contribute to it:

- **Collision Stopping Power $\mathbf{S_{col}}$**

  This contribution comes from interactions between orbital electrons and the projectile and from inelastic nuclear interactions between the projectile and target nuclei. The effect on the charged particle will be different in case of light particles or heavy particles. In fact, in case of electrons, the Coulomb interactions with the orbital electrons are of primary importance while, in case of heavy charged particles the elastic Coulomb interactions with proximal nuclei become more relevant. Moreover, inelastic nuclear interactions are possible only for heavy charged particles; in this case, the effect is huge because lot of secondary particles could be emitted (often followed by a γ photon).

In general, the collision stopping power is directly proportional to the ratio between the target charge and mass number $\frac{Z}{A}$. In addition, it is worth to underline that, only for light charged particles there is a dependence of the collision stopping power from the so called *density effects*. In fact, if we consider an electron travelling in a high density media, the electric charge seen by atoms distant from the electron is reduced due to the polarization of intermediate atoms. So, for instance, when it is necessary to estimate the dose of a given electron flux in an human tissue using a dosimeter in air, it is necessary to apply corrective factors that take into account also this effect; the ratio between the mass stopping powers $(\frac{S}{\rho})_{water}/(\frac{S}{\rho})_{air}$ is strongly dependent on energy above 0.5 MeV [28] .

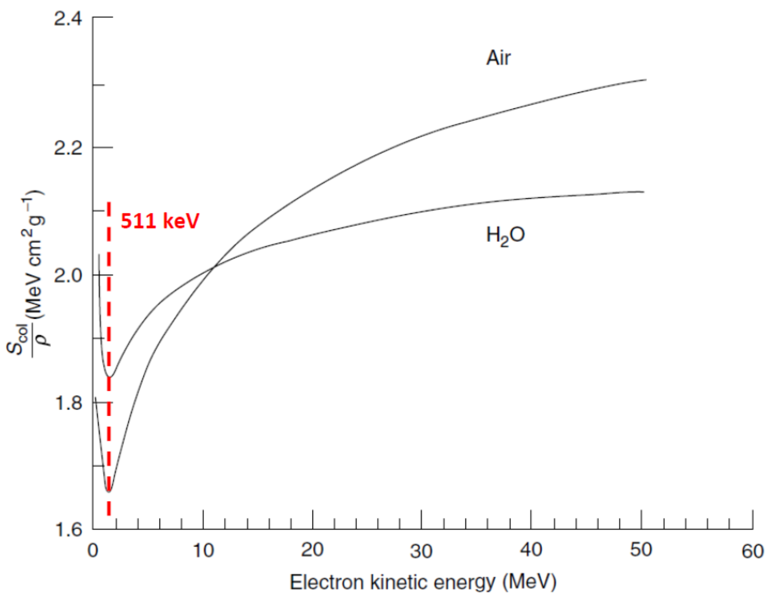

Figure 3.2: Variation of mass collision stopping power with electron E_k in air and water [28]

Another important parameter that affects the collision stopping power is the *mean excitation energy*. It is only a property of the medium and it describes how easily a target can absorb kinetic energy from the projectile. It is worth to mention it because it is a main concern in radiation therapy plans due to its uncertainties.

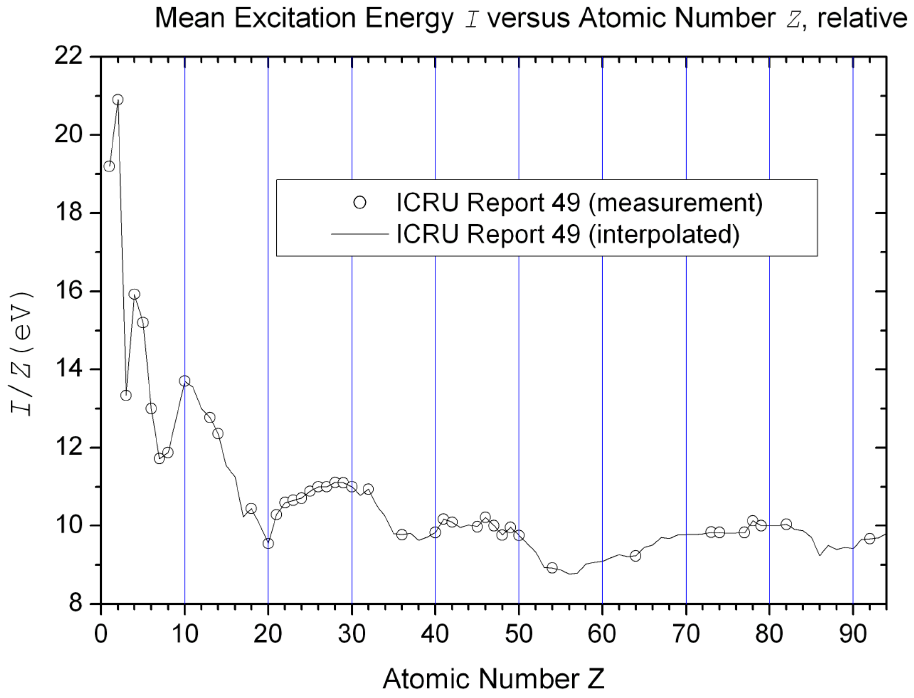

Figure 3.3: Dependence of mean excitation energy with atomic number [28]

- **Radiation Stopping Power S_{rad}**

  Accelerations of the charged projectile in the electric field of the absorber nuclei result in the emission of X-rays (the so called Bremsstrahlung effect). The contribution of this effect to the overall stopping power is defined as the radiation stopping power. The energy loss in this process becomes important for light particles (of mass m in media with a high atomic number Z. In fact, the intensity of the produced photon is proportional to $\frac{Z}{m}^2$. Moreover, the angular distribution of emitted photons becomes more forward peaked as the energy of the projectile increases. In general, for electrons below 10 MeV in low-Z materials this effect is negligible, while it is completely negligible for heavy charged particles in almost any case[28].

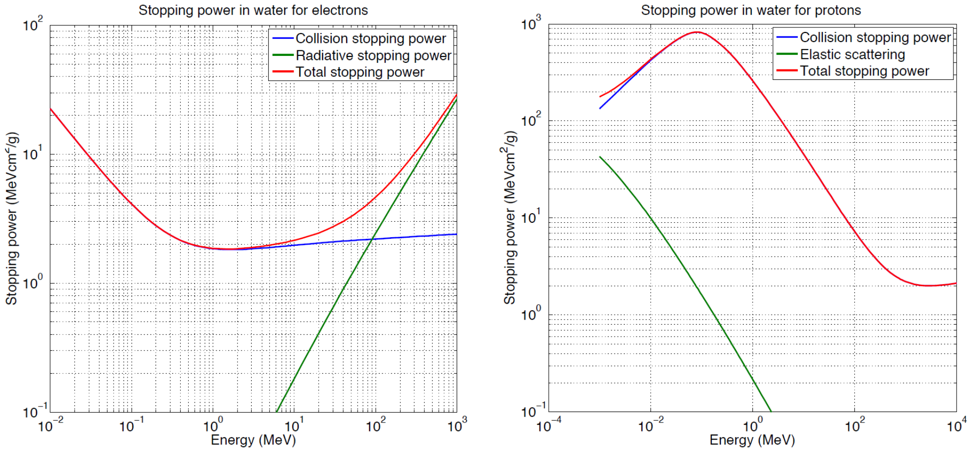

Figure 3.4: Radiation and Collision Mass Stopping Powers in water [28]

To conclude, it is important to bear in mind that stopping powers govern only the **average rate of energy loss**. Moreover, they describe only the energy lost by the charged particle, not the energy actually deposited in the medium.

Chapter 4

The Monte Carlo simulation of radiation transport

The first reference to the Monte Carlo method is dated back to 1777, before the birth of calculators. That year, the Comte de Buffon proposed a formula to compute the probability of tossing a needle onto a ruled sheet; with a needle of length L and a plane ruled with infinite parallel lines with interspace $d > L$, the probability that a needle randomly tossed on the surface intersects a parallel line is:

$$p = \frac{2L}{\pi d} \tag{4.1}$$

The interesting fact is that through a statistical experimental method it is actually possible to estimate π exploiting that idea [27] .

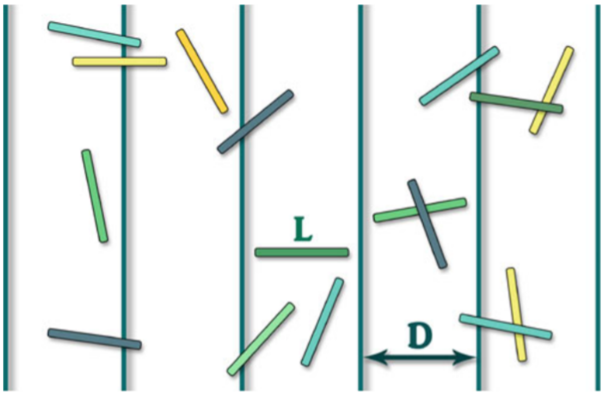

Figure 4.1: Random needle toss experiment [27]

However, the earliest description of that method in English was only given in 1873 by Hall. To make it simple, throwing a needle N times on such a surface permit us to estimate the probability of intersection in one trial as:

$$p(experimental) = \frac{N(intersect)}{N(total)} \tag{4.2}$$

Then, using this estimated probability in the formula 4.1 we can easily get an estimate of π:

$$\pi \approx \Theta_\pi = \frac{2L}{p(experimental)D} \tag{4.3}$$

This simple example contains all the elements of a Monte Carlo methods scheme. In this particular case, the quantity of interest (π) is expressed as a function of p and the observed $N(intersect)$ has a binomial distribution, which parameter has been estimated through an experimental sampling. So, at the end, we get only an *estimator* of π, which accuracy will depend on the amount of trials which have been executed (and, for a given number of trials, it will depend on the geometrical setup of the experiment).

The current name of the method was suggested by Metropolis only in the late 1940th. In particular, it was referring to a statistical approach used to solve neutron transport problems that was being developed in that period at the Los Alamos Laboratory [29]. Nevertheless, it seems that it was not the first known application of the method to radiation transport; according to Sergè [30] and Anderson [31], E. Fermi actually "invented" the method and used it to study moderation of neutrons already in 1934, but he has not published anything on the technique he used.

The uniqueness of this method is in its inherent statistical nature. But, in contrast to classical statistics where samples are collected from observations, in Monte Carlo simulations they are generated by a proper computer algorithm. Therefore, the core of this method is based on the sampling mechanism that retrieves data from statistical distributions that are representative of the problem under examination. In contrast to statistical inference, at the end we will obtain one or more estimators of a parameter distribution. This will produce an inherent **statistical uncertainty** in the solution that will sum up with any systematic error that could be introduced by the algorithm itself. For this reason it is important to provide at least the standard deviation of the estimate, which in general will decrease simply by increasing the sample size, but this will lead to an increase in the computational cost that is not always affordable. However, thanks to its solid mathematical basis, if calculations are set up correctly large errors are unlikely [27].

A general schema of a Monte Carlo method aimed at solving a physical problem is the following [27]:

1. Translation of the physical problem in mathematical terms; if one knows the governing physical laws accurately and, using enough computing resources, it is possible to answer any well-posed physical question. This is the case for most applications in radiotherapy since they are well described in the Quantum Electrodynamics (QED) theory; [12]
2. Formulation of a statistical interpretation of the problem; the quantities of interest must be expressed as a parameter of a distribution (e.g the mean);
3. Development of a proper sampling algorithm;
4. Derivation of the estimators together with their statistical uncertainty;
5. Optimisation of algorithms and choice of estimators to reduce the computational effort. Often variance reduction methods are used to achieve this goal without introducing additional systematic errors;
6. Generation of a sample large enough to achieve a desired level of accuracy of the estimator. At the end, the parameter and its uncertainty are estimated through the sample itself.

Since radiation transport is an inherently random process, it represents a perfect example to exploit the major features of the Monte Carlo method. In fact, for random phenomena, the statistical interpretation that is required could be trivial. This will allow us to adopt an approach that is called *analogous simulation* and is well-known for its simplicity. It is based on the direct simulation of the phenomena “step by step” without the implementation of a more sophisticated mathematical formulation. This will result in a lack of flexibility to optimise the algorithm, but at the end it allows for a clear physical interpretation of each step of the algorithm [27].

The use of the Monte Carlo method for solving applied problems in the medical physics field has increased a lot over the past three decades; the widespread availability of powerful computers has met the increasing need of accurate estimation of physical quantities like the absorbed dose in radiation therapy, medical imaging and nuclear medicine. Moreover, the rapid progress in hadron therapy has made the accurate understanding of biological effects of radiation extremely important. [27].

Finally, this huge progress made in solving the problems in the field of medical physics using Monte Carlo methods is also a result of the development of "user-friendly" software like *Geant4*, that has been widely used in the present work and that will be fully described later on.

4.1 Deterministic methods vs Monte Carlo

As presented in the previous chapter, the radiation transport problem is well described by Boltzmann's transport equation. To get an estimate of important quantities like the dose deposition, it is necessary to solve it and this can be done by using deterministic or stochastic methods. Which is the most suitable method? The answer is: it depends. In fact, both methods have advantages and disadvantages and the correct choice can be made examining carefully the problem statement.

The main features of the system that have to be taken into account are:

- Space dimensionality of the system;
- Physics involved;
- Time dependence;
- Memory dependence of the processes;
- Homogeneity or heterogeneity of the medium.

Deterministic models are often preferred in systems with low dimensionality and simple geometries that are well described by deterministic laws. For instance, in a domain like the human body (that is dynamic due to the patient mobility) a totally deterministic model can be too restrictive.

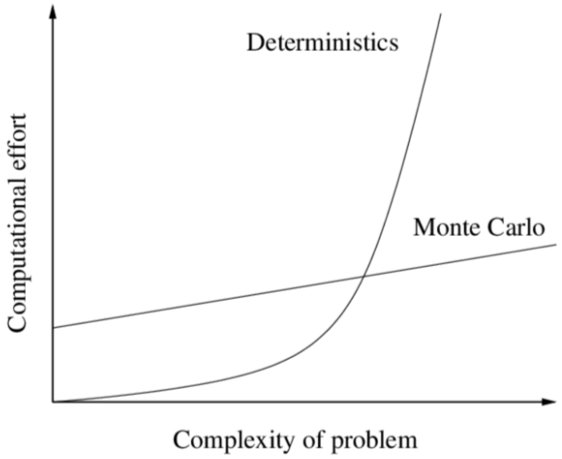

Figure 4.2: Qualitative comparison between deterministic and stochastic methods [33]

In case of radiation transport, the deterministic approach explicitly solves the problem in the entire phase-space. In order to do that, it uses finite-differencing techniques; the spatial domain is subdivided in meshes, the angular domain into discrete directions and the energy into groups. The output of such a model is limited to the particle flux in the entire domain; only a post-process of this “raw” information will provide more insight on the process.

An advantage of the deterministic approach is its superior speed of computation, which could be many order of magnitude greater than the one in Monte Carlo simulations. Moreover, no statistical uncertainties will be present and the accuracy of the solution will depend primarily on the discretisation; in fact, such an approach will solve the problem only on discretised points, giving in output the mean particle flux in each region (per energy group and per angular direction). It is possible to increase the accuracy by increasing the number of discrete points, but this will increase the time of computation and may lead the ‘numerical build up” phenomena. As a result, both too few discrete points or too much discrete point can result in non-physical results that are called “artefacts”. For this reason it is necessary to find a trade-off that will depend on the particular application [32].

The Monte Carlo approach (that has a stochastic nature) is based on the simulation of the whole particle trajectory through sampling from the probability distribution of each possible particle interaction at each step.

In case secondary particles have been generated, they are tracked in the same way until their kinetic energy goes below a predefined cut-off value or until an absorption phenomena occurs. The simulation of an entire primary particle trajectory is called *a history*.

Then, the next part of a Monte Carlo simulation concerns the collection of the information from the simulated tracks to estimate quantities of interest (for instance an observable J). This procedure is called "tallying" and the estimators are called "tallies". To do so, many histories are run and their response contributions are scored at discrete tally volumes or surfaces [32].

Finally, the mean response together with its statistical uncertainty are computed from the Central Limit Theorem. In fact, if the true average $\bar{x}$ exists and the distribution in x has a true finite variance indicated by σ_x^2, the Central Limit Theorem guarantees that the Monte Carlo estimator for $\bar{x}$ can be made arbitrarily close to $\bar{x}$ by increasing the number of histories simulated. Moreover, the theorem state that the distribution of the estimator is Gaussian and is characterised by a variance that can be estimated through the simulation itself, as we will see later on [12].

To sum up, the Monte Carlo method has a significant advantage; it can accurately follow each particle through complex geometries. In addition, unlike the deterministic approach, the response tally is not limited to the particle flux. However, it has a main limitation due to statistical uncertainties, especially in regions with limited particle histories [32].

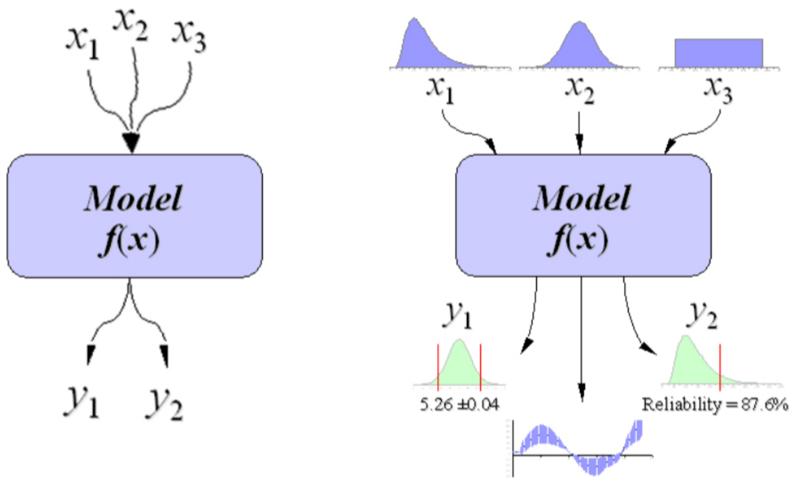

Figure 4.3: Deterministic (left) and stochastic (right) models [33]

A typical complex application in which it is better to adopt a Monte Carlo method is the treatment planning for radiotherapy. It requires the calculation of a 3D dose distribution in a heterogeneous (soft tissues, lung, bone, air cavities...) and dynamic geometry (the patients cannot be completely immobilized during treatment delivery) at a spatial resolution of approximately $2 - 3mm$ [27]. Nevertheless, the American Association of Physicists in Medicine (AAPM) [34] recommends that, regardless of the complexity of the problem, the uncertainty in the dose distribution should not exceed 2%. This can be achieved through the use of Monte Carlo simulations especially when dealing with proton therapy and hadron therapy, in which small uncertainties in range estimates lead to huge and dangerous uncertanties in dose distributions, making the treatment planning more challenging than before.

Finally it is worth to emphasize again that neither the deterministic nor the stochastic methods could be defined as "gold standards"; a careful choice of the best computational method for each particular task is necessary [32].

4.2 Sampling techniques

The core of the Monte Carlo method is represented by the sampling techniques that are employed. They represent the tool that allow to sample random values according to given probability distributions. For brevity here we will be describe only the main methods; for a deeper insight, the reader is referred to the bibliography [27].

- **Inversion method for continuous distributions** This method allows to generate a random number ξ that is described by a continuous probability distribution $f(x)$. Let's take into account its cumulative distribution function (CDF):

  $$F(x) = \int_{-\infty}^{x} f(x)dx \tag{4.4}$$

  After having generated a random number γ from a uniform distribution between 0 and 1 through an appropriate pseudo-random algorithm, the inverse function F^{-1} must be computed. Finally, solving the equation $\xi = F^{-1}(\gamma)$ it is possible to obtain ξ.

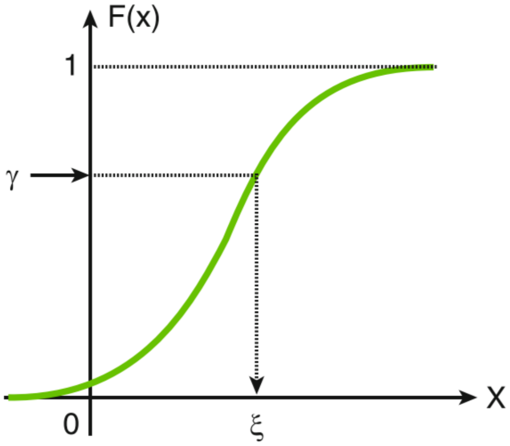

Figure 4.4: Inversion method for a continuous distribution [27]

This is the most straightforward and fast sampling method, but it requires that the cumulative distribution function $F(x)$ is invertible and that the inverse function is available in its analytical form.

- **Composition method**

  This method tries to overcome some of the limitations of the inversion method. In particular, it requires that $F(x)$ can be expressed as a sum of other CDFs $(F_1, F_2, F_3, \dots)$ each one associated with a proper weight $(p_1, p_2, p_3, \dots)$ and such that they cover all the possible outcomes:

$$\begin{aligned} &F(x) = p_1F_1(x) + p_2F_2(x) + p_3F_3(x) + \dots \\ &\sum_i p_i = 1 \end{aligned} \tag{4.5}$$

  In case the hypotheses are valid, this sampling algorithm can be applied:

  1. Generate γ from the uniform distribution in (0,1) such that $P(j = \gamma) = p_j$
  2. Retrieve ξ from the CDF $F_j(x)$.

  In radiation transport problems this method is used very often to select a particular interaction mode that occurs with probability p_j among all possible interactions.

- **Rejection method - Neumann's method**

  The CDF inversion method is not necessarily the fastest or the simplest. For instance the rejection method, depending on the properties of the distribution, could be more efficient and flexible. In order to apply it, we need to identify a probability distribution $g(x)$ that must satisfy the following properties:

  1. It needs to be similar to $f(x)$.
  2. Sampling from $g(x)$ should be simple.
  3. A number $C \geq 1$ such that $Cg(x) \geq f(x) \forall x$ exists. For a better efficiency, $g(x)$ with the lowest C should be chosen.

  At the end, the algorithm will be composed by three steps:

  1. Sample ξ from $g(x)$.
  2. Sample γ from a uniform distribution in $(0, 1)$.
  3. Rejection step: if $\gamma \leq \frac{f(\xi)}{[Cg(\xi)]}$, then accept ξ. Otherwise, go back to step 1.

  The efficiency of the algorithm is expressed in terms of the probability of accepting ξ. It can be proven that it is equal to $\frac{1}{C}$. [27]

4.3 Examples of transport of charged particles

There are several charged particles that play an important role in radiotherapy thanks to their characteristics; they include mainly electrons, positrons, protons and carbon ions. Moreover, there is a lot of ongoing research on other heavier ions as possible alternative to protons and carbon ions [27].

To simulate their tracks in Monte Carlo algorithms two main methods are adopted:

- **Condensed history algorithms**

  It is considered a "standard" and is a good compromise between computational speed and accuracy in most applications [27]. It classifies all the interactions in "hard" or "soft" depending on the energy ΔE lost in the interaction; for $\Delta E \geq E_t$ the interaction is classified as "hard", otherwise "soft". All the "hard" collisions are simulated explicitly, while the “soft” ones are simulated approximately by using a multiple scattering theory. Consequently, the efficiency of the algorithm is given by the choice of E_t.

The multiple scattering theory is based on the assumption that each interaction will cause both small deflection and small energy loss. If this assumption holds, it is possible to predict the distributions of the particle parameters due to several "soft" collisions condensing their effects all together after a given track length. In order to do that, approximated models that "condense" what happened during the underlying trajectory are implemented.

For instance, a CSDA model for the energy loss could be implemented . But, since radiation transport is an inherently random process, assuming that the energy loss is "deterministic" instead of being random is often a too strong hypothesis. So, in Monte Carlo codes that model is often extended to account also for energy straggling (Gaussian Model). Then, to predict the angular distribution a Fokker-Plank model or similar models could be used [27].

The step size is a key optimization parameter; it defines the balance between computing speed and accuracy and depends on the particle energy and material properties. Moreover, in a voxelised heterogeneous geometry it is possible to limit the uncertainties associated with boundary crossing by reducing the step size when a simulated particle approaches a boundary. Actually, to get better results the algorithm should be switched to the “event-by-event” one in these situations. [27]

To sum up, an overview of a typical condensed history algorithm is the following:

1. Start the charged particle track through either sampling the initial phase coordinates from the source distribution (if it is emitted by the source) or from differential cross sections (if it is produced in a collision).
2. Sample a free path to a “hard” collision considering all the possible interactions from the sampled initial phase coordinates
3. Compare the sampled free path to the defined step size

Now, two different things could happen:

- The free path is less than the step size:

    1. Move the particle to the point of the collision and sample its new parameters according to the multiple scattering theory
    2. Simulate the "hard" collision; if secondary particles are produced with energies exceeding (E_t), their trajectories need to be simulated. Otherwise they do not need to be tracked but the energy transferred to them must be accounted for.
  - The free path exceeds the step size: move the particle by a distance equal to the step size. Sample the particle parameters using multiple scattering theory. Make the next step, but keep in mind that the distance to the next "hard" collision has already been sampled.

  This algorithm iterates until no more particles needs to be tracked. This could be due to:

  1. The energy of the tracked particles goes below a predefined cut-off value;
  2. The particles have left the computational domain;
  3. The particles have been absorbed.

  As a result, the history terminates.

- **Event-by-event algorithms**

  It is the most accurate technique to simulate charged particle trajectories. All the interactions are simulated explicitly and, differently from the condensed history algorithms, particles travel along a straight line with constant energy between interactions. This is the same approach that is adopted for neutral particles; the only difference is that the latter have interaction cross sections of an order of magnitude smaller, which make it possible to use an event-by-event algorithm in all situations (few events in a single history). Using this approach with charged particles leads to the simulations of many interactions and the resulting algorithm will be very slow, often unpractical.

  In Fig. 4.5, tracks of three 10-MeV protons in water are showed. They are simulated using the Geant4-DNA software [35] [36]; it is especially dedicated to simulations in water and implements an event-by-event algorithm with a cut-off energy for electrons that can be as low as 10 eV.

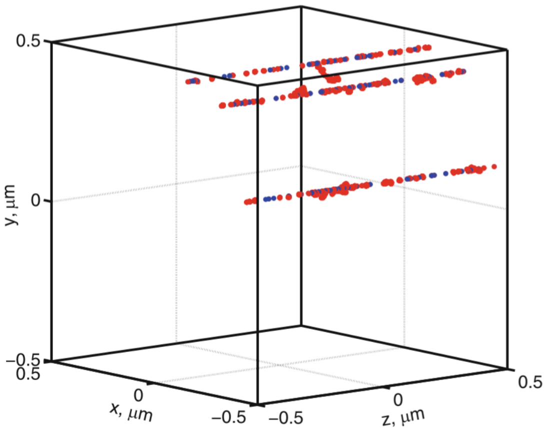

Figure 4.5: Tracks of 10 MeV protons in water using an event-by-event algorithm. Each dot represent an interaction. Proton tracks are shown in blue, delta electrons are in red. [27] [37]

This kind of algorithms are becoming more and more useful, especially due to the rapid expansion of the hadron therapy [27]. In fact, if we are interested in computing the "actual" biological responses to radiation, we need to know the dose distributions at a microscopic scale that is comparable to the size of subcellular structures (from few nanometers to few micrometers). So, it is no longer sufficient to have averaged quantities on volumes of the order of the $\approx 1mm^3$. Moreover, quantifying the variance associated with the computed dose distribution becomes of primary importance in these applications. Consequently, a switch to event-by-event Monte Carlo algorithms is essential since the Boltzmann equation simply does not contain this type of information. In fact, since the Monte Carlo method is an inherently stochastic method, the simulation of particle trajectories allows us to compute the average deposited energy together with its variance also at small scales [27].

However, a major challenge for these algorithms are the large uncertainties that exist in particle interaction parameters (such as cross sections) at low energies; they typically involve very low tracking cut-off (on the order of 10 eV for the electrons) and, for this reason, are usually written only for specific materials [27].

To solve in an efficient way this kind of problems, it is necessary to go beyond the Boltzmann equation because it does not model the fluctuating characteristics of the radiation field. This is out of the scope of this work; however it is possible to find a form of the stochastic transport equation based on the fluctuation detector method in reference [27].

4.4 Assessment of Monte Carlo uncertainty

When we are dealing with Monte Carlo simulations, we must consider an intrinsic statistic uncertainty on the results. In fact, since such simulations remain limited by their finite nature, they are subjected to sampling variability. Hence, the deducted quantities will be only estimators of the actual ones and their variability is called '*Monte Carlo Error (MCE)* [38]. In particular, the MCE is defined as the standard deviation of the Monte Carlo estimator, taken across hypothetical repetitions of the simulation (always maintaining the same simulation design and number of repetitions R):

$$MCE(\hat{\phi}_R) = \sqrt{Var[\hat{\phi}_R]} \tag{4.6}$$

Without developing techniques that yield more efficient simulation (such as variance reduction techniques) , the uncertainty will be strictly related to the number of trials performed; as it increases, the statistical accuracy will increase as well [39].

Some simple and practical tools to estimate the MCE depending on the number of trials (for a given simulation design and quantity of interest) would be very useful since they would allow us to choose the size of the sample based on the desired accuracy. Alternatively, one could monitor the behaviour of the Monte Carlo estimate directly while the simulation is running, halting it when the estimator levels off at some stationary state. This can be done by simply live plotting the estimate of the quantity of interest while the number of repetitions R is increasing. However, this method does not provide an estimate of the MCE itself. [39]

A simple tool for quantifying MCE which could be used for a huge range of quantities commonly evaluated using the Monte Carlo technique is based on the so called *asymptotic theory.* Let's assume that the target quantity ϕ has an integral representation given by:

$$\phi = \int \phi(x) f_X(x) dx \tag{4.7}$$

In this case, given a sample of R replicates generated under the simulation design $f_{\mathbf{X}}(x)$, a simple Monte Carlo estimator of ϕ is the mean of the integrand computed across the R replicates.

$$\hat{\phi}_R = \frac{1}{R}\sum_{r=1}^{R}\phi(\mathbf{X}_r) \tag{4.8}$$

Now, applying the strong law of large numbers, $\hat{\phi}_R \to E[\phi(\mathbf{X})]$ as $R \to \infty$. In addition, under mild regularity conditions, taking $R \to \infty$ we can apply also the central limit theorem [39]:

$$\begin{aligned} &\sqrt{R}(\hat{\phi}_R - \phi) \to_d Normal(0, \sigma_\phi^2) \\ &\sigma_\phi^2 = E[(\phi(\mathbf{X}) - \phi)^2] \end{aligned} \tag{4.9}$$

From this result, an estimate of the MCE could be obtained directly from the replicates:

$$M\hat{C}E_{clt}(\hat{\phi}_R) = \frac{\hat{\sigma}_\phi}{\sqrt{R}} = \frac{1}{R}\sqrt{\sum_{r=1}^{R}(\phi(\mathbf{X}_r) - \hat{\phi}_R)^2} \tag{4.10}$$

So, such estimation is based on a single simulation with R replicates; the higher R, the better the estimate. In addition, thanks to this approach it is possible to estimate the number of replicates R needed to acquire a desired level of accuracy. This can be done using the so called *Bootstrap Grouping Prediction (BGP) Plot*, that is a graphical approach for characterizing MCE as a function of R. In fact, the asymptotic theory tell us that if $R \to \infty$, the magnitude of the MCE will be linear in $\frac{1}{\sqrt{R}}$. Furthermore, if $\frac{1}{\sqrt{R}} \to 0$, then also $MCE \to 0$. These facts can be used to plot the relationship of MCE and $\frac{1}{\sqrt{R}}$ estimating just one couple (R,MCE) in the simplest case. The slope of a fitted linear regression constrained to pass from the points (0,0) and (R,MCE) in the $(\frac{1}{\sqrt{R}}, MCE)$ plane can be used to predict the value of R for any desired level of MCE. The more couples (R,MCE) are available, the better the linear regression coefficient will predict such value [39].

Finally, it could be argued that simulation studies always should come together with some assessment of uncertainty. So, whenever feasible, in this work I will adopt this philosophy.

Chapter 5

Ultrasound Contrast Agents and Superheated Emulsions

Gas-filled microbubbles are routinely used in ultrasonic imaging to enhance image contrast [51]. The first generation of ultrasound contrast agents (UCAs) was made of free air bubbles. However, these were quickly dissolved in blood and it was difficult to make them homogeneous in size. So, currently used UCAs have a thin shell made of either proteins, lipids or surfactants that aim at reducing the capillary pressure and at preventing them from dissolving in the blood. Moreover, an airless core made of inert and non-toxic gases such as octafluoropropane and perfluorohexane is used; their low solubility in water allows generating stable microbubbles [51]. All UCAs have in common the feature that they are micro or nano sized particles that are highly echogenic. Indeed, since their core gases are much more compressible than water or tissue by several orders of magnitude, and their dimensions are smaller than the wavelength of conventional diagnostic ultrasound probe, they undergo volumetric oscillation during imaging, enhancing the image contrast [51]. The next generation of UCAs will combine imaging with therapeutic functionalities. By attaching ligands (such as antibodies, peptides or small chemical compounds) to the surface of the bubbles they can be designed to adhere to the membrane of targeted cells after injection. So, a targeted microbubble can be defined as a complex system containing a gas core, a shell and targeting ligands [51].

However, due to their typical diameters of 1-10 μm, designed to maximise the contrast enhancing effect, and short half-lives (about 1 min) their application range is still limited since they can't accumulate properly, they can't be applied for long-term imaging studies and their applications are limited to the vasculature. To overcome these limitations, phase-change contrast agents (PCCAs) have started being investigated and they have recently emerged as promising platforms for a variety of imaging and therapeutic applications, owing to their ability to extravasate and vaporise into microbubble contrast agents when locally triggered by acoustic or optical energy sources.

PCCAs in the form of liquid nanodroplets are generally injected intravenously. Then, after they have accumulated at a specific site, using an ultrasound transducer it is possible to vaporise them into gaseous microbubbles in a controlled way. Once “activated”, the microbubbles enhance the ultrasound image contrast and can release drugs for therapeutic applications. Moreover, nanodroplets exhibit a unique acoustic signature during the transition from a liquid nanodroplet to a gas microbubble; this can also be exploited to generate an ultrasound image. This acoustic emission is made of an exponentially decaying sinusoidal signal (Fig. 5.1) resulting from complex oscillatory dynamics until the final equilibrium state is reached. The frequency of the signal depends on the final microbubble diameter; the smaller the bubble, the higher the frequency [52].

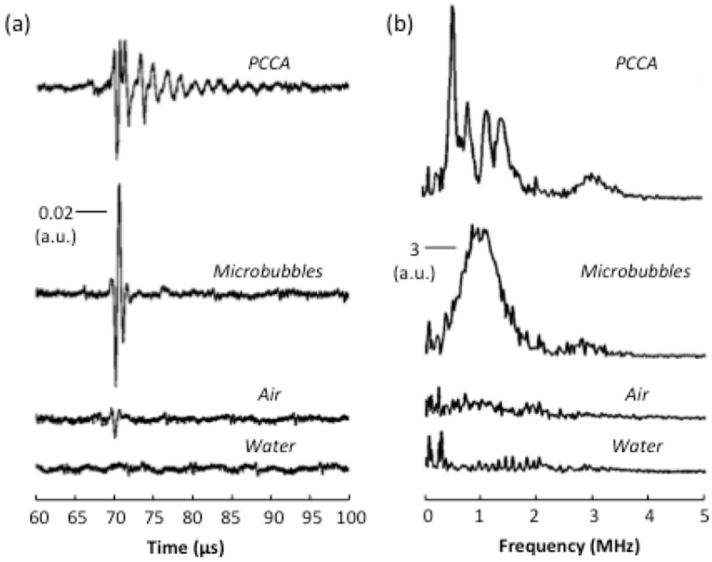

Figure 5.1: a. Raw acoustic signals from different contrast agents. b. Frequency spectrum. Signal and spectrum magnitude are in arbitrary units (a.u.) [52].

As we will see later on, it is possible to use the so called superheated emulsions as PCCAs. Superheated emulsions is the standard denomination adopted by the ICRU and ISO to indicate “any type of radiation detector using superheated drops, including superheated droplets detector and bubble detector" [40]. A superheated droplet detector (SDD) consists of a large number of micro sized superheated liquid drops that can be suspended in an aqueous viscoelastic gel or in a polymer matrix. It was invented by Apfel in the late 1970s and currently has various applications in high energy physics, medical physics and space physics.

So, the idea is to use superheated emulsions as PCCAs, exploiting the capability of ionising radiations to vaporise the droplets. This will allow, in principle, to develop an in-vivo SDD-like system using nanodroplets transforming into microbubbles.

Indeed, the liquid drops are used while in a metastable state at a temperature higher than the boiling point and lower than the critical temperature. Such state is called "superheated state" and the corresponding (T,p) values are found in the vapour region in the phase diagram (Fig. 5.2).

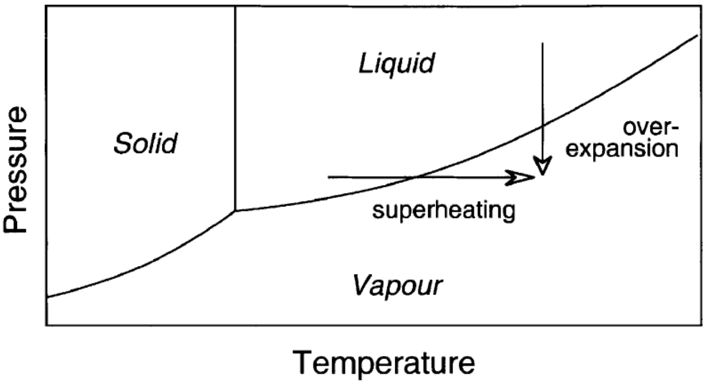

Figure 5.2: Example of phase diagram of a material [44].

Since the metastable state is fragile and short-lived, in order to keep it as long as possible, potential "heterogeneous nucleation" sites like gas pockets or microscopic particles should be avoided. For this reason the liquid should be fractionated into droplets and dispersed in an immiscible host fluid. This technique, called "emulsification", allows the creation of perfectly smooth spherical interfaces that are free of nucleating impurities. Obviously, to maintain such conditions the temperature should be not too high with respect to the boiling point and the emulsifier material should be clean and de-gassed. For a deeper insight in the manufacturing process the reader is referred to [44].

In a superheated state, it is possible to trigger the vaporisation by energy deposition of ionising radiation. The mechanism is the same as the one used in the bubble chambers developed by Glaser in 1952. However, the main difference between a SDD and a bubble chamber is that the former is continuously sensitive to radiation since the droplets are kept permanently in the superheated state while the latter completely loses its sensitivity after a vaporisation event occurs since it is not continuously kept in steady-state superheated conditions [41].

However, not every interaction between radiation and droplets leads to a vaporisation; in fact, as we will investigate later, sufficient energy must be deposited inside a superheated droplet in a prescribed critical length for a vaporisation to occur. The minimum amount of energy and the critical length depend on the composition of the emulsion and on the so called *degree of superheat* [41], which is a non-dimensional thermodynamic quantity that can be defined as “the normalised operating point of an emulsion within the temperature and pressure range corresponding to the potential existence of the metastable superheated state” [43]. It is indicated with s and it can be expressed as:

$$s = \frac{T - T_b}{T_c - T_b} \tag{5.1}$$

Where T represents the working temperature, T_b represents the boiling temperature and T_c is the critical temperature of the superheated emulsion. The choice of the composition of the emulsion (i.e. the use of different halocarbons in the formulation of the detector) and of the working temperature allows to tune the sensitivity to radiation, hence achieving a selective detection capability that will permit a wide range of applications. For instance, a relatively small degree of superheat makes the detector sensitive only to high LET radiations, while increasing it leads also to low LET radiation sensitisation [43].

Following vaporisation, the liquid droplet expands into a bubble; during this phase change acoustic signals are emitted, an expansion is present and at the end of the process the acoustic properties are changed. For this reason, the main methods used to detect the vaporisation events are based on the active detection of the acoustic signals, on the analysis of the acoustic properties (e.g. attenuation) or on the detection of the volume change [40].

The resonant frequency (with some second and third harmonics contribution) is equal to the frequency of maximum attenuation (maximum sound scattering); depending on the specific case, different formulas can be used to link the final bubble size to the resonant frequency [53]:

- Free bubbles:

$$f_M = \frac{1}{2\pi}\sqrt{\frac{1}{\rho R_0^2}[3\gamma P_0 + \frac{2(3\gamma - 1)\sigma_w}{R_0}]} \tag{5.2}$$

  Where R_0 is the bubble radius, ρ is the surrounding liquid density, P_0 is the ambient pressure in the surrounding liquid, σ_w is the surface tension of water, and γ is the gas polytropic constant that varies between 1 (isothermal) and 1.4 (adiabatic). As an estimation it is possible to set it to 1.4.

- Phospholipid bubbles:

$$f_M = \frac{1}{2\pi}\sqrt{\frac{1}{\rho R_0^2}[3\gamma P_0 + \frac{2(3\gamma - 1)\sigma_w}{R_0} + \frac{4\chi}{R_0}]} \tag{5.3}$$

  In the previous formula we add the contribution of the elasticity modulus of the bubbles χ (in N/m) . Typical values are 0.3-0.8 N/m.

A formula for polymeric bubbles (like the ones that are employed in this project) is not available. Moreover, in our case the shell parameters are not available with sufficient accuracy. So, for a rough estimate the free bubble formula is probably the more accurate for our purposes.

As an example, from acoustic vaporisation experiments conducted using C_4F_{10} droplets (with mean diameter of about $560nm$, it has been found that the mean diameter of the bubbles (after vaporisation) is 8 μm but it can go up to 12 μm (Fig. 5.3). Moreover, the detected vaporisation signals were in the range 0.4 - 1 MHz; this means that only the events from the largest droplets have been properly detected.

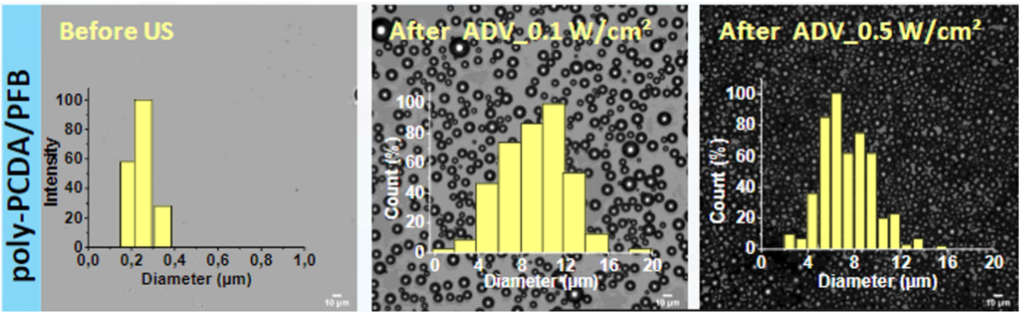

Figure 5.3: Size distribution before and after acoustic droplets vaporisation (ADV) in C_4F_{10} (perfluorobutane, PFB) droplets with a polymerised PCDA shell.

The narrow bandwidth of the ADV pulse combined with the low centre frequency of the receiving transducer allowed to discriminate between droplet vaporisation events and microbubble scattering signals, whose acoustic signatures differ both in time and in the frequency domain (Fig. 5.4).

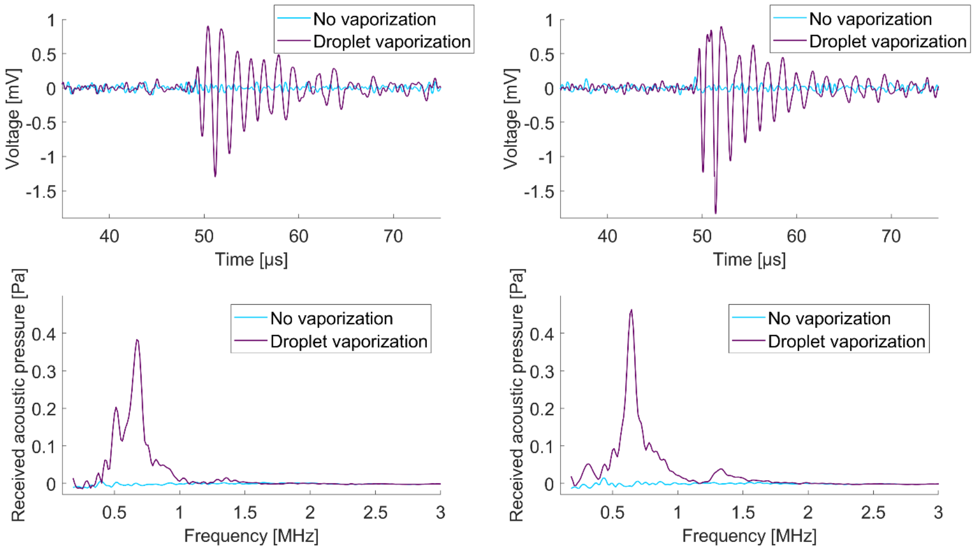

Figure 5.4: (Top) - Time domain signals of vaporisation events. (Bottom) - Associated spectrums in the frequency domain, for droplet vaporisation triggered by ADV [54].

Nowadays SE have reached their full maturity; several instruments have already been developed, in particular for neutron dosimetry and spectrometry. However, the physic of SE is somewhat complex and still not fully understood; the theoretical models that have been used in several papers to describe the radiation induced vaporisation are partly based on empirical relations. Consequently such models need to be fine tuned based on the specific case (i.e. SE type, operating conditions and radiation field) in order to obtain a good agreement with experimental results [43]. In the following section one of the most accepted theoretical models used to describe the radiation induced vaporisation will be presented.

5.1 Radiation induced vaporisation of superheated emulsions

The stability of a superheated liquid is determined by several factors, including trapped air-pockets, dirt and intrinsic microscopic voids that are present in every liquid. Each of them can nucleate the evaporation of liquid droplets. While the presence of air pockets and dirt can be reduced substantially by trapping the superheated emulsion droplets in a specifically treated medium (e.g. viscoelastic gel), the microscopic voids cannot be eliminated. The microscopic voids encounter different barriers to their growth; their stability against unlimited growth determine the stability of the superheated emulsion. The nucleation of any microbubble in a superheated droplet triggers the evaporation [50].

The minimum energy barrier to reach a critical size vapour embryo can be overcome by the average energy of thermal oscillation E_{th} of the microscopic voids itself. In fact, since $E_{th} = \frac{1}{2}k_B T$, already at room temperature there could be a small probability of spontaneous nucleation (depending on the nanodrops properties). Increasing the temperature has a double effect: firstly it increases E_{th} and secondly, as we will see, it decreases the energy barrier W_{min}. Consequently, the frequency of spontaneous nucleation increases as the temperature increases, and the liquid becomes unstable before the temperature actually reaches the physical limit T_c (above T_c the surface tension vanishes, making the energy barrier vanishing too) [50]. It is also possible to compute the probability that the barrier W_{min} will be overcome by thermal fluctuations:

$$P_{nucl} = e^{-\frac{W}{k_B T}} \tag{5.4}$$

It was observed that at a temperature T_{lim}, that is called "limit of superheat" (about 80% of the T_c), the superheated liquid becomes unstable and boils off spontaneously. Such limit has been determined by increasing the temperature of different light halocarbon emulsions until spontaneous vaporisation occurred in a low radiation background environment [42].

The nucleation can be triggered not only by thermal fluctuations, but also by an external deposition of energy. However, the energy must be deposited inside a droplet in a time scale that is small compared to the thermal diffusion time scale; this allows to use such energy locally to overcome the nucleation barrier W_{min} instead of heating up the surrounding superheated liquid. An energy deposit of this kind leads to the formation of a so-called *thermal spike* [47], potentially triggering nucleation [50].

In our case, we will focus on the energy deposit by ionising radiations as a thermal spike generation mean. So, our main assumption is that ionising radiation is able to deposit energy fast and locally in the form of heat by exciting or ionising atoms and molecules along its track.

The fluid dynamics problem of radiation induced vaporisation in a metastable liquid is extremely complex and still based on some empirical assumptions since a complete numerical approach will require a computational cost too high to permit a general use of such approach [42]. So, different semi-empirical approaches are based on the thermodynamics of the isothermal spontaneous nucleation modified according to the thermal spike theory (the reader is referred to [48] for a deep review) that have already been developed.

The main idea behind this theory is that the intense heating produced by ionising radiations induces localised boiling and generates trails of sub-microscopic vapour cavities inside the droplets. Such vapour cavities start growing against an energy barrier; if their radius becomes greater than a critical one, they overcome the barrier and start growing indefinitely leading to the vaporisation of the entire droplet, else they will collapse back to the liquid phase under the action of external pressure and surface tension. Even though a universally accepted quantitative theory still lacks, this idea is generally accepted [44].

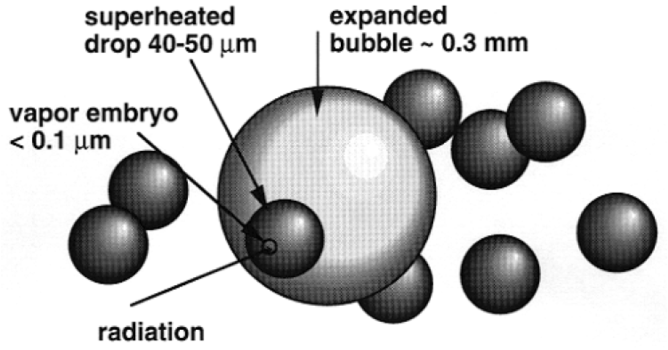

Figure 5.5: Bubble formation step in a superheated emulsion [41].

Applying the condition of mechanical equilibrium between the surface tension and the pressure difference over the walls of the vapour cavity it is possible to derive an expression for the critical radius:

$$R_c = \frac{2\sigma}{p'' - p'} \approx \frac{2\sigma}{[(p_s - p')(1 - \frac{v'}{v''})]} \tag{5.5}$$

Where σ is the surface tension at the liquid-vapor interface, p is the pressure, p_s is the saturation pressure and v is the specific volume. The apices $'$ and $''$ denote the liquid and vapour phases.

Then, studies on the neutron response of SDD, have verified the possibility to adopt an expression originally developed for bubble chambers to predict the energy barrier W_0 in the radiation-induced nucleation [44] :

$$W_0 = -\frac{4\pi}{3}R_c^3(p'' - p') + \frac{4\pi}{3}R_c^3\rho_v h_{lv} + 4\pi R_c^2(\sigma - T\frac{d\sigma}{dT}) \tag{5.6}$$

Here h_{lv} represents the latent heat of evaporation and ρ_v is the density of the gas phase. The first term is the reversible work done during expansion to a bubble of size R_c against the pressure of the liquid. Then the second term represents the energy needed to evaporate the liquid; if the subcritical bubble grows faster than energy can be supplied from its liquid vicinity, it should be provided by different means. The third term describes the work that is required to create the liquid vapour interface of the vapour embryo under the hypothesis of adiabatic process (it is reflected in the term containing $\frac{d\sigma}{dT}$).

Moreover, it is important to consider also irreversible energy losses W_{irr} caused by different dynamic phenomena present during the formation of a bubble. Main phenomena involved are:

- Contrasting action of viscous forces
- Acoustic wave emission

It is possible to estimate conservatively this contribute:

$$\begin{aligned} W_{irr} &= 2\pi\rho' R_c^3\dot{R}^2 \\ \dot{R} &= \frac{4D(\frac{\rho'}{\rho''})^{\frac{1}{3}}}{R_c} \\ D &= \frac{k}{\rho' c_p} \end{aligned} \tag{5.7}$$

Where $\dot{R}$ is the bubble-wall velocity, D is the thermal diffusivity of the liquid, k is the thermal conductivity and c_p the specific heat. W_{irr} could increase W_0 by more than 10% [42].

Depending on the temperature, $W_{tot} = W_0 + W_{irr}$ can be one order of magnitude higher than the work required for the isothermal spontaneous nucleation of a critical size bubble that is supposed to be in equilibrium with its surroundings W_G:

$$W_G = \frac{16\pi\sigma^3}{3(p_s - p')^2(1 - \frac{v'}{v''})^2} \tag{5.8}$$

The ratio $\eta = \frac{W_G}{W_{tot}}$ indicates the efficiency of the actual nucleation process compared to the reversible isothermal process that is supposed to happen in case of spontaneous nucleation of a critical bubble. The low values of η are due to the fact that most of the energy released by the ionising radiation is spent in latent vaporisation heat and work against viscous forces and some is “lost “ due to heat conduction.

The total vaporisation energy W_{tot} and the critical radius R_c have been calculated for several halocarbons (Fig. 5.6). However, it is necessary to point out that the computed values are affected by uncertainties of about 10% derived from uncertainties of thermodynamic parameters.

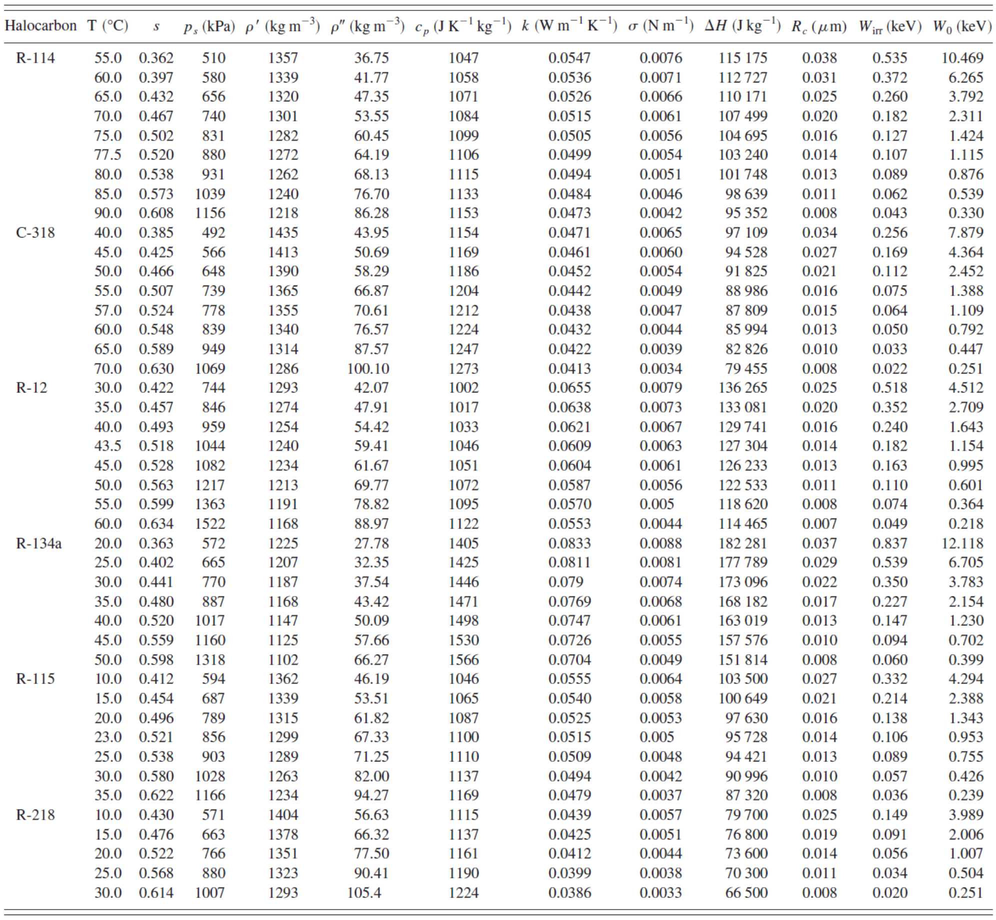

Halocarbon	T (°C)	s	p_s (kPa)	ρ' (kg m^{-3})	ρ'' (kg m^{-3})	c_p (J K^{-1} kg^{-1})	k (W m^{-1} K^{-1})	σ (N m^{-1})	ΔH (J kg^{-1})	R_c (μm)	W_{irr} (keV)	W_0 (keV)
R-114	55.0	0.362	510	1357	36.75	1047	0.0547	0.0076	115 175	0.038	0.535	10.469
	60.0	0.397	580	1339	41.77	1058	0.0536	0.0071	112 727	0.031	0.372	6.265
	65.0	0.432	656	1320	47.35	1071	0.0526	0.0066	110 171	0.025	0.260	3.792
	70.0	0.467	740	1301	53.55	1084	0.0515	0.0061	107 499	0.020	0.182	2.311
	75.0	0.502	831	1282	60.45	1099	0.0505	0.0056	104 695	0.016	0.127	1.424
	77.5	0.520	880	1272	64.19	1106	0.0499	0.0054	103 240	0.014	0.107	1.115
	80.0	0.538	931	1262	68.13	1115	0.0494	0.0051	101 748	0.013	0.089	0.876
	85.0	0.573	1039	1240	76.70	1133	0.0484	0.0046	98 639	0.011	0.062	0.539
	90.0	0.608	1156	1218	86.28	1153	0.0473	0.0042	95 352	0.008	0.043	0.330
C-318	40.0	0.385	492	1435	43.95	1154	0.0471	0.0065	97 109	0.034	0.256	7.879
	45.0	0.425	566	1413	50.69	1169	0.0461	0.0060	94 528	0.027	0.169	4.364
	50.0	0.466	648	1390	58.29	1186	0.0452	0.0054	91 825	0.021	0.112	2.452
	55.0	0.507	739	1365	66.87	1204	0.0442	0.0049	88 986	0.016	0.075	1.388
	57.0	0.524	778	1355	70.61	1212	0.0438	0.0047	87 809	0.015	0.064	1.109
	60.0	0.548	839	1340	76.57	1224	0.0432	0.0044	85 994	0.013	0.050	0.792
	65.0	0.589	949	1314	87.57	1247	0.0422	0.0039	82 826	0.010	0.033	0.447
	70.0	0.630	1069	1286	100.10	1273	0.0413	0.0034	79 455	0.008	0.022	0.251
R-12	30.0	0.422	744	1293	42.07	1002	0.0655	0.0079	136 265	0.025	0.518	4.512
	35.0	0.457	846	1274	47.91	1017	0.0638	0.0073	133 081	0.020	0.352	2.709
	40.0	0.493	959	1254	54.42	1033	0.0621	0.0067	129 741	0.016	0.240	1.643
	43.5	0.518	1044	1240	59.41	1046	0.0609	0.0063	127 304	0.014	0.182	1.154
	45.0	0.528	1082	1234	61.67	1051	0.0604	0.0061	126 233	0.013	0.163	0.995
	50.0	0.563	1217	1213	69.77	1072	0.0587	0.0056	122 533	0.011	0.110	0.601
	55.0	0.599	1363	1191	78.82	1095	0.0570	0.005	118 620	0.008	0.074	0.364
	60.0	0.634	1522	1168	88.97	1122	0.0553	0.0044	114 465	0.007	0.049	0.218
R-134a	20.0	0.363	572	1225	27.78	1405	0.0833	0.0088	182 281	0.037	0.837	12.118
	25.0	0.402	665	1207	32.35	1425	0.0811	0.0081	177 789	0.029	0.539	6.705
	30.0	0.441	770	1187	37.54	1446	0.079	0.0074	173 096	0.022	0.350	3.783
	35.0	0.480	887	1168	43.42	1471	0.0769	0.0068	168 182	0.017	0.227	2.154
	40.0	0.520	1017	1147	50.09	1498	0.0747	0.0061	163 019	0.013	0.147	1.230
	45.0	0.559	1160	1125	57.66	1530	0.0726	0.0055	157 576	0.010	0.094	0.702
	50.0	0.598	1318	1102	66.27	1566	0.0704	0.0049	151 814	0.008	0.060	0.399
R-115	10.0	0.412	594	1362	46.19	1046	0.0555	0.0064	103 500	0.027	0.332	4.294
	15.0	0.454	687	1339	53.51	1065	0.0540	0.0058	100 649	0.021	0.214	2.388
	20.0	0.496	789	1315	61.82	1087	0.0525	0.0053	97 630	0.016	0.138	1.343
	23.0	0.521	856	1299	67.33	1100	0.0515	0.005	95 728	0.014	0.106	0.953
	25.0	0.538	903	1289	71.25	1110	0.0509	0.0048	94 421	0.013	0.089	0.755
	30.0	0.580	1028	1263	82.00	1137	0.0494	0.0042	90 996	0.010	0.057	0.426
	35.0	0.622	1166	1234	94.27	1169	0.0479	0.0037	87 320	0.008	0.036	0.239
R-218	10.0	0.430	571	1404	56.63	1115	0.0439	0.0057	79 700	0.025	0.149	3.989
	15.0	0.476	663	1378	66.32	1137	0.0425	0.0051	76 800	0.019	0.091	2.006
	20.0	0.522	766	1351	77.50	1161	0.0412	0.0044	73 600	0.014	0.056	1.007
	25.0	0.568	880	1323	90.41	1190	0.0399	0.0038	70 300	0.011	0.034	0.504
	30.0	0.614	1007	1293	105.4	1224	0.0386	0.0033	66 500	0.008	0.020	0.251

Figure 5.6: Thermophysical data and computed vaporization energies for some light halocarbons [42].

It should be noted that, as introduced before, a non-dimensional thermodynamic parameter called “reduced superheat” allows to condense the behaviour of different light halocarbons; in fact, when W_{tot} and R_c are plotted versus s, they all coincide on the same curve (Fig. 5.7) [44]. Moreover, a close correlation between the degree of superheat and radiation detection thresholds has been found. For instance, neutron detection thresholds, sensitisation to photons and spontaneous vaporisation occur around the same degree of superheat for different SDD [43]. However, this is not surprising since the light halocarbons employed in the SDD belong to the same fluids class.

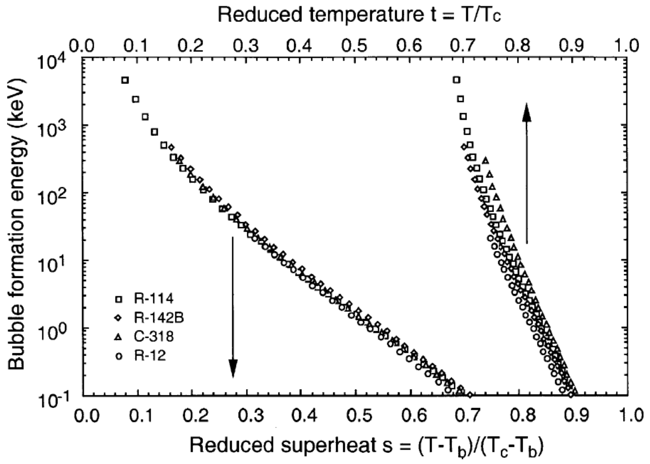

Figure 5.7: Computed bubble nucleation energy for superheated emulsions of different light halocarbons versus reduced superheat and reduced temperature [44].

In order to have a radiation-induced phase transition, the locally deposited kinetic energy of an incident particle must exceeds W_{tot}. Moreover, it has been found that the local Linear Energy Transfer (LET) of the particle must be large enough to supply W_{tot} as heat over a critical distance L_c that is greater than a critical diameter. This can be explained supposing that a trail of vapour cavities should initially extend along the charged-particle track before it can quickly acquire a spherical shape (Fig. 5.8) [55]:

$$E_{dep}(T) = \int_0^{L_c(T)} \frac{dE}{dx} dx \geq W_{tot}(T) \tag{5.9}$$

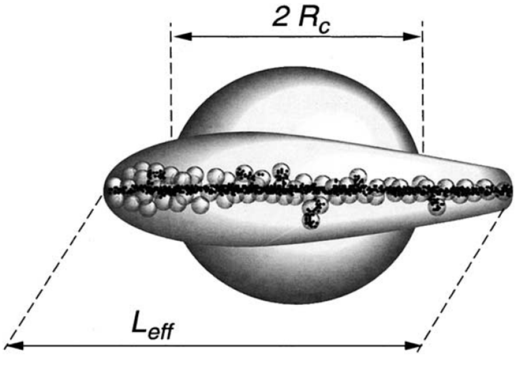

Figure 5.8: Formation of an embryonic bubble of critical size [44].

Since R_c is the natural length scale of the vaporisation process, the critical distance that is needed is usually supposed to be proportional to R_c. However the proportionality coefficient k (that will be called *nucleation parameter*) varies a lot from author to author: even if a value of 2 seems to be intuitively justified and is supported by experimental data for low energy thresholds (below 20 keV), some authors propose values around 6 and others up to 12 [55]. This uncertainty in the model makes an experimental calibration of the nucleation parameter for each experimental setup (i.e. operating temperature, superheated emulsion and radiation field involved) strictly required in order to obtain more accurate estimations of the superheated emulsion actual behaviour. Moreover, it has been reported that a nucleation can be triggered also if the minimum energy requirement has not been overcome; in that case the nucleation probability diminishes as the energy shortfall increases [50].

The minimum threshold should be overcome by an energy deposit along a single radiation track; synergistic effects due to multiple energy deposits in the same droplets by different radiations simultaneously have not been reported. This has been investigated by *M. Takada et al.* increasing the proton flux incident on a bubble detector and comparing the "proton sensitivity" (computed as the ratio between the number of bubbles formed and the number of protons incident on the detector). No significant increase in such parameter has been found [46].

Different kinds of ionising radiation can achieve nucleation transferring energy to the superheated droplets in different ways:

- Ions, recoil nuclei, protons and alpha particles: they mainly excite the electrons of the materials that they encounter along their track. In particular it has been found that protons can trigger the nucleation both via nuclear reactions (as long as their energy is higher than the required threshold) and via Coulomb scattering (when the degree of superheat is sufficiently high).

- Neutrons: in this case, since they mostly create recoil nuclei by elastic scattering or energetic ions by low-energy nuclear reactions, bubble formation is induced by the generated highly ionising charged particles. This allows a clear discrimination of sparsely ionising radiations such as electrons or photons just by tuning the degree of superheat.

- Electrons: they deposit their energy in a less localised way with respect to heavier charged particles. They initially trigger bubble vaporisation at the end of their range, where the LET is sensibly higher.

- Photons: they create light charged particles by means of photoelectric production, Compton scattering or pair productions. Then such particles will deposit their energy with the processes described above.

The photon sensitisation phenomenon has been observed, for instance, by irradiating several light halocarbon emulsions and recording their response at increasing temperature steps. Counting the formation of bubbles, for each detector a " photon sensitisation temperature" above which the count rates increase rapidly has been identified. It has been found that such photon sensitisation arises for each emulsion approximatively at a reduced superheat value of 0.51 (Fig. 5.9). A similar relationship between temperature and vaporisation has been established for the irradiation of chlorocarbons with thermal neutrons; the sensitisation of all chlorocarbons corresponds to a reduced superheat of about 0.33 (Fig. 5.10) [44].

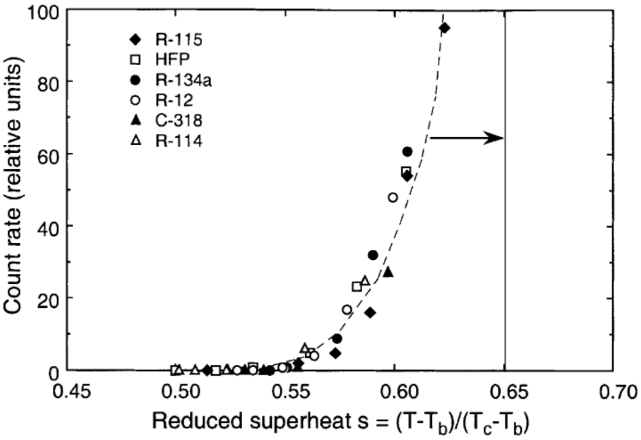

Figure 5.9: Photon sensitisation of superheated emulsions made by different halocarbons. The vertical line represents the reduced superheat limit common to all halocarbons [44].

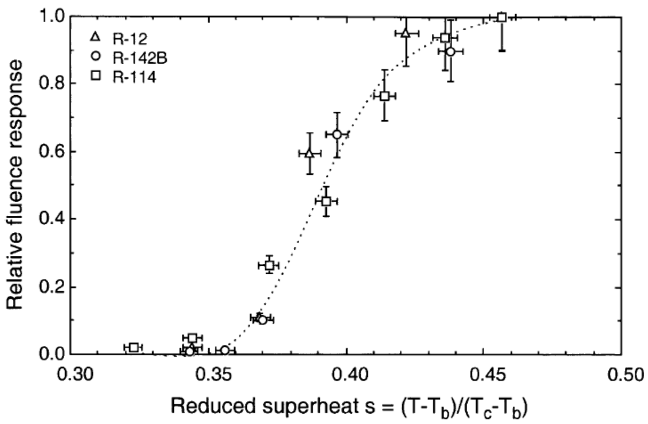

Figure 5.10: Thermal neutron sensitisation of superheated emulsions made by different chlorocarbons [44].

The sudden evaporation is followed by an acoustic emission in both the sonic and ultrasonic frequency range (depending on the bubble size) that is used as a “signature” of the vaporisation event in the so called active detection method. In fact, it is worth to underline that the droplets nucleate independently from each other, since the acoustic pulses are too weak to trigger new nucleations [50]. Moreover, the different energy deposition pattern and time scales between different ionising radiations is expected to affect the nucleation dynamics and the high frequency content of the evaporation acoustic pulses, allowing a more detailed characterisation of each event. To have more insight, the reader is referred to [49].

Since at the same time the vaporisation is accompanied by a volume expansion, this phenomenon is exploited to detect the event in the so called passive detection method [50].

5.1.1 Superheated droplets detector: applications

The small dimensions of such detectors and their ability to discriminate the radiation contribution of photons have contributed to a huge development of this technology for neutron personal dosimetry; in fact, that is one of the most common application of the superheated emulsions. Using a combination of passive bubble damage detectors it is possible to provide good estimates of neutron dose equivalent in radiation environments typical of the nuclear industry [43]. Moreover, since they rely only on the optical counting of the bubbles that remain trapped in the polymer matrix, they are relatively simple compared to the active devices. To overcome the counting issues related to the overlapping of the formed bubbles, a mechanism for the mechanical pressurisation of the detector is present, which has to be applied after each use to re-condense the formed bubbles. In addition, a passive temperature compensation system is adopted to minimise the temperature dependence of the response [44].

Superheated emulsions are also typically involved in the measurement of photoneutrons around high energy X-ray beams. The passive selective counting capability of such detectors allows to detect such photoneutrons without showing saturation issues that could be present in active detectors due to the intense and pulsed primary photon beam [43]. For these applications, passive detectors based on dichlorofluoromethane (R-12) have been developed. They are comprised of a vial that contains tens of thousands of $\approx 60\mu m$ droplets in the bottom part, while the upper part contains inert gel only (Fig. 5.11).

Figure 5.11: Superheated drop detector based on volumetric counting. Adapted from [44].

When vapour bubbles form, an equivalent volume of inert gel is displaced into graduated pipettes that are connected to the vial caps. Such detectors show a response that closely matches the kerma-equivalent trend in the energy region that is relevant for photoneutrons (Fig. 5.12); so, provided CPE is attained at the point of measurement, it can be used to compute accurate dose-equivalent at depth in tissue [44].

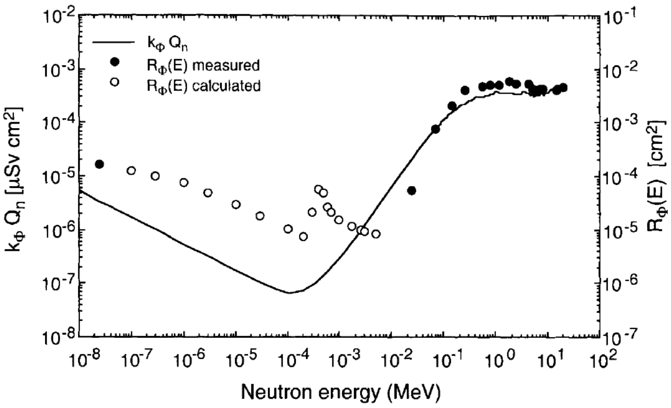

Figure 5.12: Fluence response $R_\phi(E)$ of a R-12 superheated drop detector compared to the "kerma equivalent factor" $k_\phi Q_n$ [44].

Since it is also possible to register bubble nucleations acoustically, active detection methods based on the detection of the acoustic pulses that are emitted during the formation of the bubbles have been developed. In general, a double piezoelectric transducer configuration is used for the comparative pulse-shape analysis of the signals that come from both the detector and the external noise channels. After a proper elaboration, the shape and amplitude of the signals are analysed and each time they match those of a real bubble-formation event, a pulse is counted. With respect to the passive counting methods, the active ones theoretically allow to record as many events as the number of droplets contained in the detector without the need of a re-pressurisation step. However, the response becomes non-linear due to the depletion of the detector and this must be accounted for. In addition, due to both the intrinsic duration of a bubble pulse and pulse analysis time requirements, superheated detectors based on active counting techniques are extremely slow compared with most radiation detectors, making them not suitable for all physics experiments. Nevertheless, they are fast enough for radiation protection applications [43].

Neutron spectrometry can be also carried out using detectors based on the passive or active detection technology; in the former case several bubble damage detectors with different energy thresholds are adopted, while in the latter case temperature controllers are used to regulate the temperature of the emulsion, allowing to vary the detection threshold continuously. They have important applications in the nuclear fusion technology since they allow the measurements of neutrons above $\approx$ 16 MeV. This is made possible thanks to their insensitivity to neutrons of lower energy coming from the plasma and to photons from (n, γ) reactions. The resulting tail neutron spectra can be used to obtain information on the spatial and energy distributions of confined alpha particles in deuterium-tritium tokamaks [43].

Even though the use of superheated emulsions in neutron dosimetry and spectrometry is the main reason for their popularity, different applications have been developed. For instance, large superheated emulsion chambers with extremely fine suspensions of droplets in a heavy viscous gel have been developed in order to perform the 3-D dosimetry of photon-emitting brachytherapy sources. Through the bubble distribution that forms after having inserted a source inside such detector chamber it is possible to visualise the radiation field. For instance, such bubble distribution can be visualised using magnetic resonance or optical tomography techniques. After imaging, it is possible to re-condense the bubbles in the liquid phase by pressurising the detector. This will allow to use it again for repeated measurements thus improving the counting statistics [43].

Relevant applications are also present in cold dark matter investigation; superheated emulsions are employed to look for weakly interacting massive particles. In this case, the superheated emulsions are operated at a high degree of superheat, below the photon sensitisation threshold. A huge improvement in cold dark matter sensitivity is expected from these detectors [43].

Moreover, as already mentioned, extravascular ultrasound contrast agents, or nanodroplets, also make use of superheated liquids as core material, and are able to extravasate thanks to their small dimension. Then, after having reached the target organ, they are activated by ultrasound or light to form microbubbles that enhance imaging contrast. Ongoing research aims at exploiting the same procedure to deliver drugs; i.e. the superheated emulsions are capable of carrying a payload that will be delivered locally only upon activation [45].

5.1.2 Parametric analysis for C_4F_{10} and C_3F_8

By applying the reported semi-empirical model, a preliminary parametric analysis for different nanodroplets has been developed. The choice of the droplet liquid core material is dictated by theoretical considerations on the required degree of superheat, the biological compatibility and the stability. Consequently, superheated nanodroplets with a perfluorobutane and octafluoropropane liquid core (boiling point. -2°C and -39°C, respectively) encapsulated in a polymerised fatty acid monolayer shell of 10,12 pentacosadiynoic acid (PCDA) have been chosen.

The aim of this analysis is to give an overview of W_{tot} , R_c and of the minimum LET requirement at different temperatures for each core material. For such analysis, even though the mean diameter of the nanodroplets that have been used is on the order of $560nm$, the Laplace pressure contribution has been neglected. In fact, there is a study in which the vaporisation transition was measured as a function of the temperature for C_4F_{10} and C_3F_8 nanodroplets ($1\mu m$ mean diameter) coated with a lipid shell; it turned out that such nanodroplets experienced 90% vaporisation at 75°C and 40°C respectively. Since the resulting temperatures are near the theoretical superheat limit (80%-90% of the critical temperature), they concluded that the prevailing effect that led to the observed metastability of the superheated emulsions doesn't come from the droplet Laplace pressure that alters the boiling point, but comes from the intrinsic metastability of the pure superheated fluid against homogeneous nucleation of a critical vapor embryo. Then, even though the intramolecular cohesion forces of the shell could slow down the vaporisation process increasing its activation energy, also the effect of the shell has not been included in the model [45].

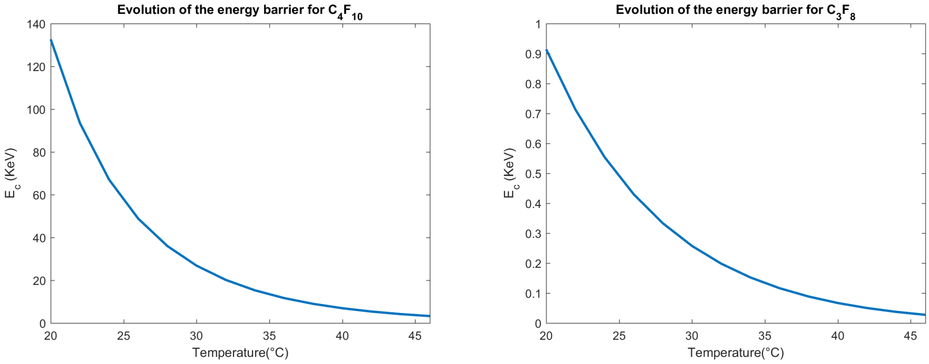

Figure 5.13: W_{tot} computed for C_4F_{10} (Left) and C_3F_8 (Right) as a function of the temperature

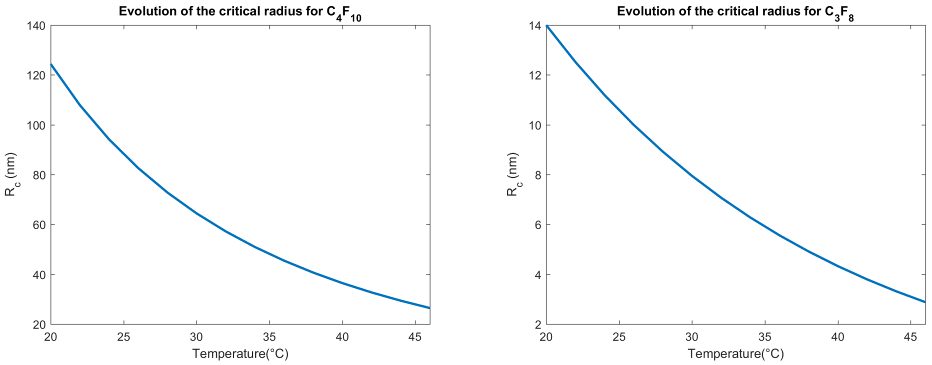

Figure 5.14: R_{crit} computed for C_4F_{10} (Left) and C_3F_8 (Right) as a function of the temperature

Next to the energy barrier and the critical radius values for both the core liquids, the minimum LET requirement is computed as a function of the temperature and varying the nucleation parameter k from 2 to 12.

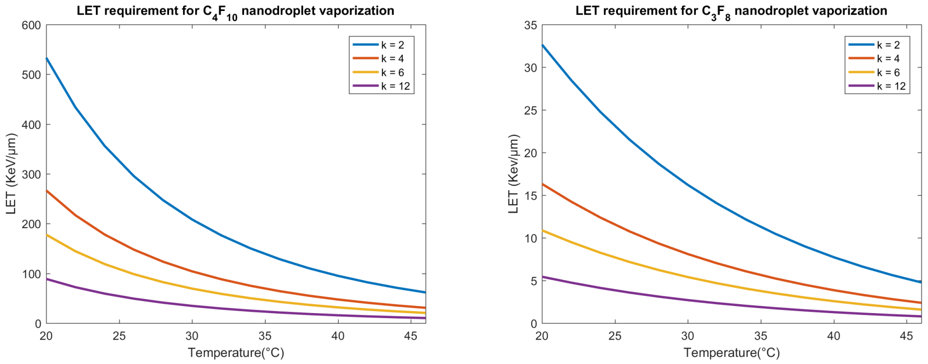

Figure 5.15: Minimum LET requirement computed for C_4F_{10} (Left) and C_3F_8 (Right) as a function of the temperature

We can immediately notice that, if the parameter has been chosen wrongly huge differences could arise, especially at low temperatures. So, it will be of extreme importance to validate the Monte Carlo model through performing experiments that will allow to tune such parameter in order to match the results. Consequently, since no validation has been done, at the moment this represents the major uncertainty in the results of the simulations that have been performed.

Moreover, from the values of the LET requirement computed at 35°C in the worst case scenario (k = 2, LET requirement around 150 keV/um for C_4F_{10}, around 13 keV/um for C_3F_8), we can conclude that C_3F_8 would be definitely better than C_4F_{10} as a proton range verification tool since it allows to clearly distinguish the vaporisations due to Coulomb scattering that are abundant in the Bragg peak region.

Chapter 6

Simulation of superheated emulsions response

To understand the response of superheated emulsions detectors in different conditions (e.g. radiation source, nanodroplets core, nanodroplets concentration, nanodroplets radius, temperature) without performing time consuming and expensive experiments one has to take recourse to simulation. As we already mentioned, the main uncertainties will come from the semi empirical theory that should be used to describe the radiation induced vaporisation process; nevertheless, some estimates can be made. In this work, the response of superheated emulsions detectors made of C_4F_{10} or C_3F_8 to protons or photons was investigated using the Geant4 simulation toolkit. All the outputs were analysed using ROOT[57] and MATLAB[56].

Geant4 (GEometry ANd Tracking code) is an object-oriented Monte Carlo toolkit that allows to simulate the transit of particles through matter. First developed by CERN, its areas of application include high energy, nuclear and accelerator physics, as well as studies in medical and space science [59, 60]. It consists of a broad collection of C++ class libraries that can be used to build up a fully customised simulation program. Geant4 version 4.10.04.p2 was used in all simulations.

To build up an application, it is mandatory to implement at least:

- Main file: in this file user interface, user classes and run manager should be declared.
- Sources and header files: it is necessary to build different user classes through inheritance from already built G4 classes. Among them, there are three classes that are mandatory in order to run a simulation:

- Primary Generator Action: in this class the primary particles source must be defined. In our case, a G4ParticleGun was used in all the simulations and was properly configured according to the actual source characteristics.
- Detector Construction: here materials (taken from the internal NIST database or newly defined starting from basic elements), geometry and sensitive detectors should be defined. Sensitive detectors can be attached to geometric volumes in order to extract information about the interactions that will occur in such volumes.
- Physics List: here particles to be tracked and processes that need to be simulated (each one with their own model) must be specified.

A typical simulation is divided hierarchically in different elemental units [59]:

1. **Run**: a run is initiated every time a */run/beamOn/* command is executed. It is a collection of primary particles shot (i.e. histories).

2. **Event**: every primary shot in a run constitutes an event. Each event is associated to a particular primary particle track and it carries all the information about it and about all the secondary particles that are generated. To store information, it is possible to associate different *hit collections* to each sensitive detector that has been defined; at the end of each event, all the hit collections are read and their content can be sent in an output file or can be directly elaborated to produce histograms.

3. **Track**: it is a snapshot of a particle. It keeps current information of a particle and it is updated after each step. Only when all the tracks are terminated (E_{kin} under the pre-defined energy cut, particle out of geometric boundaries or particle disappeared in an interaction) the current event is terminated.

4. **Step**: it is the smallest simulation unit. It contains the particle properties that are updated each time a process is invoked. Only after a step is completed, it is possible to extract information from it.

Geant4 is able to simulate particle interactions with matter using different electromagnetic, hadronic and optical physics models. Nowadays its capabilities have also been extended; for instance, thanks to the Geant4-DNA project, it is now possible to simulate direct and non-direct ionising radiation effects in water at the DNA scale using specific electromagnetic physics models that are valid down to the sub-eV scale [59].

In Geant4 each physical interaction is described by a "physics process" class that must be properly implemented in the code in order to "activate" its simulation. Moreover, for each physics process it is necessary to define at least one "model" class that includes the physical model needed to simulate such process. It is possible to define multiple model classes for a single physical process; they can be either "alternative" (applicable to identical energy ranges but each one holds in a particular geometrical region) or "complementary" (applicable to different energy ranges). For instance, regarding the electromagnetic processes models, they are subdivided into two main sub-packages: the "standard" ($1keV \leq E \leq 10TeV$) one and the "low-energy" ($\approx 100eV \leq E \leq 100GeV$) one [59]. Within parenthesis is represented the so called "energy cut off" value; it is defined as "the energy of a particle at which the computations are terminated and the residual particle energy is deposited at the site of interaction rather than transported to other regions" [32]. Low energy models require more CPU performance but they allow to simulate a variety of low energy processes (i.e. fluorescence emission, Auger electron production).

Photons processes are the only ones that by default are simulated in a discrete way; this means that all the interactions are explicitly simulated on a step-by-step approach [59]. This is possible thanks to the fact that their mean free path is big enough to have a limited number of interactions in each track. Instead, other ionising particles such as electrons and protons are in general simulated using condensed history algorithms in Monte Carlo transport codes. However, such condensed history algorithms tend to break down in spatial scales of a mean free path (e.g. scales in which there are few interactions) [58]. Consequently, particular attention is needed if detailed simulations in the nanometre scale are foreseen.

An important part of a Geant4 simulation is the definition of the simulation domain. The main steps involved are:

1. Specify the materials:

   There are different ways to specify a material. The easiest way is through the NIST database manager; there are lots of materials already built in that are ready to use (with densities computed at standard temperature and pressure, in general). Otherwise, starting from the elementary isotopes, it is possible to build molecules, compounds and mixtures. Then, for each material a density should be defined; in our case, the variation of the density of the droplets core with temperature has been considered making a polynomial fit of the data that are reported in [61].

2. Create the geometric solid:

   After having defined all the materials, the next step involves the creation of a G4VSolid object. It contains only information about the shape and the size of the solid.

3. Create the logical volume:

   Assigning a material (i.e. all the physical properties) to a G4VSolid object creates a logical volume. Moreover, at this stage it is possible to assign a sensitive detector to logical volumes.

4. Create the physical volume:

   This is the final step. It involves the placement of logical volumes inside the simulation domain. For each placement a *mother volume* must be specified: the coordinates used to define the position of the *daughter volume* are relative to the coordinate system of the mother volume. So, a physical volume is a positioned instance of a logical volume inside another logical volume. One or more logical volumes can be placed in a mother volume, but overlaps must be avoided. A unique physical volume which represents the experimental area must exist and it must fully contain all other volumes. It is called *world volume* [59]. Every time a particle exits the world volume it is considered lost and it is no longer tracked.

It is also possible to define *regions*; they represent a collection of physical volumes that can share their own energy cut-off values, step-size limit and physics models.

In order to estimate the quantities of interest, it is necessary to collect information from the simulated interactions. This process is called tallying. To achieve this aim, it is possible to use the so called *sensitive detectors*. They are able to create "hit objects" using information from steps along a particle track. In fact, every time a step is composed in a logical volume in which a sensitive detector is attached, a sub-routine written inside the sensitive detector code is called [59]. Through such sub-routine it is possible to create and store an "hit object" containing all the relevant information about the interaction.

For instance, in order to tally the fluence of particles crossing a surface perpendicularly, we need to count the average number of particles crossing the surface, dividing each contribution by the area of the surface and the cosine of the angle between the direction of travelling and the normal to the surface. As a result we get an estimation of the total fluence. If we count only particles with a certain energy we obtain the energy distribution of the fluence.

Even if there exist several built-in sensitive detectors, they can provide information only grouped at the event level [59]; in our case, this is not sufficient since we need to store information step by step in order to identify possible vaporisation events. So, customised sensitive detectors were built in order to store the LET in each step inside the superheated nanodroplets. Moreover, also a customised sensitive detector able to score the fluence together with the particle ID and kinetic energy was built.

Finally, the outputs of the simulations have been analysed using ROOT and MATLAB. The former is an Object Oriented framework that was developed specifically to overcome several issues related to the management and the analysis of large amounts of data (i.e. data coming from Large Hadron Collider experiments on a daily basis). It is entirely written in C++ and it includes tools for advanced statistical analysis and for visualisation. The command and scripting language is C++. However, it supports integration with other languages such as R or Python, but for the purpose of this work C++ was used. So, even if it is not intuitive with respect to other tools, it is extremely powerful for handling a large amount of data [57].

6.1 Geant4 simulation framework

Simulation studies using the Geant4 toolkit have been carried out to predict the response of the superheated emulsions under different experimental conditions. In addition, in order to simulate a real experimental setup using a standard workstation (HP Z440) in a reasonable time, an approximate acceleration technique has been developed and validated.

The entire simulation framework (Fig. 6.2) can be schematised in the following way:

1. **Generation of droplet positions**: this first step has been carried out using MATLAB. An algorithm that aims at generating centers of a given number of non-overlapping spherical droplets in a given volume has been developed. A flowchart of this algorithm is depicted in Fig. 6.1.

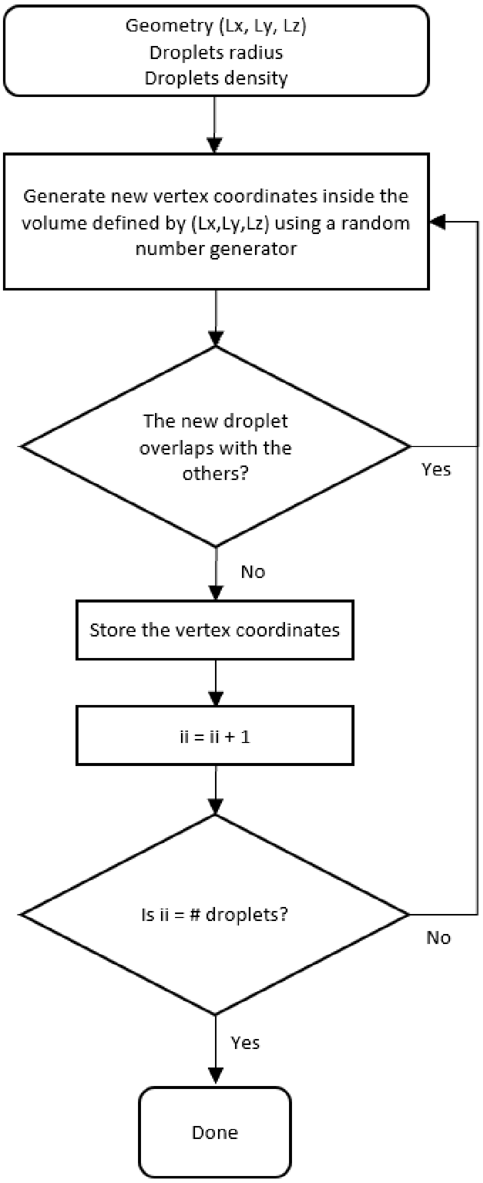

Figure 6.1: Algorithm for the generation of droplets position. Flowchart.

2. **Probability kernels computation**: the second step concerns the computation of the vaporisation probability kernel for the ionising particles that have been identified as "relevant" for a given application. A probability kernel must be computed once for each given set of input parameters (temperature, droplet concentration, layer thickness , maximum energy, energy bin width, phantom material). These

simulations are the most computationally expensive and are made using Geant4 and ROOT. The theoretical model for the radiation induced vaporisation has been coded for the post-processing of the output data from the Geant4 simulations. For each parameters set it computes the minimum LET requirement and it compares such value with the LET recorded in the droplets in order to look for vaporisation events.

3. **Event simulation**: the third step deals with the simulation of the real experimental setup using the input parameters set defined in the previous step. The sensitive volume is subdivided into layers perpendicular to the beam axis and the energy distribution of the fluence of each relevant ionising particle in each layer is scored and exported in a .txt file.

4. **Post-processing**: In the last step, the energy distribution of the fluence in each layer is imported into a ROOT application. Then, a convolution between the probability kernels computed in the second step and the fluences is made in order to get an estimate of the expected number of vaporisations in each layer (i.e. along the beam axis). The results are exported in a text file for their final elaboration in MATLAB.

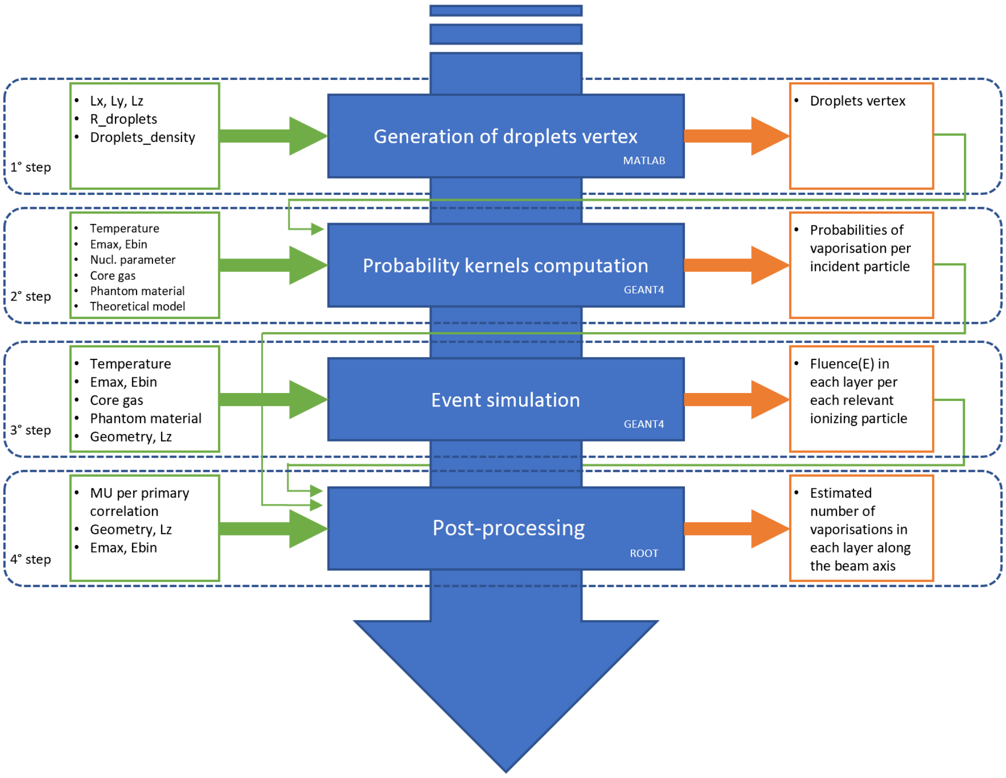

Figure 6.2: Simulation framework overview.

So, in order to estimate the number of vaporisation events along the beam axis the whole procedure has been subdivided into two sub-procedures; first a set of simulations is made to get the vaporisation probability kernel and then a simulation using the actual experimental conditions (i.e. geometry, primary beam characteristics...) is performed to score the fluence of ionising particles that are travelling through the layers. For simplicity, from now on the first set of simulations will be called *Simulation A* and the latter will be called *Simulation B*. The final result will be an estimate of the number of vaporisations along the beam axis per Monitor Unit (MU)[1] for a given set of experimental conditions.

All the relevant physical parameters for the core fluid have been obtained from [61]. Several polynomial fits have been carried out in order to use them in the ROOT analysis script giving as an input only the operating temperature and the core fluid type. Only the surface tension values have been taken from [44].

---

[1] A monitor unit (MU) is a measure of machine output. The output dose per MU of a therapeutic radiation beam is traditionally calibrated under specific reference conditions (beam energy, field size, depth in water, etc.).

Finally, several simplifying hypotheses have been made:

1. Monodisperse droplets: even though the actual size distribution of the droplets is not monodisperse, in order to simplify the simulation setup a mono-disperse size distribution (corresponding to the mean diameter) has been chosen. However, we should bear in mind that the larger the droplet, the shorter is its lifetime in the radiation field since the particles are more likely to deposit energy inside its volume.

2. Droplets amount in the phantom fixed: even in case of vaporisation, they have not been removed from the simulation domain. However, since the volume fraction of droplets is very low (less than 1%), the total vaporisation fraction that is achieved at the end of the simulation is low, thus not affecting the results notably.

3. Laplace pressure: the Laplace pressure contribution was neglected because there was insufficient information to quantify it. Indeed, the droplets surface tension has not been measured and therefore the Laplace pressure contribution can't be estimated. However, if the pressure inside the droplet is above the atmospheric pressure the vaporisation probability will decrease (becoming null if the pressure is so high that the droplets are no more superheated). In our case we have assumed that the encapsulated droplets have null surface tension, hence the Laplace pressure contribution is not present.

4. Homogeneous spontaneous vaporisation events due to thermal agitation have not been modelled.

In the following sections the proposed approximate acceleration technique will be presented and validated. To do so, the simulation A will be fully described. Finally, the simulation B will be explained and the main results will be presented.

6.2 An approximate acceleration technique

Since our nanodroplets have a mean diameter of about 560nm, we need a step-by-step simulation approach in order to identify tracks inside the droplets with a sufficient accuracy. For the same reason, we will need low-energy physics models since an energy cut-off of 100 eV corresponds to an electrons range of about 10 nm in water. Moreover, below a few hundred of eV we have the maximum LET value for electrons.

However, simulating charged particle trajectories down to 100 eV using a step-by-step approach is extremely computationally intensive and as such impossible to apply to the entire simulation domain, which has dimensions that are several orders of magnitude larger (centimetre scale). Moreover, the total amount of droplets to be simulated in a macroscopic geometry is huge and the tracking of particles in such a geometry will be extremely slow due to its complexity.

So, to deal with the multi-scalarity present in our geometry, different physics models for each physical region were implemented; a more detailed low energy single scattering model has been used inside the nanodroplets, while a condensed history model has been used in other regions. This combination of models can be implemented in the “physics list” class of the Geant4 simulation application. In that class the list of particles to be tracked, the physical processes for each particle to be considered and the corresponding physics models should be declared. Moreover, if multiple models are adopted for the same process, their range of applicability (in terms of energy interval and/or geometrical region) should also be declared. All the available models, their range of validity and all these procedures are well described in [58].

However, even when using this approach, when it comes to simulate the droplets response in a macroscopic geometry, the huge computational time makes the simulation not affordable. In order to overcome this issue, an approximate acceleration technique has been developed and validated in a geometry that is small enough to make the simulation possible in a reasonable time.

The developed technique can’t be defined a *variance reduction method* since it reduces the variance of the estimated droplet response (keeping the same simulation time) but, at the same time, it introduces systematic errors, making the expectation of such response different with respect to a simulation that doesn’t adopt this technique [27]. While, a variance reduction method would reduce the variance of the response without introducing systematic errors. For instance, the use of condensed history algorithms or the use of an energy threshold (both as cut-off value and as production threshold) also represents an approximate acceleration technique.

However, for our aims, such newly introduced errors can be neglected; in fact, we will be mostly interested in obtaining the shape of the vaporisation curve and a rough estimate of the amount of vaporisations that are produced in particular conditions.

The underlying idea is the following: instead of simulating the whole experimental setup with a huge amount of droplets inside, we can split the simulation into two parts; first we compute the probability that a given primary particle with energy E_{pr} will produce a vaporisation event while travelling along a layer of thickness t_l. Then, we convolve such probability kernel with the energy distribution of the fluence that will be scored in layers with the same thickness in a simulation made without considering the presence of the nanodroplets. This technique is based on the assumption that each particle is like an independent Bernoulli trial with a given probability of success (e.g. vaporisation) that remains constant during the whole irradiation experiment; consequently, the total number of vaporisations will be distributed like a binomial random variable and its expected value will be just the product between the probability of success and the number of trials.

In this way, the only computational intensive simulation will be the first one; actually it will involve several simulations performed at increasing beam energies for each primary particle that is assumed to be "relevant" from the vaporisation probability point of view. For instance, if the primary beam is made of photons, since their main effects are due to the free electrons that are produced in the interactions, the only probability kernel that is needed is the one computed using electrons.

So, the basic brick is the computation of the probability of vaporisation due to an ionising particle of type k (k = protons, electrons ...) with an initial energy i incident on a layer of thickness t_l , having the temperature $T = T_{exp}$, the nucleation parameter $k = k_{exp}$ and the droplets type (C_4F_{10} or C_3F_8) and concentration $C_{drop} = C_{drop,exp}$ fixed. In order to do so, a geometry composed by a water layer of (Lx, Ly, t_l) dimensions was built and a number of droplets given by $N_{drop} = C_{drop} * V_{layer}$ was distributed randomly inside it. A schematic of the geometry setup is depicted in Fig. 6.3.

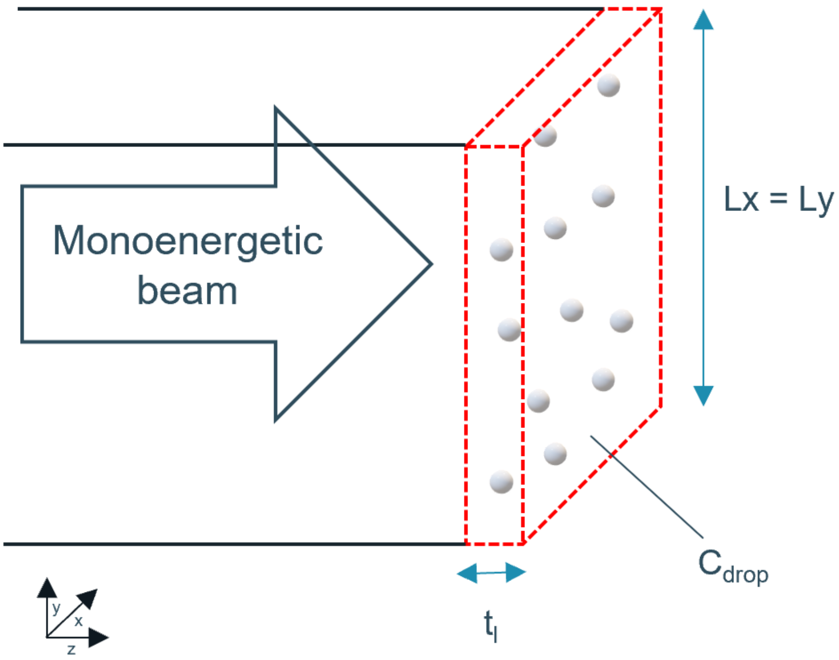

Figure 6.3: Scheme of the simulation domain.

Then, a primary source of type k with energy i has been set up and the physics packages have been selected. To achieve better results, accurate low-energy step-by-step physical models are used inside the region identified by the droplets while standard models are used elsewhere. It is worth to underline that, thanks to the reduced dimension of the domain, the computational effort remains affordable even if accurate step-by-step physics models are involved.

Each droplet can be identified individually because it is tagged with a unique ID in the geometry part of the simulation. The simulation will provide in output the LET of each ionising particle in each step in a droplet. If the LET value is higher than the minimum LET requirement that is computed according to the radiation induced vaporisation theory, a vaporisation event is counted. During the data analysis vaporisation events due to the same ionising particle in the same droplet have been discarded.

Once the probability kernel has been computed for each relevant ionising particle of type k and each energy i, it is stored in a .txt file that will be imported in a ROOT script for the convolution with the fluence values that will be scored in the simulation B. In fact, if Φ_{ij}^{k} is the scored incident flux of particle type k with energy i on the layer j and p_i^k is the probability of vaporisation computed for particle type k with energy i, the estimated number of vaporisation events in a phantom with M layers will be given by:

$$Vap_{events} = \sum_{k=1}^{P}\sum_{i=1}^{N}\sum_{j=1}^{M} p_i^k(\Phi_{ij}^k A) \tag{6.1}$$

Where N is the number of energy bins, P is the number of relevant particles to be considered and A is the incident area of the layers in the simulation B. However, such estimated value will depend on the number of primaries used in the simulation and an additional term is needed to make it comparable with a real experiment. So, a conversion factor K has been included in the above formula:

$$\begin{aligned} Vap_{events}(1MU) &= \sum_{k=1}^{P}\sum_{i=1}^{N}\sum_{j=1}^{M} p_i^k(\Phi_{ij}^k K A) \\ K &= \frac{(primaries - per - MU)}{number - of - primaries} \end{aligned} \tag{6.2}$$

Finally, the vaporisation fraction is computed as:

$$Vap_{fraction}(1MU) = \frac{Vap_{events}}{N_{drop}} \tag{6.3}$$

The conversion factor K “scales” the fluence so that it matches the one that would be present if a given number of MU are delivered. Such linear scaling is possible thanks to the linearity of the Boltzmann equation; the effect (for instance in terms of secondaries fluence) of a given number of primaries (the source term) is directly proportional to it. This fact is clearly shown in Fig. 6.4.

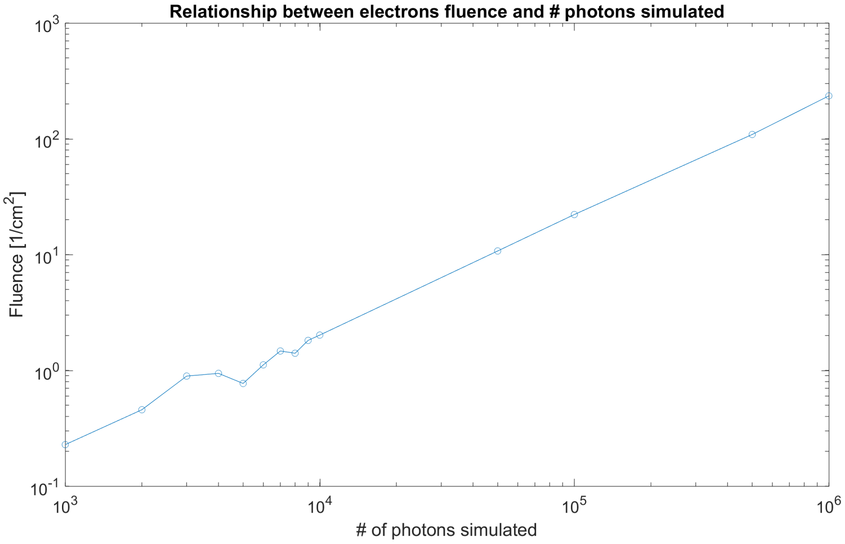

Figure 6.4: Linearity of the primary-to-fluence conversion. Oscillations are present when the number of primaries is low due to the prevalence of the statistical uncertainty

For the simulations involving a photon beam, the photons-per-MU factor have been estimated using Geant4 itself. In fact, the linac that has been used in the experiments is calibrated in a way that the monitor chamber reads 1 MU when the dose delivered at 10 cm depth in a water phantom placed at SSD = 90 cm using a 10x10 cm field size is equal to 0.8 cGy. So, an estimated value of the primaries-per-MU factor has been determined building a geometry identical to the one used for the calibrations and scoring the dose deposited at 10 cm depth. This procedure has been repeated increasing the number of primaries to estimate the uncertainty using a BGP plot (Fig. 6.5). The final estimate is $2.2 * 10^{-13}$ MU-per-photon with a relative error that is less than 0.5% (Fig. 6.6).

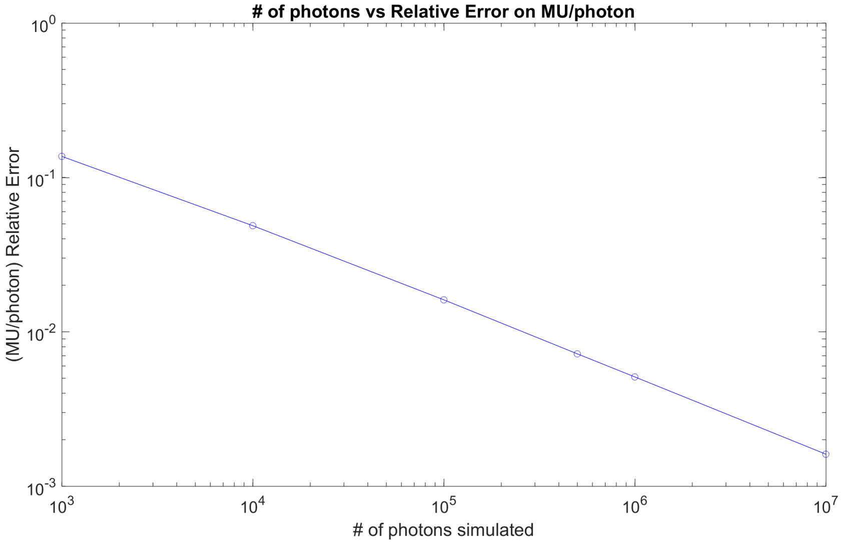

Figure 6.5: MU-per-photon Bootstrap Grouping Prediction plot. The relative error follows the same behaviour of $N^{-\frac{1}{2}}$, where N is the number of photons simulated.

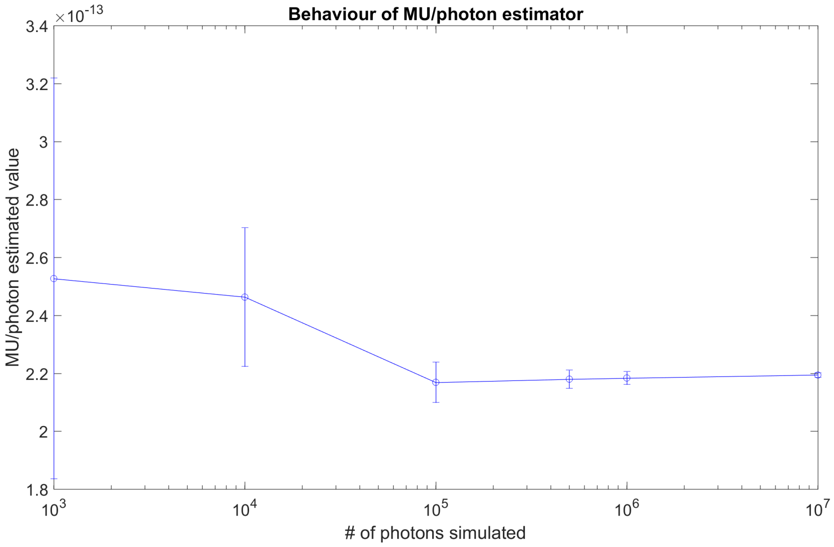

Figure 6.6: Behaviour of the MU-per-photon estimator

For the simulations involving the proton beam, a protons-per-MU factor of around 10^8 for a 60 MeV beam has been estimated using tabulated values for different beam energies provided by the Cyclotron Resource Centre

(UCLouvain) for the proton beam in which the phantom experiments will be performed in the near future.

The accuracy of such probability kernels will depend on several factors. Among them, major contributions come from:

- The energy bin width: depends on the particle, on the energy range and on the material. For instance, the LET of electrons is more or less constant from 1 MeV until 10 MeV in water, while it increases a lot as the energy goes down from 1 MeV to 100 eV. So, if electrons in the low energy range are produced, a sufficiently narrow energy bin width should be applied to estimate their effects in terms of triggered vaporisations. To cope with this LET behaviour, an adaptive energy bin width was applied depending on the energy interval under consideration.

- The number of histories: increasing the number of histories that are used to estimate the probability at each energy will increase the accuracy of the estimation. To set it to a reasonable value, it is important to bear in mind that the final number of vaporisation events in the layer for every energy should be sufficiently large in order to have a low statistical uncertainty. In fact, if the number of events is high, the 68% confidence interval is approximately equal to the estimated probability value $\pm\delta$, where δ is the standard deviation computed as the square root of the estimated value [64].

- The area of the layer: increasing the area of the layer up to the real dimensions that it has in the macro scale geometric setup will increase the accuracy since it will allow to consider more and more backscattering events that otherwise will be neglected (as soon as a particle moves out the world region, it is considered lost). Moreover, the bigger the geometry, the better will the random droplets distribution response approximate the actual one.

- The thickness of the layer: this parameter can also affect the accuracy of the estimation. In order to accurately estimate the vaporisation probability due to particles with an energy that makes their mean free path very small, a layer with a comparable thickness would be better in order to assure that they will encounter at least some droplets before they stop. In fact, randomly positioning droplets in a bigger layer could result in no droplets near the entrance border, leading to zero interactions between low energy particles and them. So, in case such particles are the majority, a thin layer would be a better choice. However, since in the simulation B the same thickness must be used, a layer too thin would result in both an increased computational time (each boundary will increase the complexity of the simulation) and an increased uncertainty on the scored fluence values for the same number of histories.

Applying this method, we are implicitly assuming that the amount of droplets in the phantom is fixed: in fact, even in case of vaporisation, they will not be removed from the simulation domain and the different ionising particles that are flowing through the layers will vaporise droplets with a given probability irrespective of the others. Only in the “full” simulation that will be used for validating this approach double counting of vaporisations will be avoided in the post-simulation analysis, while when using the approximated technique no controls can be made.

Moreover, when a proton beam is used as a source, even in a “full” simulation, errors due to an overestimation of the average material density along the proton tracks (that, in case of vapour, will be lower) are present. A possible increase in the proton range will not be recognised at all. This effect will be negligible in case a photon beam is involved.

6.2.1 Validation of the approximate acceleration technique

In order to validate the approximate acceleration technique, a small trial geometry composed of a 3 cm cubic water phantom with a 1 mm cubic sensitive volume placed in the middle has been generated. This allows to simulate the nanodroplets’ response with and without the approximate technique; in fact, with a small geometry, even if a “full simulation” is requested, the computational effort will be sufficiently low to get results in a reasonable time.

In the actual simulation (the one without the approximate acceleration technique) 500 000 non-overlapping nanodroplets were randomly dispersed in the sensitive volume achieving a concentration of $5 * 10^8 \frac{droplets}{ml}$ and a sensitive detector able to score the LET of the ionising particles was attached to each. After the simulation, the results were analysed using ROOT applying the semi-empirical theoretical model presented in the previous chapter. In that way, it was possible to identify all the vaporisation events that were triggered (N_{vap}). Finally, the computed vaporisation fractions were plotted subdividing the phantom length along the beam axis into 100 parallel layers having thickness $t_l = 0.01mm$.

Then, the same geometry was used to simulate the droplets response applying the approximate technique. Now, instead of having the nanodroplets dispersed inside the sensitive volume, it was subdivided into 100 layers perpendicular to the beam direction with $t_l = 0.01mm$ and $Lx = Ly = 1mm$ and a sensitive detector able to score the fluence of each relevant ionising particle (only electrons for the photon beam, electrons, protons and neutrons for the proton beam) in different pre-defined energy bins was attached to each layer (Fig. 6.7). The energy bins were chosen according to the primary beam characteristics and to the ionising particle type.

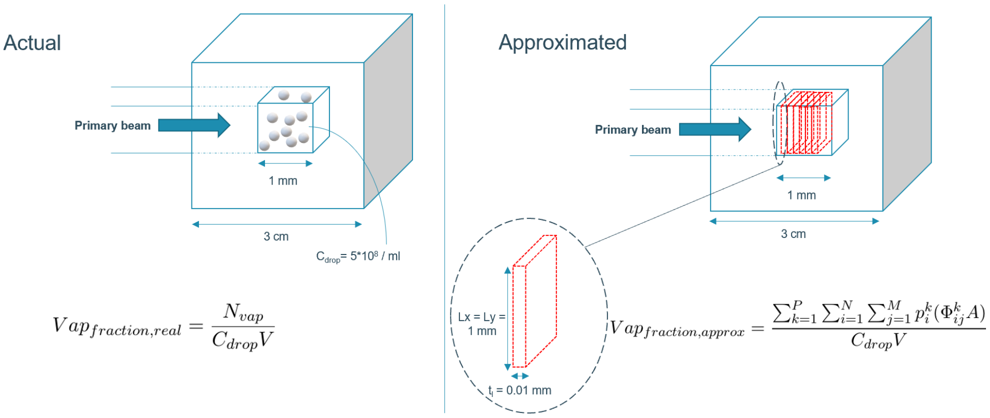

Figure 6.7: Validation of the approximate acceleration technique. Comparison between actual and approximated simulations.

The fluences were finally convoluted using the formula presented in the previous section with a probability kernel computed using a single layer characterised by $t_l = 0.01mm$, $Lx = Ly = 0.1mm$ and $C_{drop} = 5 * 10^8 \frac{droplets}{ml}$ (Fig. 6.8).

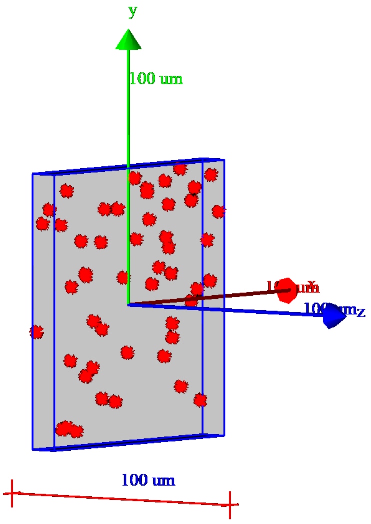

Figure 6.8: Simulation domain used for the probability kernels computation. Screenshot taken from Geant4 GUI.

At the end, the plots depicting the number of vaporisations along the beam axis were superimposed and the deviation between the "full" simulation and the approximated one was determined by computing the "mean absolute percentage error" (MAPE) between each estimated vaporisation fraction value:

$$
\begin{aligned}
MAPE^i &= \frac{\left|Vap^i_{fraction,real} - Vap^i_{fraction,approx}\right|}{Vap^i_{fraction,real}} \\
MAPE &= \frac{\sum_{i=1}^{N} MAPE^i}{N}
\end{aligned}
\tag{6.4}
$$

Where i represents the layer index, N is the number of layers, $Vap^i_{fraction,real}$ is the estimated number of vaporisations in layer i and $Vap^i_{fraction,approx}$ is the estimated number of vaporisation in layer i computed using the approximate method.

As far as the uncertainty on the vaporisation fraction is concerned, one standard deviation (δ) has been taken into account. However, its estimation was done in different ways:

- Standard deviation for $Vap_{fraction,real}$: in this case the final number of vaporisations is just obtained by directly counting vaporisation events that occur randomly with a low probability. So, if such number is sufficiently high its distribution (initially Poissonian) will approach a Gaussian distribution [64]. This allows to consider the 68% confidence interval by just taking one time the standard deviation (computed as the square root of the mean value) [64].

- Standard deviation for $Vap_{fraction,approx}$: since the final value is given using a convolution formula in which there are different uncertainties associated with each term, things are more complicated. In order to compute the standard deviation of the final result, the uncertainties should be propagated carefully through the various mathematical operations. This was done according to [65].

In all the following plots, one standard deviation is used to define the error bars.

According to the presented scheme, two simulations using a photon beam and a proton beam were performed:

- **Validation using a primary photon beam**: in this case a typical photon beam generated by a linac operating at 6 MV was used as a source. The probability kernel was computed only for electrons setting $E_{max} = 5MeV$ and $E_{bin} = 0.02MeV$. Such values have been chosen after the analysis of the electrons fluence inside the phantom (Fig. 6.9).

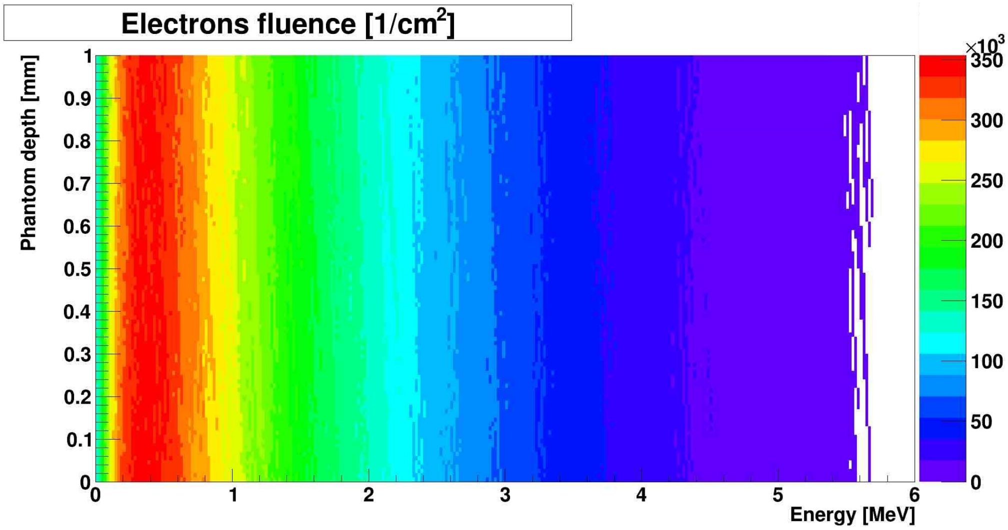

Figure 6.9: Validation of the approximate acceleration technique using a primary photon beam. Electrons fluence inside the sensitive volume (1e6 histories simulated).

It is worth reminding that in a photon beam the electron fluence shows a slight decrease after the dose build-up has taken place due to the beam attenuation (transient charged particle equilibrium). So, since the local LET remains more or less constant along the photon beam path and the electron fluence slightly decreases, it is possible to assume that in our case the vaporisation profile will be linear, with a slight decreasing trend. In fact, a linear fit was used in the post-processing of the result with good results; it has allowed to better compare the actual and approximate simulations compensating for the variance of the actual simulation data points.

In order to have a sufficient number of vaporisation events without simulating a considerable number of histories, two simulations (one using C_4F_{10} and one using C_3F_8) at temperatures near the superheat limit T_{lim} were performed:

- Validation using C_4F_{10}: this simulation was run at 65°C. The computed critical radius is $\approx 10nm$, the energy barrier is $\approx 0.419keV$ and the LET threshold computed using a nucleation parameter equal to 6 is $\approx 6.98\frac{keV}{\mu m}$. The actual simulation was run using 10^9 primaries, while the approximated one included 10^7 primaries; for this reason, in order to compare the results they were normalised to the number of primaries. The results are shown in Fig. 6.10 and Fig. 6.11.

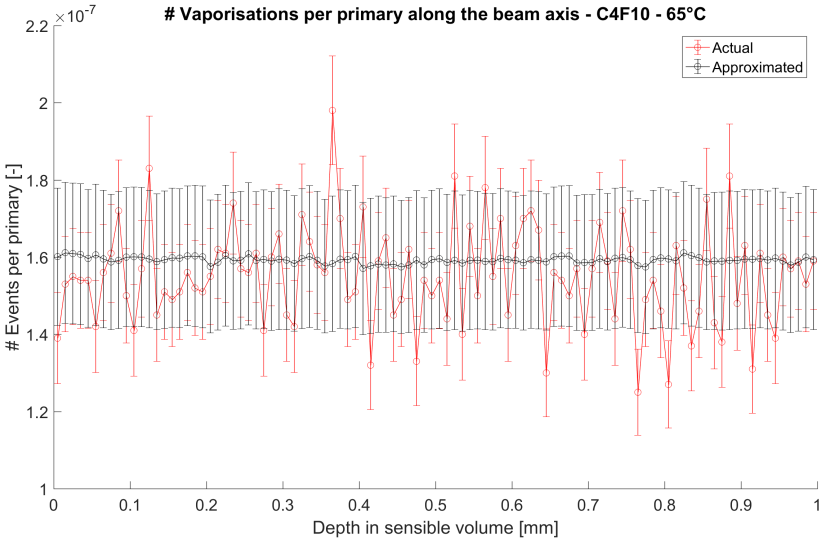

Figure 6.10: Validation of the approximate acceleration technique using a photon beam and C_4F_{10} as core gas. Comparison between the raw output data of both simulation approaches.

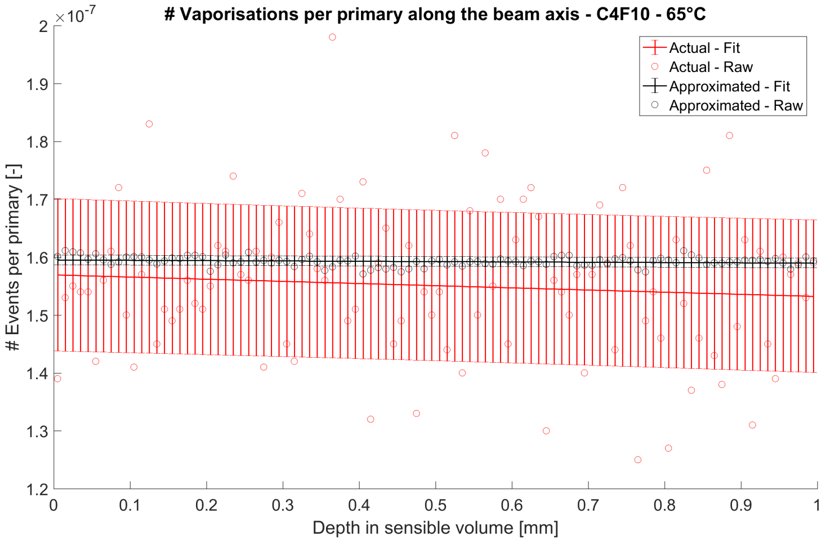

Figure 6.11: Validation of the approximate acceleration technique using a photon beam and C_4F_{10} as core gas. Comparison between the linear fits on the respective output data of both simulation approaches.

The MAPE computed using the raw data is 7.1% while the one computed using the linear fits is 2.7%.

- Validation using C_3F_8: this simulation was run at 35°C. The computed critical radius is $\approx 5.9nm$, the energy barrier is $\approx 0.125keV$ and the LET threshold computed using a nucleation parameter equal to 6 is $\approx 3.53\frac{keV}{\mu m}$. The actual simulation was run using 10^9 primaries, while the approximated one included 10^7 primaries. The results are shown in Fig. 6.12 and Fig. 6.13.

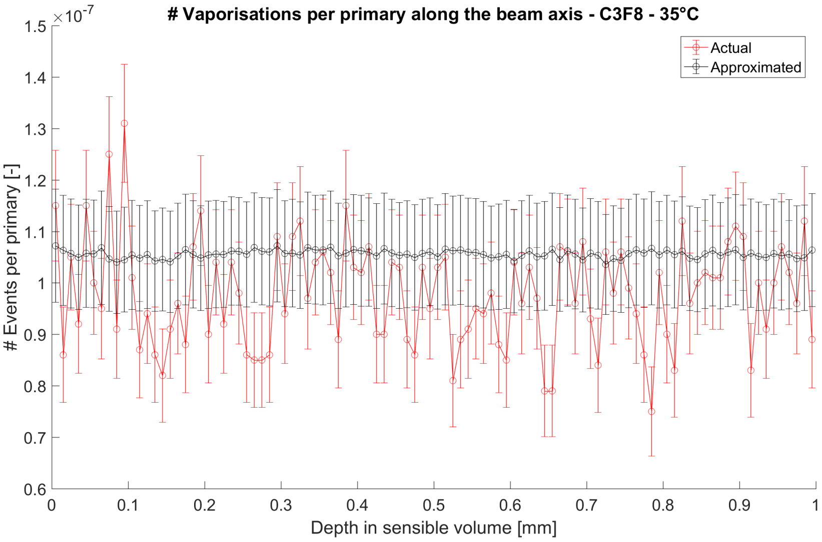

Figure 6.12: Validation of the approximate acceleration technique using a photon beam and C_3F_8 as core gas. Comparison between the raw output data of both simulation approaches.

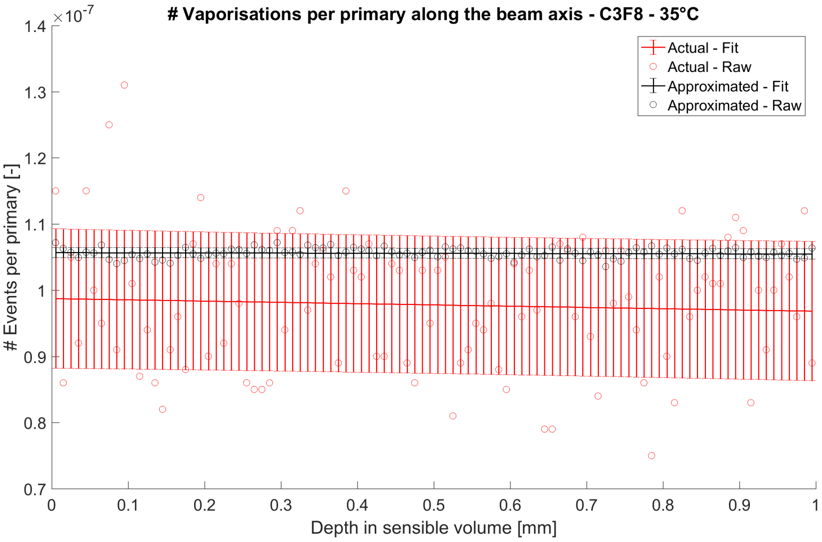

Figure 6.13: Validation of the approximate acceleration technique using a photon beam and C_3F_8 as core gas. Comparison between the linear fits on the respective output data of both simulation approaches.

The MAPE computed using the raw data is 11.4% while the one computed using the linear fits is 8.0%.

- **Validation using a proton beam**: a second validation of this technique was performed using a 22.5 MeV mono energetic proton beam as a source. The energy of the beam was chosen in order to have the Bragg peak inside the sensitive volume; this allows to better check the capability of the approximate technique to catch the droplets behaviour in such region. In this case the probability kernel was computed for electrons, setting $E_{max} = 0.02 MeV$, and $E_{bin} = 0.001 MeV$ and for protons, setting $E_{max} = 10 MeV$ and $E_{bin} = 0.1 MeV$. E_{max} and E_{bin} were determined based on the fluence values inside the sensitive volume; for instance, the electron fluence at energies above 0.02 MeV is negligible (Fig. 6.14). The same idea applies to protons (Fig. 6.15).

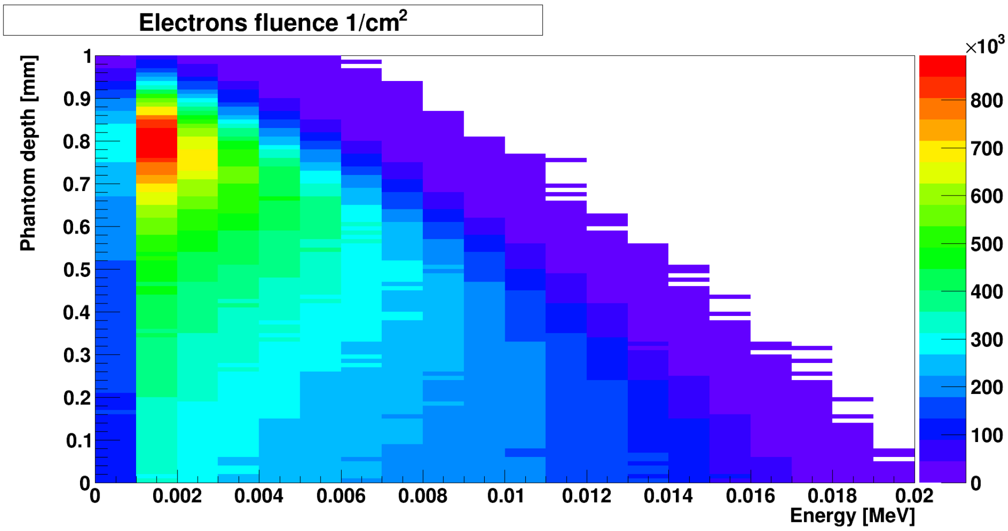

Figure 6.14: Validation of the approximate acceleration technique using a primary proton beam. Electron fluence inside the sensitive volume. 5e5 histories simulated.

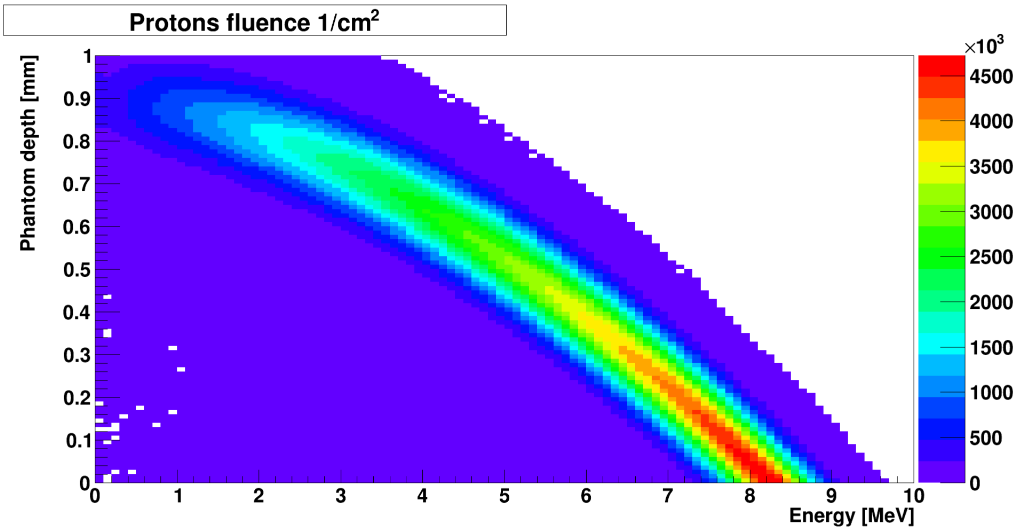

Figure 6.15: Validation of the approximate acceleration technique using a primary proton beam. Proton fluence inside the sensitive volume. 5e5 histories simulated.

Two simulations (one using C_4F_{10} and one using C_3F_8) were performed at the same temperatres as for the photon simulations. Moreover, for each simulation the post-processing was performed using three different nucleation parameter values: 2, 6 and 12.

- Validation using C_4F_{10}: at 65°C the computed critical radius is $\approx 10nm$ and the energy barrier is $\approx 0.419keV$. The LET threshold was computed using different nucleation parameter values:

Nucleation parameter	**LET threshold** $[\frac{keV}{\mu m}]$
2	20.45
6	6.82
12	3.41

Table 6.1: Minimum LET threshold for C_4F_{10} at 65°C computed using different nucleation parameter values.

Both the actual and the approximated simulations were run using $5 * 10^5$ primaries. The results are shown in Fig. 6.16.

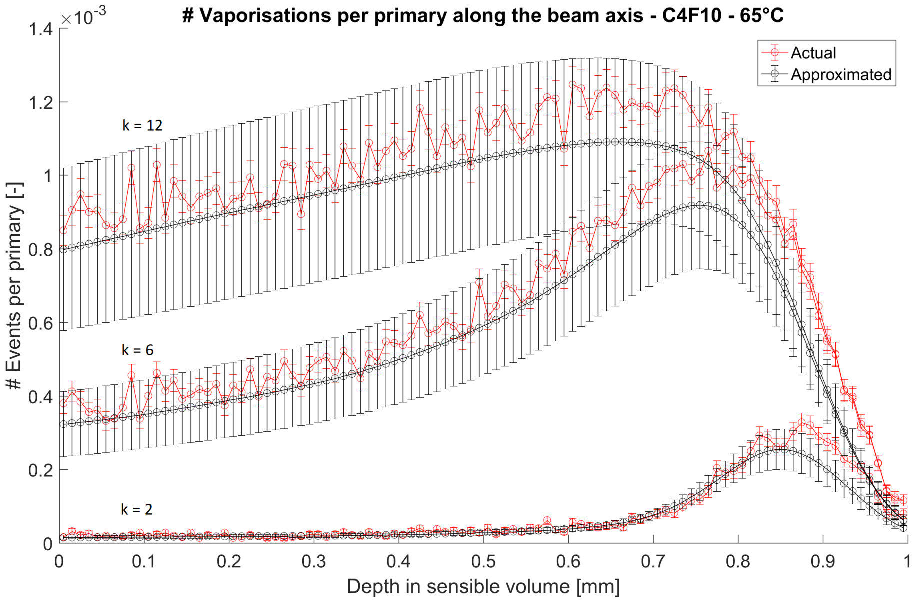

Figure 6.16: Validation of the approximate acceleration technique using a proton beam and C_4F_{10} as core gas. Comparison between raw data using different nucleation parameter values.

The MAPE decreases as the nucleation parameter increases: 19.7% at k = 2, 12.5% at k = 6 and 11.3% at k = 12. This behaviour can be explained in the following way: increasing the value of k, the number of vaporisation events increases too. This reduces the statistical uncertainty, leading to an overall better agreement between the two simulations.

- Validation using C_3F_8: at 35°C the computed critical radius is $\approx 5.9 nm$ and the energy barrier is $\approx 0.125 keV$. Also in this case the LET threshold was computed using different nucleation parameter values:

Nucleation parameter	LET threshold $[\frac{keV}{\mu m}]$
2	10.57
6	3.53
12	1.76

Table 6.2: Minimum LET threshold for C_3F_8 at 35°C computed using different nucleation parameter values.

In this case, both the actual and the approximated simulations were run using $5 * 10^4$ primaries. The results are shown in Fig. 6.17.

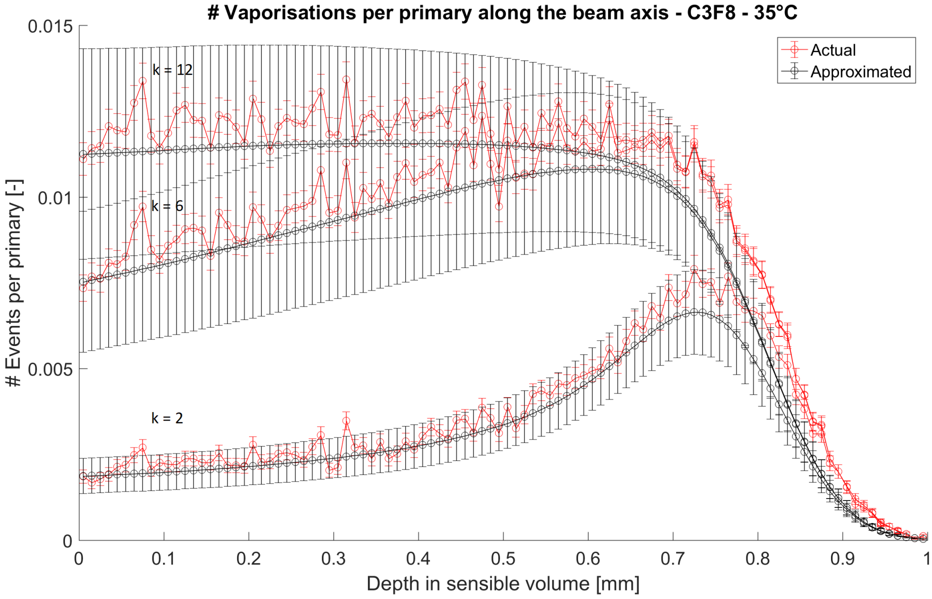

Figure 6.17: Validation of the approximate acceleration technique using a proton beam and C_3F_8 as core gas. Comparison between raw data using different nucleation parameter values.

> The MAPE shows the same behaviour as before. It decreases as the nucleation parameter increases: 15.7% at k = 2, 13.7% at k = 6 and 13.5% at k = 12. However, now since the difference between the LET thresholds is less pronounced and the the statistical uncertainty is higher (the number of primaries is lower by one order of magnitude with respect to the previous simulations with C_4F_{10}), the MAPE reduction is less pronounced, but still present.

In conclusion, there is a good agreement between the actual and the approximate simulations; the deviations between the results are always comprised in the range estimated by the error bars. Hence, this technique has been used in the remainder this work to simulate the nanodroplets behaviour in real experimental conditions, dramatically reducing the total computation time required. The results are presented in the following section.

6.3 Simulations results

In this section, results coming from simulations using C_4F_{10} and C_3F_8 at different temperatures in a 6 MV linac photon beam and in a 60 MeV proton beam will be presented. All the simulations were carried out using the approximate acceleration technique that has been described previously. These results will be extremely useful to plan the future experiments necessary investigate the capabilities of these superheated emulsions to detect the range of protons using an ultrasound-based readout method. Moreover, the phantom experiments that will be carried out in the near future will serve as a tool to validate and improve the simulation model.

6.3.1 Vaporisations induced by a photon beam

An experiment using a photon beam delivered by a 6 MV Varian TrueBeam linear accelerator was conducted. In this experiment, nanodroplets made by C_4F_{10} were tested at 32°C. A total dose of 16 Gy in steps of 4 Gy (500 MU) was delivered. However, it was not really succesful; it was not possible to identify vaporisation signals that were clearly due to the irradiation. In fact, vaporisation signals were recorded before exposure to radiation, during irradiation and in the control measurement. However, according to the literature the degree of superheat for C_4F_{10} at 32°C should not be sufficient to make the vaporisation counts due to photons interactions clearly distinguishable from the spontaneous one (i.e. photon sensitisation is achieved at higher temperatures). So, it could be reasonable to assume that those events were simply spontaneous events. New experiments with a better controlled environment (e.g. temperature, absence of gas in the dilution liquid...) are planned in the near future to confirm such hypothesis.

So, as a first step, the behaviour of superheated nanodroplets when irradiated by a photon beam was investigated implementing the same experimental setup in a Geant4 model. The following table (6.3) contains the description of each volume in the simulation domain (Fig. 6.18): all the components affecting the beam considerably were taken into account.

Volume	**Dim. (w,h,t) [mm]**	**Material**	**Sensitive?**
World	(1150,1150,1150)	Air	No
External Box	(540,410,100)	Polycarbonate	No
Water filling	(530,400,100)	Water	No
Sample holder	(40,40,50)	Plexiglass	No
Layers	(40,40,0.01)	Water	Yes

Table 6.3: Description of the volumes included in the MC model of the photon beam experiment

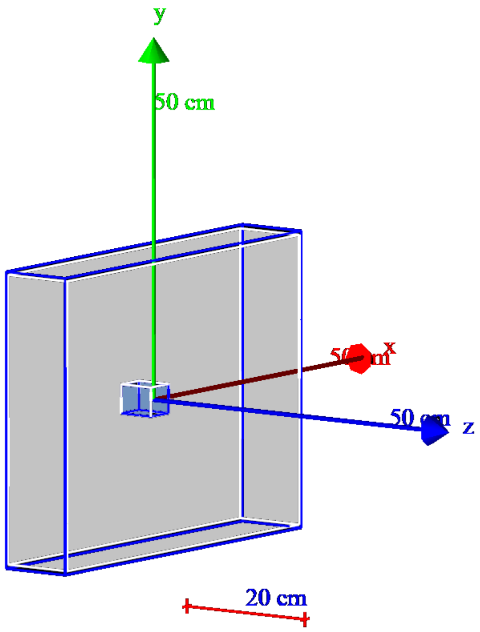

Figure 6.18: Simulation domain. Screenshot taken from Geant4 GUI.

The primary photons enter the world volume from the right-hand-side of the Fig. 6.18. A typical photon spectrum of a medical linear accelerator Varian Clinac 2100 operating at 6MV was implemented as a primary source. In order to achieve a sufficient accuracy, the typical energy distribution of photons in standard conditions with a field size of 3cm x 3cm and 10cm x 10cm (Fig. 6.19) has been imported in the simulation setup and a pure photon source directly incident on the phantom external surface in a perpendicular way has been used. Such energy distribution has been computed by *Konefal et al* using a Monte Carlo code that simulates the whole linac starting from the electron source and including all the beam-line components [62].

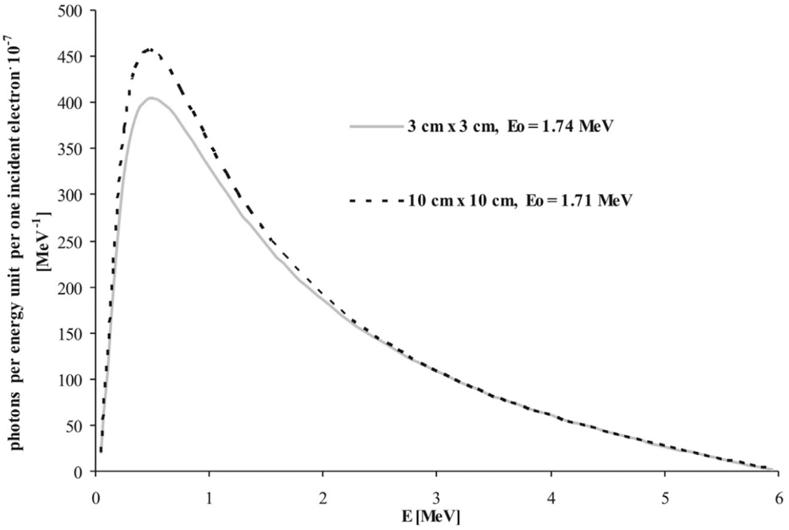

Figure 6.19: 6MV Varian Clinac 2100 photon spectrum [62].

Continuing their path, photons first encounter the water that fills the external polycarbonate container and then the plexiglass sample holder. The inner side of the sample holder is subdivided into 0.01 mm thick layers parallel to the beam axis. A sensitive detector is attached to each layer to tally the fluence of secondary electrons with a given energy that is passing through the layer. Finally, during post-processing the fluence in each layer has been convoluted with a probability kernel computed previously using layers having dimensions $t_l = 0.01mm$ and $Lx = Ly = 0.1mm$ filled with $5 * 10^8$ droplets per ml (560 nm diameter). The probability kernel was computed using mono energetic electron beams with $E_{max} = 3MeV$ and $E_{bin} = 0.02MeV$. The maximum energy has been limited to 3 MeV since the electrons fluence at higher energies is negligible (Fig. 6.20). The resulting vaporisation probabilities are depicted in Fig. 6.21 (C_4F_{10}) and in Fig. 6.22 (C_3F_8).

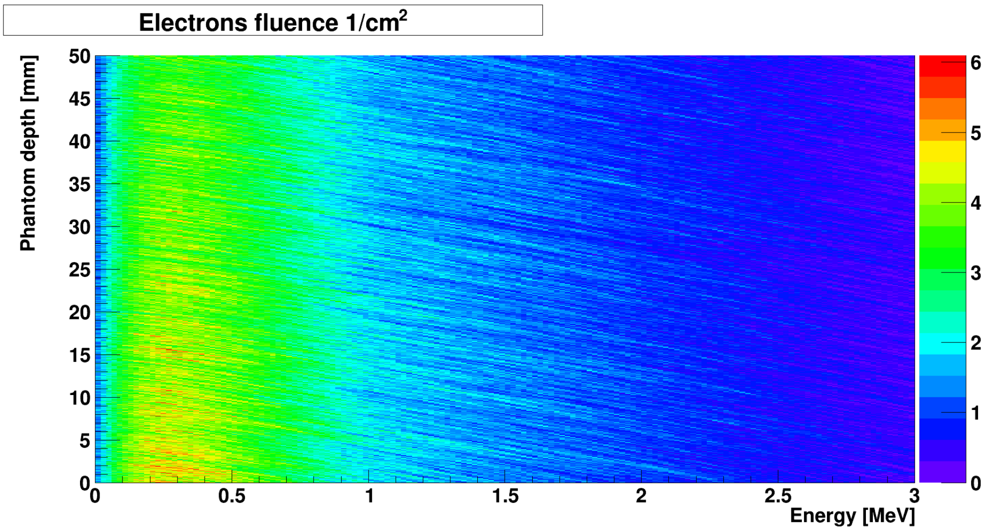

Figure 6.20: Simulations using 6MV linac photon beam. Electrons fluence inside the sample holder. 5e5 histories simulated

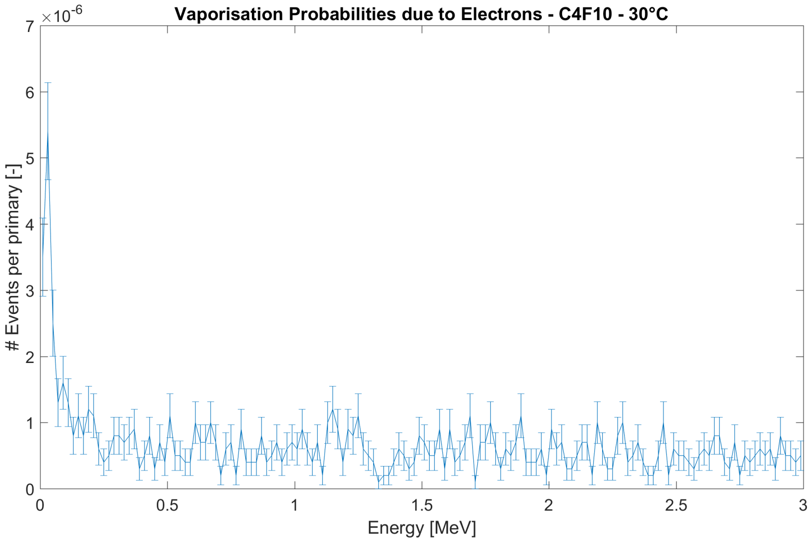

Figure 6.21: Vaporisation probabilities computed for mono energetic electrons at 30°C using C_4F_{10} as core gas, k = 2 and a layer with $Lx = Ly = 0.1mm$ and $t_l = 0.01mm$. 1e7 histories simulated.

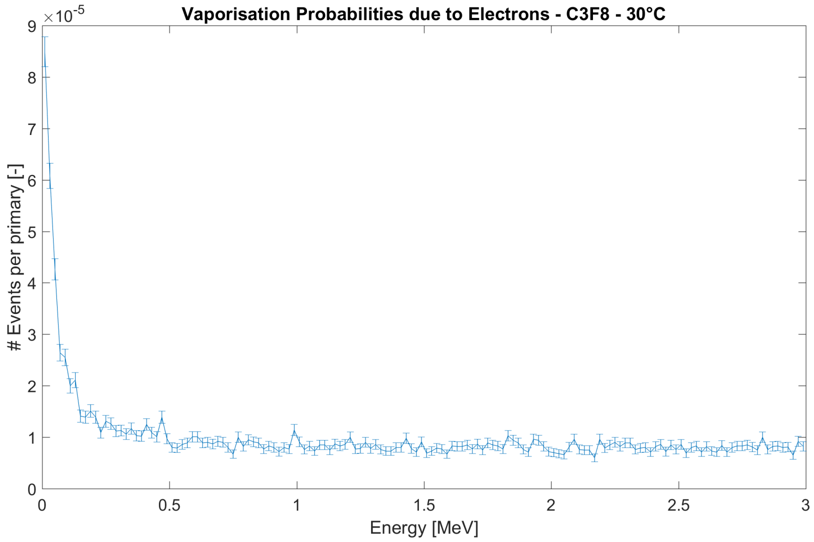

Figure 6.22: Vaporisation probabilities computed for mono energetic electrons at 30°C using C_3F_8 as core gas, k = 2 and a layer with $Lx = Ly = 0.1mm$ and $t_l = 0.01mm$. 1e7 histories simulated.

Afterwards, simulations were performed for the experimental setup for both C_4F_{10} and C_3F_8 at 30°C fixing the nucleation parameter to 2 (worst case in terms of minimum LET requirement). The results, expressed in terms of vaporisations per MU, are depicted in the following pictures:

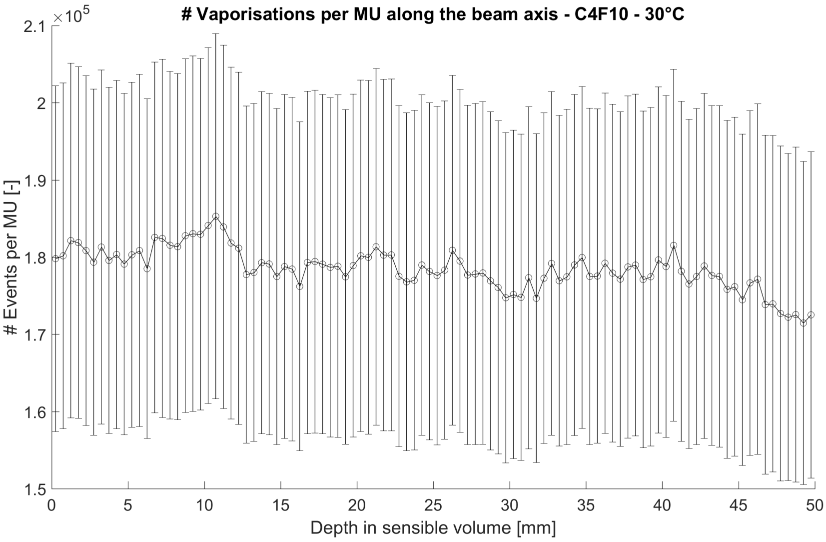

Figure 6.23: Vaporisations per MU along the beam axis. C_4F_{10} core gas at 30°C using k = 2. Minimum LET threshold equal to $232.2\frac{keV}{\mu m}$

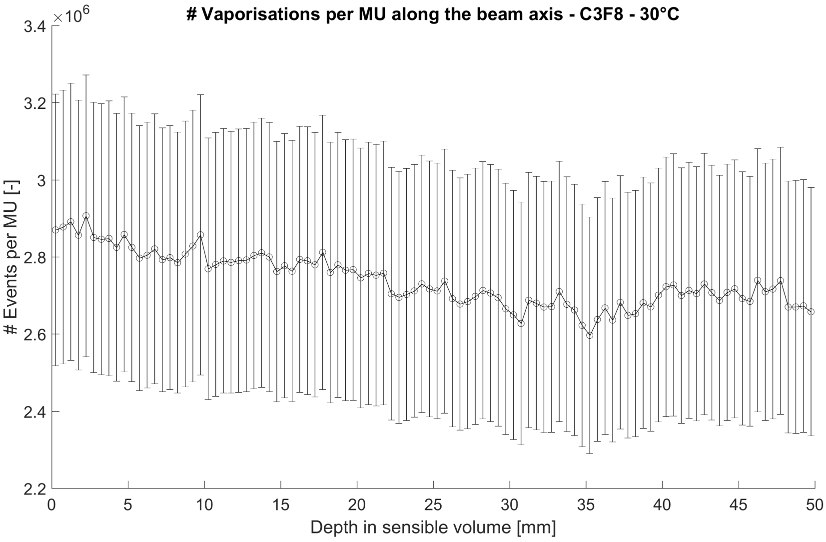

Figure 6.24: Vaporisations per MU along the beam axis. C_3F_8 core gas at 30°C using k = 2. Minimum LET threshold equal to $16.2\frac{keV}{\mu m}$

According to our results, delivering 1 MU ($\approx 4.5 * 10^{14}$ photons) would result in a vaporisation fraction of about 0.20% and 3.17% respectively for C_4F_{10} and C_3F_8. However, especially for C_4F_{10}, the uncertainty on the vaporisation probability values, due to the extremely high LET threshold ($232.2\frac{keV}{\mu m}$) that makes vaporisation events rare (less than 10 events using ten million primaries), is relevant and it can't be estimated easily since the hypothesis of a Gaussian distribution for the counted events doesn't hold any more.

Finally, as already mentioned our estimate does not take into account any depletion effect; for high total vaporisation fraction an overestimation is likely to occur.

6.3.2 Vaporisations induced by a proton beam

A first draft of the experimental setup that will be used in the future proton beam experiments has already been made (Fig. 6.25) and the Geant4 model has been developed on it.

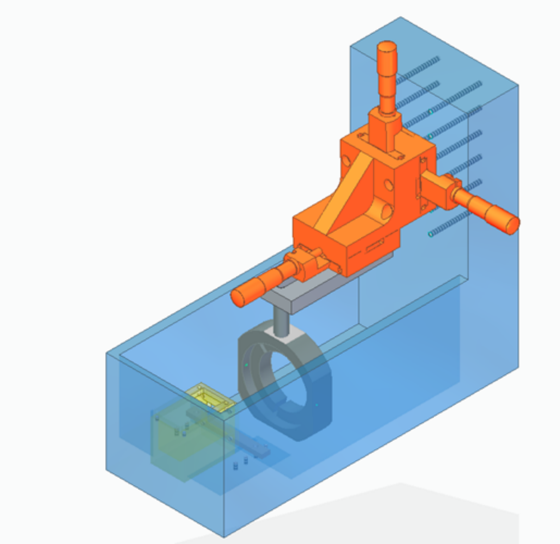

Figure 6.25: Draft of the experimental setup that will be used in the proton induced vaporisation experiments. The beam comes from the left. The sample holder is made of plexiglass and it contains droplets dispersed in an agar matrix

The blue part represents the water tank. If the tank is completely full, the inner dimensions are (280x120x110) mm. The orange part is the 3D linear stage for alignment of the ultrasound probe, and the grey part is the transducer holder. The goal is to measure, online, during beam delivery, the number of vaporisation signals using a single element transducer located distally to the Bragg peak (with the Bragg peak located at its focus). Subsequently, the phantom will be removed and imaged with a 2D ultrasound probe to locate the vaporisation events. The proton beam will come from the left; before entering into the sensitive volume, it will pass through 5 mm of plexiglass (3 mm water tank thickness and 2 mm of phantom mold thickness).

To build up the simulation domain, only the components able to affect the beam in a relevant manner have been considered. They are the external boxes and the phantom (Fig. 6.26). The Table 6.4 contains the description of each volume that has been built.

Volume	**Dim. (w,h,t) [mm]**	**Material**	**Sensitive?**
World	(200,200,400)	Air	No
External Box	(126,116,286)	Plexiglass	No
Water filling	(120,110,280)	Water	No
Sample holder	(32,28,58)	Plexiglass	No
Layers	(28,24,0.1)	Water	Yes

Table 6.4: Description of the volumes included in the MC model of the proton beam experiment

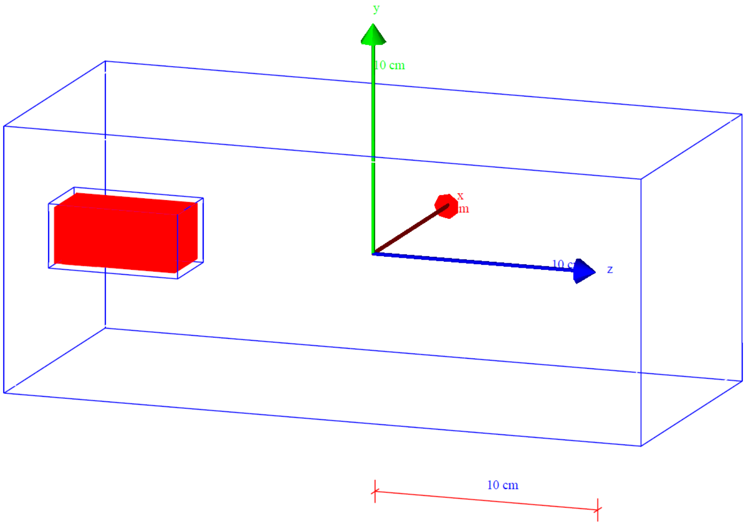

Figure 6.26: Simulation domain. Screenshot taken from Geant4 GUI. The sensitive layers are depicted in red. The beam comes from the left hand side.

Since the major aim of this simulation is to provide qualitative information about the superheated droplets response, a pure proton source with a Gaussian energy distribution was chosen. The mean energy and the standard deviation were respectively set to 60 MeV and 0.8 MeV.

As already mentioned, we expect a huge vaporisation area in the Bragg peak region (due to Coulomb interactions) and some vaporisation during the whole proton track that will be present due to recoil nuclei (high LET) and sparse low LET ionisations [63]. The contribution of recoil nuclei and heavy ions that are formed following nuclear reactions is minimal and its estimation is not our aim; so, only vaporisations due to protons, electrons and neutrons were simulated. Since we are mostly interested in detecting the Bragg peak, we will notice that the only required contribution come from protons and electrons.

In this case, the inner side of the sample holder was subdivided into 0.1 mm thick layers perpendicular to the beam axis. A sensitive detector able to tally the fluence of protons, electrons and neutrons has been attached to each layer. Finally, during post-processing, the fluence values in each layer have been convoluted with the corresponding probability kernel that has been computed previously using layers having dimensions $t_l = 0.1mm$ and $Lx = Ly = 1mm$ filled with $5 * 10^8$ droplets per ml (560 nm diameter).

So, a probability kernel for each relevant ionising particle has been computed:

- Electrons: regarding the electrons, the probability kernel was computed using mono energetic beams with $E_{max} = 0.12MeV$ and $E_{bin} = 0.002MeV$. The maximum energy has been limited to 0.02 MeV since the electrons fluence at higher energies is negligible (Fig. 6.27).

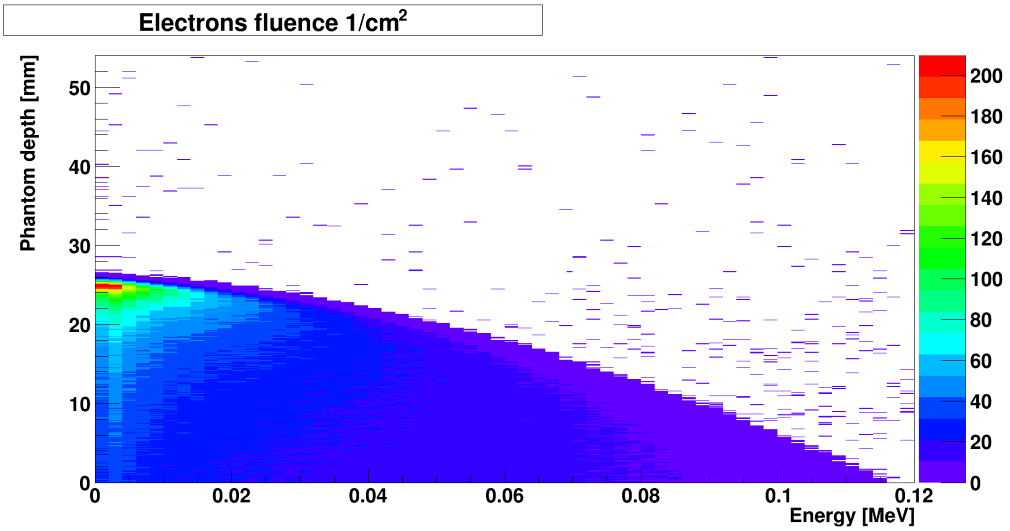

Figure 6.27: Simulations using 60 MeV proton beam. Electron fluence inside the sample holder. 1e5 histories simulated

- Protons: in this case the probability kernel was computed using mono energetic beams with $E_{max} = 60MeV$ and $E_{bin} = 0.5MeV$. The proton fluence above 60 MeV is null (Fig. 6.28).

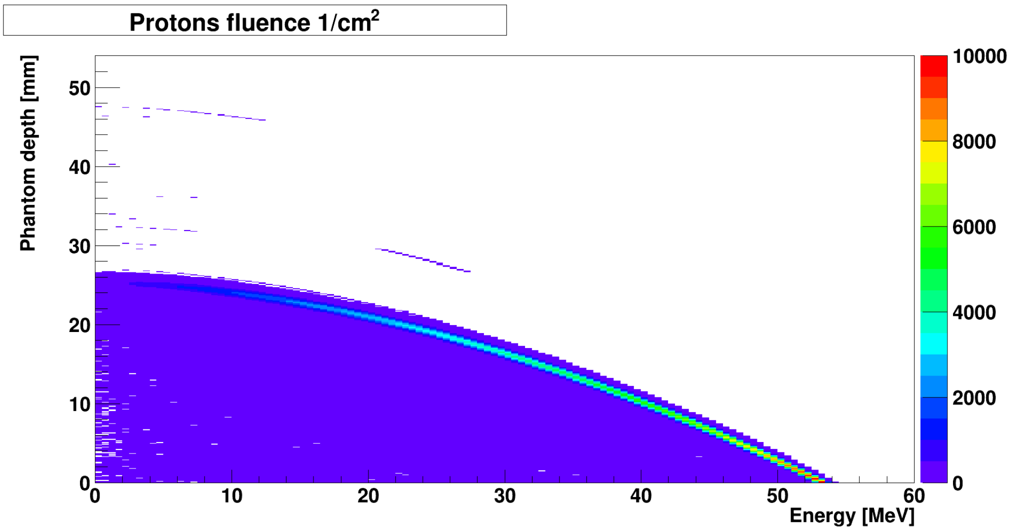

Figure 6.28: Simulations using 60 MeV proton beam. Proton fluence inside the sample holder. 1e5 histories simulated

- Neutrons: in this case the probability kernel was computed using mono energetic beams with $E_{max} = 60MeV$ and $E_{bin} = 0.5MeV$.

The neutron fluence is negligible with respect to the previous ones (Fig. 6.29) and their ability to vaporise the droplets is limited.

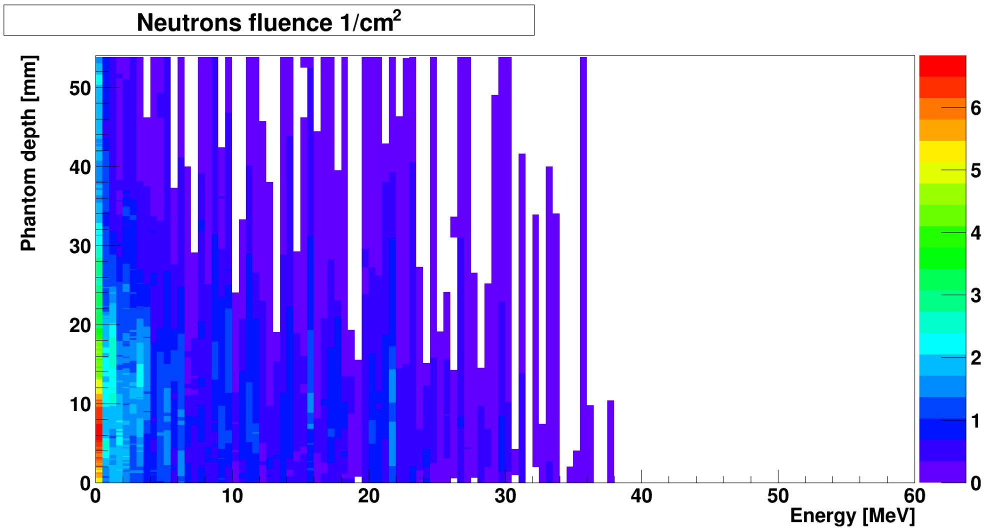

Figure 6.29: Simulations using 60 MeV proton beam. Neutron fluence inside the sample holder. 1e5 histories simulated

For each core gas (C_4F_{10} and C_3F_8), two sets of simulations were run: a first set to perform a sensitivity analysis for the nucleation parameter, by fixing the temperature at 36°C and varying k from 2 to 12. Then, a second set of simulations was performed using a fixed nucleation parameter and increasing the temperature to obtain the minimum temperature needed to clearly identify the Bragg peak by means of the triggered vaporisation events. To better understand where the Bragg peak is located, the normalised dose deposition curve was superimposed in each plot.

Also in this case the results are expressed in terms of number of vaporisation per MU, where a rough estimate of 10^8 primary protons per MU was used.

Firstly, the behaviour of C_4F_{10} was analysed. Looking at the results from the first set of simulations (Fig. 6.30), it seems that superheated nanodroplets made of C_4F_{10} will not be able to clearly detect a Bragg peak at 36°C in the worst case scenario (k = 2). But, already starting from k = 6, it seems possible to detect the peak with a good accuracy, distinguishing the vaporisations due to Coulomb interactions in that area from other non-interesting events.

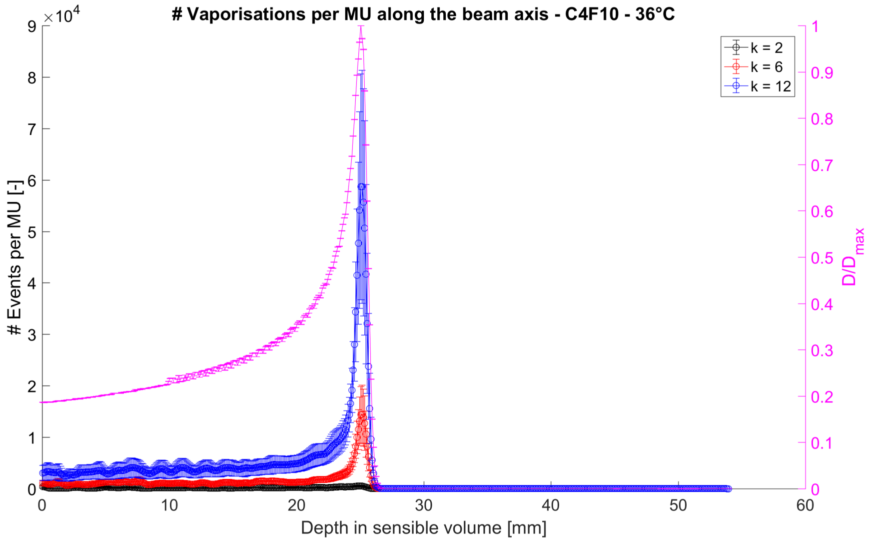

Figure 6.30: Vaporisations per MU along the beam axis using a 60 MeV proton beam. C_4F_{10} core gas at 36°C, different values of the nucleation parameter. The normalised dose deposition curve is depicted in magenta.

Nucleation parameter	LET threshold $[\frac{keV}{\mu m}]$
2	148.84
6	49.61
12	24.81

Table 6.5: Minimum LET threshold for C_4F_{10} at 36°C computed using different nucleation parameter values.

Looking at the second set of simulations (Fig. 6.31), it is clear that an increase in temperature will permit to detect the Bragg peak more clearly even assuming a low value of the nucleation parameter.

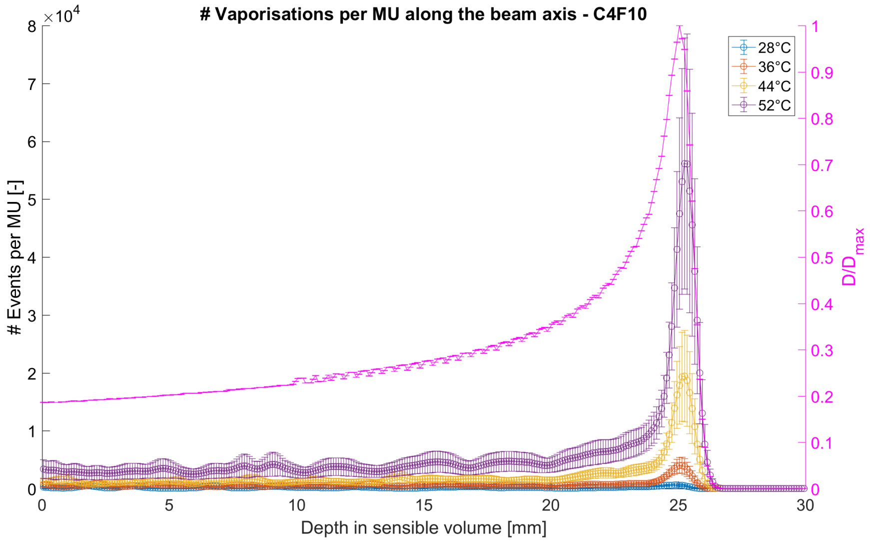

Figure 6.31: Vaporisations per MU along the beam axis using a 60 MeV proton beam. C_4F_{10} core gas at increasing values of temperature. Nucleation parameter fixed to 4. The normalised dose deposition curve is depicted in magenta.

For C_3F_8, even in the worst case scenario the nanodroplets seem to be able to detect the range of protons inside the phantom. In fact, looking at Fig. 6.32 , the Bragg peak region is clearly distinguishable even when a nucleation parameter equal to 2 is set. Consequently, we propose to perform the phantom experiments at a temperature of at least 36°C using C_3F_8, while for C_4F_{10} it should be increased up to 44°C.

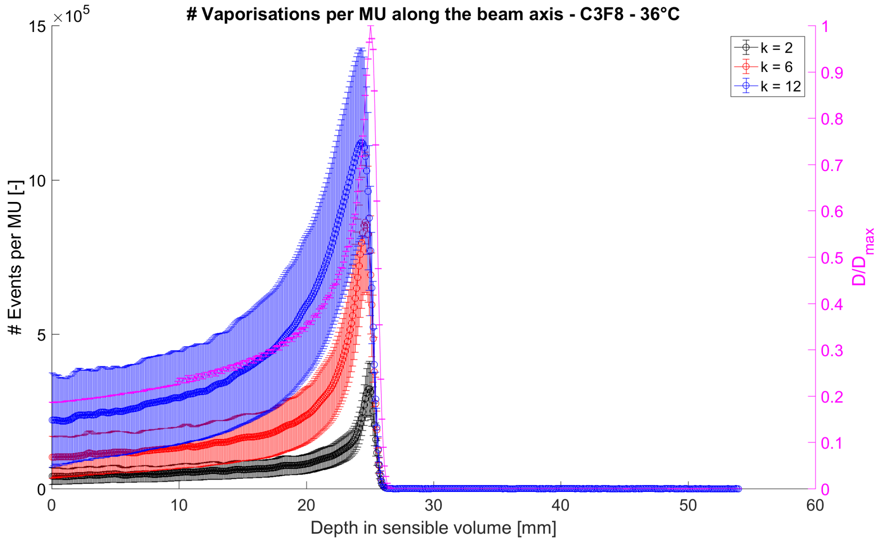

Figure 6.32: Vaporisations per MU along the beam axis using a 60 MeV proton beam. C_3F_8 core gas at 36°C, different values of the nucleation parameter. The normalised dose deposition curve is depicted in magenta.

Nucleation parameter	**LET threshold** $[\frac{keV}{\mu m}]$
2	9.82
6	3.28
12	1.64

Table 6.6: Minimum LET threshold for C_3F_8 at 36°C computed using different nucleation parameter values.

The second set of simulations (Fig. 6.33) shows that there is a good probability to detect the range even a lower temperatures.

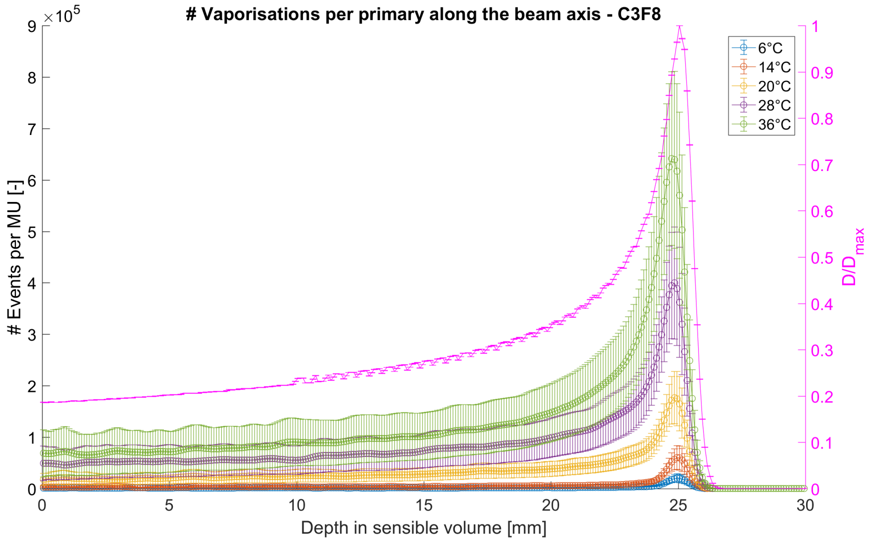

Figure 6.33: Vaporisations per MU along the beam axis using a 60 MeV proton beam. C_3F_8 core gas at increasing values of temperature. Nucleation parameter fixed to 4. The normalised dose deposition curve is depicted in magenta.

Chapter 7

Conclusions

The use of C_3F_8 and C_4F_{10} superheated nanodroplets as an in-vivo proton range verification tool was investigated using a Monte Carlo method approach. Specifically, their response to both a typical 6 MV linac photon beam and to a 60 MeV proton beam was simulated and the number of vaporisations along the beam axis was estimated under different experimental conditions.

For this purpose, an approximate acceleration technique was developed to dramatically reduce the computational time needed, while still achieving high accuracy of the estimated vaporisation events. The technique was validated using the non-accelerated computationally intensive model, showing good agreement in terms of Mean Absolute Percentage Error.

The results of the simulations, at least for C_3F_8 , are encouraging to plan future in phantom experiments.

Indeed, already from 36°C onwards, it seems possible to detect the Bragg peak region (even in the worst case scenario, k = 2) by looking at the vaporisation events.

However, in case C_4F_{10} is used as core gas, it is not certain whether the proton range will be detectable due to the uncertainties about the nucleation parameter.

Nevertheless, the physics behind the vaporisation process is complex and the theory of radiation induced vaporisation is semi-empirical. This makes the prediction of their response difficult and requires every model to be verified experimentally for the particular superheated emulsion involved.

Moreover, it is worth to remind that several assumptions (e.g. Laplace pressure effect was neglected, the nanodroplet distribution was assumed monodisperse, spontaneous vaporisation events were neglected) have been made in order to get these results; for this reason, until a proper validation of the model is made, it can only serve as a qualitative prediction of what will happen in a real experiment.

Hence, phantom experiments are planned to validate the model, hopefully confirming the ability to capture the essential physics of the radiation induced nucleation process. Finally, in future work, the model can be elaborated to include contributions from the Laplace pressure and the effect of polydispersity of the nanodroplets size distribution.

List of Figures

List of Tables

Bibliography

[1] Verboven E., D'Agostino E., Callens M., Pfeiffer H., Verellen D., D'hooge J., Van Den Abeele K., "Ultrasound based dosimetry for radiotherapy: in-vitro proof of principle", 2014 IEEE International Ultrasonics Symposium Proceedings

[2] Robert Johnston's database of radiological incidents and related events, `http://www.johnstonsarchive.net/nuclear/radevents/index.html`

[3] Website of the AMPHORA (Acoustic Markers for Enhanced Remote Sensing of Radiation Doses) Project, `http://www.amphora-project.eu/`

[4] B. Mijnheer "State of the art of in-vivo dosimetry", Radiation Protection Dosimetry, vol. 131, no. 1, pp. 117-122, 2008.

[5] D'Errico F. , "Radiation dosimetry and spectrometry with superheated emulsions", Nuclear Instruments and Methods in Physics Research B 184 (2001) pp. 229-254

[6] NDT Resource Center, `https://www.nde-ed.org/EducationResources/HighSchool/Radiography/discoveryxrays.htm`

[7] Glasser O: Wilhelm Conrad Roentgen and the early history of the roentgen rays, Springfield, Ill, 1933, Charles C. Thomas.

[8] Technic of roentgenotherapy to treat epitheleoma of the face, Wikimedia Commons, `https://upload.wikimedia.org/wikipedia/commons/thumb/e/e3/Technic_of_roentgenotherapy_to_treat_epitheleoma_of_the_face_-_1915.jpg`

[9] Gianfaldoni S, Gianfaldoni R, Wollina U, Lotti J, Tchernev G, Lotti T, An Overview on Radiothreapy: From its History to its Current

Applications in Deramtology. Open Access Maced J Med Sci. 2017 Jul 25; 5(4):521-525. https://doi.org/10.3889/oamjms.2017.122

[10] Bortfeld T., Schmidt-Ullrich R., De Neve W., E.Wazer D. (Eds.), 2006, Image-Guided IMRT, Springer.

[11] *Lecture notes of the course on Biomedical and Industrial application of radiation, A.A 2017/2018, Politecnico di Torino*

[12] Anderson, H.L. , 1986, Handbook Of Radiotherapy Physics

[13] How radiation affects cells , Radiation Effects Research Foundation https://www.rerf.or.jp/en/programs/roadmap_e/health_effects-en/basickno-en/radcell-en/

[14] Aarhus University Hospital, Particle radiobiology, http://www.en.auh.dk/departments/the-danish-centre-for-particle-therapy/research/intro-workpackages/basic-and-translational-research/wp1---particle-radiobiology/

[15] Desouky O., Zhou G., “Biophysical and radiobiological aspects of heavy charged particles”, Journal of Taibah University for Science 10 (2016) pp. 187-194

[16] ICRP, 2003. Relative Biological Effectiveness (RBE), Quality Factor (Q), and Radiation Weighting Factor (wR). ICRP Publication 92. Ann. ICRP 33 (4).

[17] Ionising radiation - Protection Dose quantities in SI units, Wikimedia Commons, https://upload.wikimedia.org/wikipedia/commons/0/03/SI_Radiation_dose_units.png

[18] Chang Gung Memorial Hospital International Medical Center, Introduction to Proton Beam Radiation Therapy, http://www.chang-gung.com/en/news-1.aspx?rows=8&page=1&type=&id=352&mid=120&bid=3

[19] Leroy R, Benahmed N, Hulstaert F, Mambourg F, Fairon N, Van Eycken L, De Ruysscher D. Hadron therapy in children – an update of the scientific evidence for 15 paediatric cancers. Health Technology Assessment (HTA) Brussels: Belgian Health Care Knowledge Centre (KCE). 2015. KCE Reports 235. D/2015/10.273/05.

[20] Essers M., J. Mijnheer B, “ In Vivo Dosimetry During External Photon Beam Radiotherapy”, Int. J. Radiation Oncology Biol. Phys., Vol 43, No 2, pp. 245-259, 1999

[21] Zhu X, El Fakhri G., “Proton Therapy Verification with PET imaging”, Theranostics, 2013; 3(10):731-740, doi:10.7150/thno.5162

[22] Yunhe Xie, El Hassane Bentefour Guillaume Janssens, Julien Smeets, Franc¸ois Vander Stappen, Lucian Hotoiu, Lingshu Yin, Derek Dolney, Stephen Avery, Fionnbarr O’Grady, Damien Prieels, James McDonough, Timothy D. Solberg, Robert A. Lustig, Alexander Lin, Boon-Keng K. Teo, “Prompt Gamma Imaging for In Vivo Range Verification of Pencil Beam Scanning Proton Therapy”, Int J Radiation Oncol Biol Phys, Vol. 99, No. 1, pp. 210e218, 20170360-3016/

[23] Paganetti H., “Range uncertainties in proton therapy and the role of Monte Carlo simulations”, Phys. Med. Biol. 57 (2012) R99-R117, doi:10.1088/0031-9155/57/11/R99

[24] Knopt C.-A., Lomax A., “In vivo proton range verification: a review”, Phys. Med. Biol. 58 (2013) R131-R160, doi:10.1088/0031-9155/58/15/R31

[25] Lu H.-M., “A point dose method for in vivo range verification in proton therapy”, Phys. Med. Biol. 53 (2008) N415-N422, doi:10.1088/0031-9155/53/23/N01

[26] F. Gensheimer M., I. Yock T., J. Liebsch N., C. Sharp G., Paganetti H., Madan N., Grant P. E., Bortfeld T., “In Vivo Proton Beam Range Verification Using Spine MRI Changes”, Int. J. Radiation Oncology Biol. Phys., Vol 78, No. 1, pp. 268-275, 2010

[27] Oleg N. Vassiliev, 2017, Monte Carlo Methods for Radiation Transport, Springer.

[28] *Lecture notes of the course on Technologie en Technieken in de Radiotherapie, A.A 2018/2019, KU Leuven*

[29] Metropolis, N. , 1987, The beginning of the Monte Carlo method. Los Alamos Sci. 15(Special issue), 125–130

[30] Sergè E. , 2007, From X-Rays to Quarks: Modern Physicists and their Discoveries. Dover, Mineola, NY

[31] Anderson, H.L. , 1986, Scientific uses of the MANIAC. J. Stat. Phys. 43(5/6), 731–748

[32] Zygmanski P., Sajo E. , Nanoscale radiation transport and clinical beam modeling for gold nanoparticle dose nhanced radiotherapy (GNPT) using X-rays. Br J Radiol 2016; 89; 20150200

[33] Nicotra D. , M.Sc thesis “Characterization of a proton beam delivery line with Monte Carlo simulation”, 2018

[34] American Association of Physicists in Medicine (AAPM): Tissue inhomogeneity corrections for megavoltage photon beams. Radiation Therapy Committee Task Group 65. Report No. 85. , Medical Physics Publishing, Madison, WI , 2004

[35] Incerti, S., Baldacchino, G., Bernal, M., Capra, R., Champion, C., Francis, Z., Guatelli, S., Guye, P., Mantero, A., Mascialino, B., Moretto, P., Nieminen, P., Villagrasa, C., Zacharatou, C.: The Geant4-DNA project. Int. J. Model. Simul. Sci. Comput. 1, 157–178 (2010)

[36] Bernal, M.A., Bordage, M.C., Brown, J.M.C., Davidkova, M., Delage, E., El Bitar, Z., Enger, S.A., Francis, Z., Guatelli, S., Ivanchenko, V.N., Karamitros, M., Kyriakou, I., Maigne, L., Meylan, S., Murakami, K., Okada, S., Payno, H., Perrot, Y., Petrovic, I., Pham, Q.T., Ristic- Fira, A., Sasaki, T., Stepan, V., Tran, H.N., Villagrasa, C., Incerti, S.: Track structure modeling in liquid water: a review of the Geant4-DNA very low energy extension of the Geant4 Monte Carlo simulation toolkit. Phys. Med. 31(8), 861–874 (2015)

[37] Wang, H., Vassiliev, O.N.: Microdosimetric characterisation of radiation fields for modelling tissue response in radiotherapy. Int. J. Cancer Ther. Oncol. 2(1), 020116 (2014)

[38] Lee, S. M. S., and Young, G. A. (1999), The effect of Monte Carlo Approximation on Coverage Error of Double-Bootstrap Confidence Intervals, Journal of the Royal Statistical Society, Series B: Statistical Methodology, 61, 353-366

[39] Elizabeth Koehler, Elizabeth Brown & Sebastien J.-P. A. Haneuse (2009) , On the Assessment of Monte Carlo Error in Simulation-Based Statistical Analyses, The American Statistician, 63:2, 155-162, DOI: 10.1198/tast.2009.0030

[40] Sarka R., Kumar Mondal P., Datta M., Kumar Chattarjee B., “A new optical method for the detection of bubble nucleation in superheated droplet detector”, Review of Scientific Instruments, 88, 066106 (2017)

[41] D’Errico F., Nath R., Lamba M., Holland K. S.,“A position-sensitive superheated emulsion chamber for three-dimensional photon dosimetry”, Physics in Medicine & Biology (1998), Vol. 43, pp. 1147-1158

[42] D’Errico F., Nath R., Nolte R.,“A model for photon detection and dosimetry with superheated emulsions”, Medical Physics (2000), Vol. 27, No. 2, pp. 401-409

[43] D’Errico F., “Status of radiation detection with superheated emulsions”, Radiation Protection Dosimetry (2006), Vol. 120, No. 1-4, pp. 475-479, doi:10.1093/rpd/ncj018

[44] D’Errico F., “Radiation dosimetry and spectrometry with superheated emulsions”, Nuclear Instruments and Mehods in Physics Research B (2001), Vol. 184, pp. 229-254

[45] Mountford A. P., Thomas N. A., Borden A. M., “Thermal Activation of Superheated Lipid-Coated Perfluorocarbon Drops”, Langmuir (2015), Vol. 31, pp. 4627-4634, doi:10.1021/acs.langmuir.5b00399

[46] Mountford A. P., Thomas N. A., Borden A. M., “Measured Proton Sensitivities of Bubble Detectors”, Radiation Protection Dosimetry (2004), Vol. 111, No. 2, pp. 181-189, doi:10.1093/rpd/nch330

[47] Seitz, F.,”On the theory of bubble chamber”, Phys. Fluids (1958), Vol. 1, pp. 2-13

[48] West, C. D.,”Cavitation Bubble Nucleation by Energetic Particles”, Oak Ridge National Laboratory (1998), ORNL/TM-13683

[49] Di Fulvio A., Huang J., Staib L., d’Errico F., “LET dependence of bubbles evaporation pulses in superheated emulsion detectors”, Nuclear Instruments and Methods in Physics Research A (2015), Vol. 784, pp. 156-161, doi:10.1016/j.nima.2015.01.064

[50] Sarkar R., Chatterjee B. K., Roy B., Roy S.C., “Radiation detection by using superheated droplets”, Radiation Physics and Chemistry (2006), Vol.75, pp. 2186-2194, doi:10.1016/j.radphyschem.2005.10.007

[51] Paradossi G., Pellegretti P., Trucco A., 2010, Ultrasound Contrast Agents: Targeting and Processing Methods for Theranostics, Springer.

[52] Arena C. B., Novell A., Sheeran S. P., Puett C., Philips C. L., Dayton A. P., "Ultrasound Imaging from Vaporisation Signals Emitted by Phase Change Contrast Agents", IEEE International Ultrasonics Symposium Proceedings (2014), doi:10.1109/ULTSYM.2014.0441

[53] Sander M. Van der Meer, Benjamin Dollet, Marco M. Voormolen, Chien T. Chin, Ayache Bouakaz, Nico de Jong, Michel Versluis, and Detlef Lohse, "Microbubble spectroscopy of ultrasound contrast agents", The Journal of the Acoustical Society of America, 121 (1), 2007, pp. 648-656

[54] Heymans S. V., Toumia Y., Carlier B., Giammanco A., Collado G., Lange H., Himmelreich U., Sterpin E., de Jong N., d'Agostino E., Paradossi G., D'hooge J., Van Den Abeele K., "Investigation of PCDA-PFB nanodroplets for multimodal imaging and in vivo dosimetry of radiation therapy", The 24th European Symposium on Ultrasound Contrast Imaging, 18-19 January 2019, Rotterdam, The Netherlands.

[55] PICASSO collaboration, "New insights into particle detection with superheated liquids", New Journal of Physics (2011), Vol. 13, arXiv:1011.4553v1

[56] MATLAB, The MathWorks, Inc., Natick, Massachusetts, United States.

[57] Brun R., Rademakers F., "ROOT - An object oriented data analysis framework", Nuclear Instruments and Methods in Physics Research A (1997), No. 389, pp. 81-86

[58] GEANT Collaboration et al. «Physics reference manual». In: Version: geant4 10.9 (2016).

[59] GEANT Collaboration. «Introduction to Geant4». In: (2010).

[60] GEANT Collaboration, `https://geant4.web.cern.ch/`

[61] CERN detector cooling data, `www.detector-cooling.web.cern.ch/Detector-Cooling/data/C4F10.htm` and `www.detector-cooling.web.cern.ch/Detector-Cooling/data/C3F8.htm`

[62] Konefal A., Bakoniak M., Orlef A., Maniakowski Z., Szewczuk M., "Energy spectra for the 6 MV X-ray therapeutic beam generated by Clinac-2300 linac", Radiation Measurements (2005), No. 72, pp. 12-22

[63] Guo S. et al., “Proton tracks in bubble detector”, Nuclear Instruments and Methods B (2002), No. 198, pp. 135-141

[64] Propagation of Uncertainty through Matematical Operations, Massachusetts Institute of Technology, `http://web.mit.edu/fluids-modules/www/exper_techniques/2.Propagation_of_Uncertaint.pdf`

[65] Counting statistics laboratory, Department of Physics & Astronomy, University of Tennesse, `http://electron6.phys.utk.edu/phys250/Laboratories/counting_statistics.htm`